LUMINESCENCE EFFECTS IN QUANTUM WELL STRUCTURES IN MAGNETIC AND ELECTRIC FIELDS

by

Sava Atanassov Denev

B.S., Sofia University, 1995

M.S., University of Pittsburgh, 2002

Submitted to the Graduate Faculty of

the School of Arts and Sciences in partial fulfillment

of the requirements for the degree of

Doctor of Philosophy

University of Pittsburgh

2004

UNIVERSITY OF PITTSBURGH

SCHOOL OF ARTS AND SCIENCES

This dissertation was presented

by

Sava Atanassov Denev

It was defended on

September 22, 2004

and approved by

David Snoke, Associate Professor, Dept. of Physics and Astronomy

Daniel Boyanovsky, Professor, Dept. of Physics and Astronomy

Robert Devaty, Associate Professor, Dept. of Physics and Astronomy

Hrvoje Petek, Professor, Dept. of Physics and Astronomy

David Waldeck, Professor, Dept. of Chemistry

Dissertation Director: David Snoke, Associate Professor, Dept. of Physics and Astronomy

LUMINESCENCE EFFECTS IN QUANTUM WELL STRUCTURES IN MAGNETIC AND ELECTRIC FIELDS

Sava Atanassov Denev, PhD

University of Pittsburgh, 2004

We have performed experimental studies of the exciton dynamics in coupled quantum wells in electric and magnetic fields. Being composed of an electron and a hole, the excitons are Bose particles and there are theoretical predictions that they should undergo Bose-Einstein condensation (BEC). Coupled quantum wells, a two dimensional system due to the quantum confinement, are particularly suitable for studying BEC of excitons due to the ability to extend excitons' lifetime up to several microseconds. We have found that the disorder in the structure plays an important role in the properties of the exciton luminescence under magnetic field. We were also among the first to observe an unique effect—luminescence rings around the excitation spot that can span over distances of millimeters. We found that this effect is extremely dependent on the specific experimental conditions as well as some characteristic properties of the structure, like doping level, that can facilitate charge separation in two dimensions.

TABLE OF CONTENTS

LIST OF TABLES

LIST OF FIGURES

1.0 INTRODUCTION

The main motivation for this work was to study 2D dynamics of excitons in coupled quantum wells. The main driving force is the general issue of Bose-Einstein condensation of excitons. Along the way, however, other related problems attracted our attention. The importance of disorder in the system, for example, is a very relevant question since in a typical quantum well structure there is always disorder—at the interfaces, from impurities, from variation of the well width, etc. Other processes like diffusion and transport of the excitons and trapping also have an important role in the overall picture of exciton dynamics in two dimensions. In the course of our studies we have found that disorder, for example, plays a significant role in the carrier dynamics in the presence of a magnetic field. We have also observed that under certain conditions the exciton luminescence can exhibit some very unusual and unique features.

In this introductory chapter we will outline some of the features of the excitons and the quantum wells, and will describe the experimental setup.

1.1 EXCITONS

If we consider a semiconductor with no impurities at low temperatures, the valence band will be completely filled with electrons and the conduction band will be empty. If now an electron is excited from the valence band to the conduction band by, for example, a photon with appropriate energy, an empty state will be left in the place of the electron. This "hole" will behave like a positive particle in the valence band, which is filled with electrons. Naturally there is Coulomb attraction between the hole and the electron and they may form

1

a bound state much like a hydrogen atom. Such a bound state is called an exciton. The states of an exciton can be found by analogy with a hydrogen or positronium atom. The energy of the hydrogen atom is given by

$$E = \frac{-Ry}{n^2} + \frac{\hbar^2 k^2}{2(m_0 + m_p)},$$ (1.1)

where Ry is the Rydberg energy, $Ry = \frac{e^2}{2a_0} = 13.6eV$ with a_0 being the hydrogenic Bohr radius, and n is the principal quantum number. The second term represents the kinetic energy of the particle, where m_0 and m_p are respectively the mass of the electron and the proton. By analogy one can write a similar expression for the energy of the exciton:

$$E_{ex} = E_{gap} - \frac{e^2}{2a_{ex}\epsilon\, n^2} + \frac{\hbar^2 k^2}{2(m_e + m_h)}$$ (1.2)

with excitonic Rydberg energy $Ry_{ex} = \frac{e^2}{2a_{ex}\epsilon}$, where $a_{ex} = \frac{\hbar^2\epsilon}{e^2 m_r}$ is the exciton Bohr radius and $m_r = \frac{m_e m_h}{m_e + m_h}$ is the reduced mass of the exciton. Since the excitons are surrounded by the atoms of the crystal lattice, we have accounted for the screening of the interaction by inclusion in (1.2) of the static dielectric constant ϵ. In semiconductors ϵ is on the order of 10 so the excitonic Bohr radius is usually much larger than the average lattice constant. In GaAs, for example, $\epsilon = 13$ and therefore $a_{ex} \sim 120$ Å. E_{gap} is the band gap energy of the semiconductor. From (1.2) we see that if the kinetic energy of the exciton is zero, the particle has energy less than the band gap energy by the amount Ry_{ex}. This is the binding energy of the exciton.

There are in general two types of excitons. If there is strong interaction between the hole and the electron they will remain confined to a single lattice site. This kind of exciton is called a "Frenkel" exciton. If, on the other hand, the interaction is weak, the electron-hole pair will span over many lattice sites. Then the exciton is called a "Wannier-Mott" exciton.

Excitons are usually created when a photon with certain energy $\hbar\omega$ promotes an excited electron into the conduction band, generating a hole in the valence band, so that they bind into an exciton. After a certain finite time, ultimately depending on the overlap of the electron and hole wave functions, the electron and the hole can recombine to produce a photon again. By that time the exciton may have moved microns away. This means that

we can think of the exciton as a quantum of energy moving through the crystal. Since the exciton consists of two particles with equal but opposite charges, it obviously is a neutral particle and applying an external electric field will not produce exciton motion. On the other hand, excitons will react to a local change in the energy of the band structure and will move to the location with minimum energy. So one way to move excitons would be to create such local changes, for example by applying nonuniform stress.

Since the electron and the hole both have half-integer spin, the exciton has integer spin which makes it a boson. As such, it can undergo, at least in principle, Bose-Einstein condensation where under the appropriate conditions a macroscopic number of particles can occupy one single quantum state—in equilibrium, the one with lowest energy. The critical particle density n for a BEC transition of an ideal Bose gas to occur in three dimensions is given by

$$n = 2.612 \left(\frac{2\pi m\, k_B T_c}{h^2} \right)^{3/2} \tag{1.3}$$

or for the critical temperature T_c

$$T_c = \frac{h^2}{2\pi k_B\, m} \left(\frac{n}{2.612} \right)^{2/3}, \tag{1.4}$$

where m is the mass of the Bose particle and T_c is the critical temperature at which the condensation occurs. The inverse proportionality between m and T_c is part of the appeal to investigate BEC of excitons in semiconductors. Since the mass of the exciton is on the order of the effective mass of the electron, which itself is a fraction of the free electron mass, the critical temperature for given particle density is much higher than the temperature required for other Bose systems. The BEC of alkali atoms, for example, occurs at the staggering temperature of a few nanokelvins [1, 2]!

The idea for BEC of excitons has been around for more than forty years [3, 4] and various theories have been proposed [5, 6], but still solid evidence hasn't been found. If such evidence is demonstrated, excitons in semiconductors will be among the few systems other than superfluid helium, spin polarized hydrogen, and alkali atoms, that can undergo BEC. Besides the scientific understanding of the processes involved such success may also pave the way for some novel applications like new switching devices or achieving coherence without a laser since the luminescence from the condensate should be coherent [7, 8].

A major difference between the atomic and excitonic systems in respect to BEC is the finite lifetime of the excitons. If the excitonic gas is to undergo a spontaneous BEC transition to a thermodynamic state with well defined temperature, the lifetime of the excitons has to be longer than the thermalization time, *i. e.* the time required to reach quasi-equilibrium. In GaAs quantum wells, for example, the exciton thermalization times at low temperatures have been measured to be up to several hundred picoseconds [9], which in some cases could be comparable to the exciton lifetime. In such a way the finite lifetime of the excitons imposes a major limitation to the experiments pursuing BEC.

Equation (1.3) shows the minimum exciton density required for BEC to occur. There is another limit, however, when the density is so high that the excitons will begin to see the Fermi nature of the electrons and the holes of the other excitons and overall the gas cannot be treated as Bose anymore. So, in order that such a treatment to be valid, the density of excitons should stay below some limit, on average

$$n \ll 1/a_{ex}^3. \tag{1.5}$$

Using the value of $a_{ex} = 120$ Å from above this limit implies densities on the order 5×10^{17} cm^{-3}.

There are other types of transitions that can occur in a gas of excitons. If the interaction between the excitons is attractive they can form pairs similar to the hydrogen molecule, called biexcitons, which can exist together with the normal exciton gas. In such a state a phase transition to a liquid state may occur and form a liquid of Fermions called electron-hole liquid (EHL) similar to metallic hydrogen [10, 11, 12].

If at a certain temperature the dissociation of excitons produces enough free electrons and holes that they start screening the Coulomb interaction between the electron-hole pairs thus preventing them from binding into pairs, another thermodynamic phase appears—a conducting but charge neutral electron-hole plasma (EHP). The transition from EHP to nonconducting exciton gas is called the Mott transition.

Growth direction

E_C

E_{gA} E_{gB}

E_V

A   B   A

b)

Growth direction

E_{gA}

E_C

E_{gB}

E_V

A   B   A   B
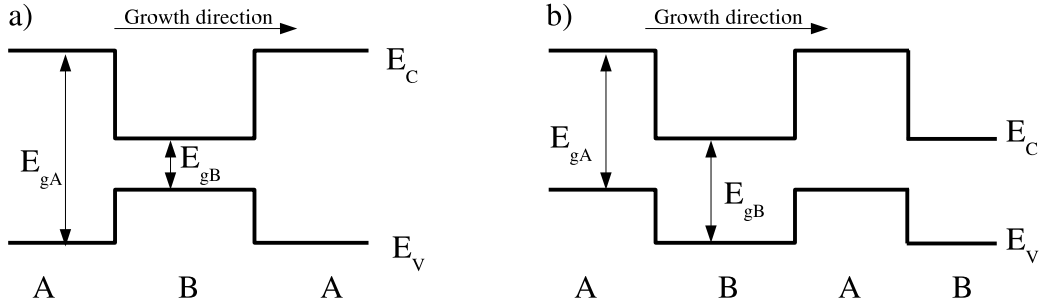
Figure 1.1: Two different quantum well types: a) type I and b) type II.

1.2 QUANTUM WELLS

If we consider a charge-neutral semiconductor heterojunction where two semiconductors are in contact along an atomically clean surface (for example, one is grown on top of the other, and we neglect the lattice mismatch) the vacuum levels of both semiconductors will align. In general they will have different work functions and band structures which will lead to abrupt band discontinuities. If a thin layer of semiconductor B is sandwiched between two layers of semiconductor A, with a proper choice of the materials A and B, the newly formed conduction and valence band profiles will represent a quantum well for the electrons and the holes respectively, where they can get trapped. Depending on the alignment of the bands, there are two types of quantum wells, shown in Figure 1.1. In type I quantum wells, the electrons and the holes are confined in the same layer, whereas in type II they are in adjacent layers.

If the well is narrow enough, the motion of the electrons and the holes will be confined to a two-dimensional plane perpendicular to the growth direction. When excitons are formed, they will be confined in two dimensions as well. In such a way the quantum wells provide a convenient environment for studying particle dynamics in 2-dimensional systems.

Excitons in quantum wells exhibit some features not observed in bulk material. First, in quantum wells the exciton energy is different from the one in bulk. In bulk the energy of the exciton is the band-gap energy, E_g, minus the exciton binding energy, Ry_{ex} (Equation

(1.2)), whereas in quantum wells there are additional factors due to the confinement of the electrons and the holes. A simple estimate of the confinement energy in a square well with infinitely high walls is $E = \dfrac{\pi^2 \hbar^2 n^2}{2mL^2}$, where L is the width of the well and $n = 1, 2, 3 \ldots$ denotes the energy level of the confined particle. Also, due to the confinement, an increase of the binding energy is observed with decreasing well width. Calculations show that this increase of the binding energy could be up to several times its bulk value [13, 14, 15, 16, 17]. At low temperatures, excitonic features dominate the absorption spectrum of quantum well structures (Figure 1.2) and even at room temperature some large excitonic nonlinear optical effects are observed in quantum well structures [18]. Figure 1.2, from one of the first studies of quantum wells by Dingle *et al.* [19], shows the absorption spectra of GaAs quantum wells at 2 K for different well widths. As the well narrows, quantum confinement takes place and distinct exciton peaks, corresponding to different n's in the expression for the confinement energy above, appear in the spectrum above the GaAs absorption energy. Another feature, noticeable from Figure 1.2, is the increase of the confinement energy with decreasing well width—the exciton lines move to higher energies and their separation increases as the quantum wells get narrower—which is expected from the inverse proportionality between E and L.

The idea of designing and building quantum wells and superlattice structures by growing alternating thin layers of different semiconductors was proposed back in the 1970s by Esaki and Tsu [20, 21], but it was the use of advanced growing techniques like Molecular Beam Epitaxy that allowed the growing of layers with well controlled thickness and atomically clean surfaces and interfaces, thus drastically improving the quality of the structures. To achieve quantum confinement the width of the quantum well has to be on the order of the de Broglie wavelength of the electron, or several hundred ångsröms. This method has been used successfully but also has intrinsic disorder due to width variation. For example, using the confinement energy of an electron in the ground state of a infinitely deep quantum well, $E = \dfrac{\pi^2 \hbar^2}{2mL^2}$, we find the change of the energy to be proportional to the change of the well width: $|\delta E/E| = |\delta L/L|$. If we assume a well width of 100 Å then a change of the well thickness by a single monolayer, which is about 6 Å, will introduce a 6% change of the confinement energy. If such variations of the well width occur on a macroscopic scale, for
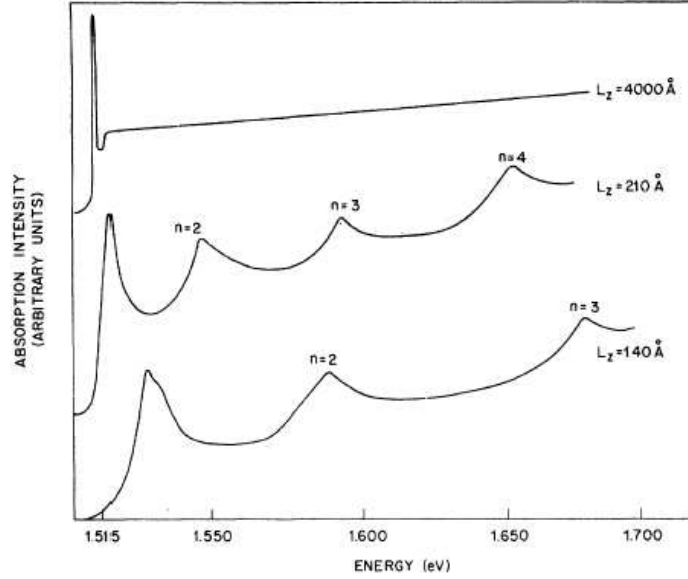
Figure 1.2: Absorption spectrum of GaAs/Al$_x$Ga$_{1-x}$As quantum well structure for different well widths, L_z. (From Ref. [19])

example the size of the laser excitation spot, the excitation laser will illuminate the sample over sites with different well widths each with its own confinement energy, and as a result a smearing of the luminescence line will be observed. The rougher the structure, the broader the luminescence line will be. Such broadening is known as inhomogeneous broadening.

If two quantum wells are grown close to each other with a thin barrier separating them, the resulting structure is called coupled quantum wells. Coupled, since the electrons and the holes, although from two separate wells, are not completely separated, and depending on the thickness of the barrier their wave functions may have considerable overlap. Using such coupled quantum wells structures for studying excitons has some advantages that could be exploited in the pursuit of experimentally achieving BEC. Arguably the most important or useful one is the ability to separate spatially the electrons and the holes. The separation occurs in the growth direction where the electrons reside in one of the quantum wells and the holes reside in the other. In the plane of the wells they could still be located in the same region but separated by the barrier between the wells. Such separation can be achieved

7
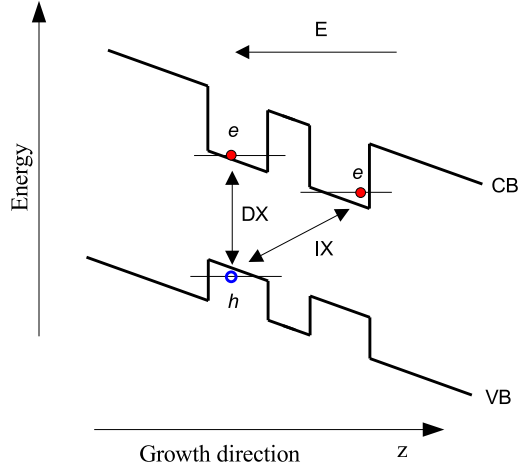
Figure 1.3: Direct (DX) and indirect (IX) excitons

by applying an electric field parallel to the growth direction (perpendicular to the plane of the wells). In this case the band structure will tilt by an amount proportional to the electric field, as shown in Figure 1.3. When electrons and holes are created, there will be an energetically lower state where an electron from one well will bind with a hole from the other and form the so-called "indirect" exciton (also called a dipole or interwell exciton), as opposed to the "direct" exciton in which the electron and the hole are in the same well. The indirect excitons have several advantages over the direct ones. Since the electron and the hole are separated spatially, the overlap of their wave functions will be reduced and in such a way the recombination rate will decrease, leading to increased lifetime of the excitons since the radiative lifetime is proportional to the overlap between the electron and the hole wavefunctions [22]. Such an increase of the exciton lifetime is advantageous in a BEC experiment where lifetimes longer than the thermalization time are required.

In type II quantum wells even in single well structures the excitons are naturally indirect since the electrons and the holes are confined to different spatial regions.

Creating indirect excitons is not without drawbacks, however. Although the semiconductor structure has high electrical resistance along the growth direction, it is not infinite. This means that, while applying voltage to create indirect excitons, there will be current,

8

albeit small, flowing through the quantum wells which will introduce a concentration of free carriers that will act as scattering centers for the excitons and in such a way reduce their mobility.

1.3   SUPERFLUID TRANSITION IN TWO DIMENSIONS

We have to point out that BEC in low dimensional structures is different from BEC in 3D systems. A gas of free noninteracting bosons with mass m at temperature T has the one particle distribution function

$$n_k = \frac{1}{e^{\beta(\varepsilon_k - \mu)} - 1} \, , \tag{1.6}$$

where $\varepsilon_k = \hbar^2 k^2 / 2m$ is the particle energy and $\beta = 1/k_B T$. The chemical potential μ is negative and is determined by the condition

$$\sum_k n_k = N \, . \tag{1.7}$$

The total number of particles can be written as an integral

$$N = \int g(\varepsilon) \frac{1}{e^{\beta(\varepsilon - \mu)} - 1} d\varepsilon \tag{1.8}$$

where $g(\varepsilon)$ is the one-particle density of states. $g(\varepsilon)$ depends on the dimensionality of the system, and for a 3D system it is

$$g(\varepsilon) = 2\pi \left(\frac{2m}{\hbar^2} \right)^{3/2} \sqrt{\varepsilon} \, . \tag{1.9}$$

In two dimensions the density of states is

$$g(\varepsilon) = \pi \left(\frac{2m}{\hbar^2} \right) = \text{constant} \, . \tag{1.10}$$

In 3D, the integral in (1.8) has an upper bound when $\mu = 0$, which is equal to the result (1.3). Extra particles added to the system must go into the ground state, forming the condensate. In 2D however, the integral has no upper bound and BEC is not possible. This was pointed out by Hohenberg [23]. A solution of this problem was suggested by Bagnato and Kleppner

9

[24]. Hohenberg's results were calculated for a Bose gas with constant potential confined by rigid walls. Bagnato and Kleppner have suggested that if the 2D gas is confined by a spatially varying potential then the integral above can converge (see also Nozieres [25]).

So creating a potential trap in a 2D system, in principle, makes BEC possible. Great effort was put in our lab to create such varying potentials in 2D systems. A success was achieved by using a pin to apply stress to the sample mounted between two metal plates [26, 27]. A more detailed account on the exact mounting of the sample and the way stress was applied will be given later.

Although BEC cannot occur in translationally invariant 2D systems, another type of transition is possible. Kosterlitz and Thouless [28, 29] pointed out that a two-dimensional gas can undergo a Kosterlitz-Thouless superfluid (KTS) transition, the critical temperature of which is given by

$$k_B T_c = \frac{\pi \hbar^2 \rho_s}{2m} \, , \tag{1.11}$$

where ρ_s is the superfluid density. The Kosterlitz-Thouless transition occurs in various systems such as the 2D classical XY model and superfluid helium on a surface [28]. In the two-dimensional XY model, for example, there is no long range order and a phase transition with mean magnetization cannot take place. There exists, however, a transition temperature below which metastable states corresponding to vortices are bound in pairs, and above that temperature they are free. Similarly, in a Kosterlitz-Thouless superfluid it is required that BEC occurs only in small regions of the system with locally defined condensate wavefunction but as a whole there is no long range order. Then in each region vorticity can be defined in terms of total phase change of the wavefunction along the region boundary. When the vortices in each region are considered, there will be no free vortices at low temperatures but only clusters with zero total vorticity. The KTS transition is also characterized by an infinitely differentiable specific heat at T_c thus making it infinite-order phase transition.

Fisher and Hohenberg [30] have considered the Kosterlitz-Thouless transition in a dilute 2D Bose gas and have found that the critical temperature depends on the particle density

as

$$T_c \approx \frac{4\pi\hbar^2\rho}{2m\ln\ln(1/\rho a^2)} \, , \qquad (1.12)$$

where a is the range of the interactions between the particles and ρ is the total density of the particles.

A possibility of superfluidity of a 2D system of spatially separated electrons and holes was envisioned first by Lozovik and Yudson [31]. They did not speak explicitly about excitons but rather considered the superconductivity of a system of spatially separated electrons and holes located in two semiconductor sheets separated by a dielectric layer. Fukuzawa [32] claimed the observation of KTS of indirect excitons in coupled GaAs quantum wells based on the narrowing of the luminescence peak with increasing electric field and sharp dependence of the full width at half maximum (FWHM) of the peak on the temperature. Other groups have also claimed evidence of KTS of excitons in 2D. Larionov have studied GaAs/AlGaAs/GaAs double quantum wells [33, 34, 35] and observed the appearance of a very narrow peak on top of the indirect exciton luminescence which disappeared at temperatures higher than 3.5 K. Butov have performed studies of single GaAs/AlGaAs quantum well [36] and a number of studies of double GaAs/AlGaAs quantum wells [37, 38] with claims of Bose stimulation of exciton scattering. We should also mention their observation of luminescence rings which were interpreted as evidence of a superfluid excitonic state [39, 40]. This effect will be discussed in detail in later chapters.

As mentioned earlier, no quantum well system is perfect. Even though the quality of the structures has increased in the past few years, there still exists inhomogeneous broadening due to disorder. This disorder can be, for example, from impurities, quantum well width variation, or dislocations. In a recent paper Berman discussed the problem of superfluidity of "dirty" excitons in a 2D system of coupled quantum wells [41]. The term "dirty excitons" is used to denote excitons in a system with disorder. Berman considered the random field of the disorder to be larger than the exciton-exciton interaction energy but smaller than the exciton binding energy. Using the coherent potential approximation he derived a correction
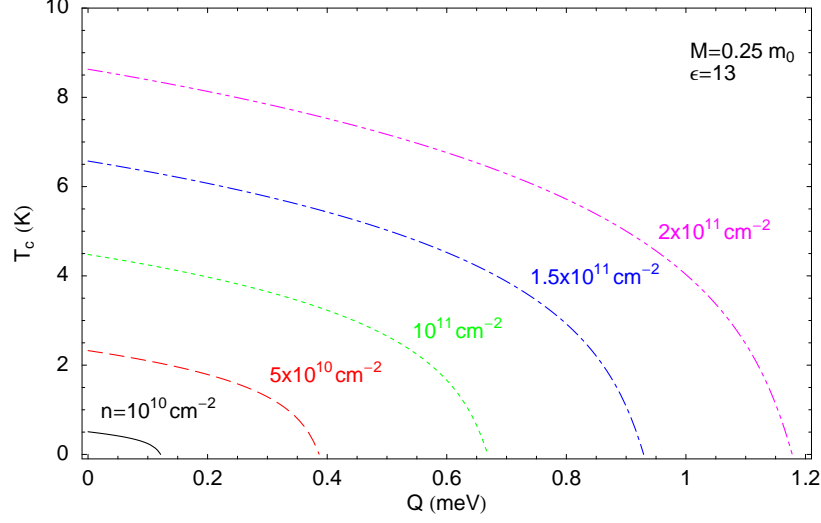
Figure 1.4: Dependence of the Kosterlitz-Thouless transition temperature T_c on the random field Q for different exciton densities n. After Ref. [41]

to the KTS transition temperature that takes into account the random field Q:

$$T_c = \left[\left(1 + \sqrt{\frac{32}{27}\left(\frac{MT_c^0}{\pi n'}\right)^3 + 1} \right)^{1/3} - \left(\sqrt{\frac{32}{27}\left(\frac{MT_c^0}{\pi n'}\right)^3 + 1} - 1 \right)^{1/3} \right] \frac{T_c^0}{2^{1/3}}, \qquad (1.13)$$

where

$$T_c^0 = \left(\frac{2\pi n' c_s^4 M}{3\zeta(3)} \right)^{1/3} \qquad (1.14)$$

and

$$n' = n - \frac{nQ}{2Mc_s^2}. \qquad (1.15)$$

In the above equations n is the density of the excitons, M is their mass and c_s is the speed of sound in the system. A plot of the Kosterlitz-Thouless transition temperature T_c vs. the random field Q shows that at fixed n, T_c decreases with increasing Q (Figure 1.4).

This result shows that even though the random field depletes the condensate, superfluidity is still possible albeit at a lower transition temperature.

1.4 EXPERIMENTAL

The general experimental setup is shown in Figure 1.5.

All experiments were performed in a Janis Vari-Temp optical cryostat where the temperature of the samples could be varied from 2 K to room temperature and higher. 2 K was achieved by submerging the sample in liquid helium and pumping the He vapor thus reducing the temperature of the superfluid liquid. Higher temperatures could be achieved by heating the samples locally using heating wire while cold helium vapor provided the needed cooling power for maintaining constant temperature.

A variety of light sources was used to excite the samples. A modelocked, frequency-doubled Nd:YAG laser (532 nm) with typical pulse duration of 50-80 ps was used to pump tunable dye lasers operating in the red or the near infrared region. The typical pulse width from the dye lasers was 5 ps with repetition rate 3.8 MHz or 76 MHz and maximum average power of 150 mW. For a large portion of the experiments, a small 4 mW continuous wave HeNe (632.8 nm) laser was used.

The luminescence from the sample was collected by Oriel MS257$^{\text{TM}}$ imaging spectrometer with 0.1-0.2 nm resolution. There were two detecting systems—an image intensified CCD camera and a multichannel plate (MCP) type photomultiplier tube (PMT), and the selection was performed by a flipping mirror. Since the spectrometer is of imaging type (Figure 1.6), the spatial information of the luminescence along the spectrometer slit is preserved in the spectrometer focal plane and this allows us to collect and observe simultaneously in real time spectral and spatial data on the CCD camera. With the PMT we could perform single photon counting with 100 ps time resolution when pulsed laser sources were used thus enabling us to take time-resolved data. A beamsplitter was used to pick off part of the laser light which triggered a fast photodiode, thus generating a start pulse, and a photon from the exciton luminescence arriving at the PMT served as a stop pulse. If data is collected long enough a histogram of the times between the start and the stop pulses could be built. This histogram is essentially a curve of the number of counts versus time and from it we can extract the temporal evolution of the excitonic light emission. We call this a "time trace."

The glass block in front of the spectrometer slit, shown in Figure 1.5, was used as a
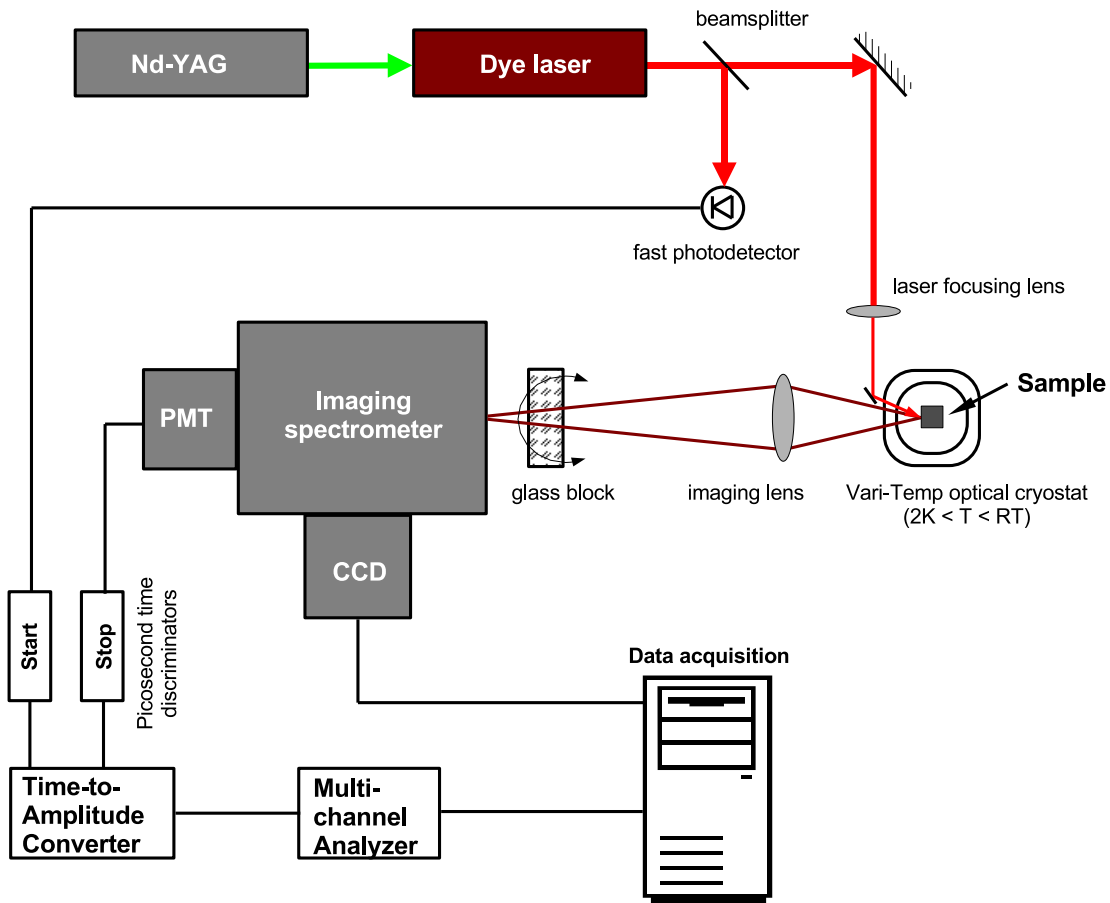
Figure 1.5: General experimental setup for time-resolved measurements
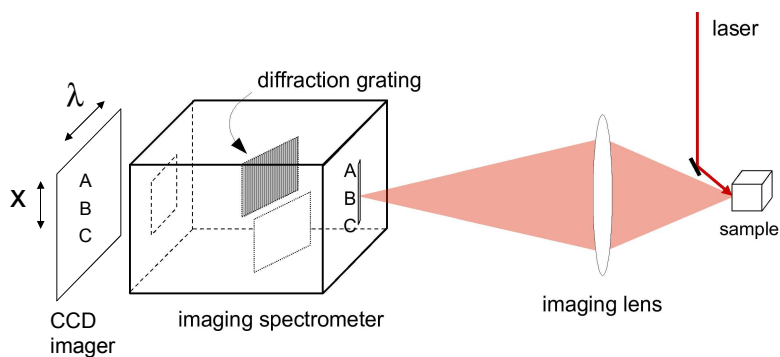
Figure 1.6: Imaging spectrometer. The spatial information along the front slit (*i.e.* the order of points A, B, C) is preserved in the image on the CCD.

scanning device. When turned about a vertical axis, different parts of the sample were imaged on the spectrometer slit. This allowed us to measure the spatial profile of the luminescence and identify any narrowing possibly related to BEC.

We can collect essentially two types of time-resolved data—time-resolved spectra and time-resolved profiles. A time-resolved spectrum measurement consists of a number of time traces, integrated for a certain amount of time, at different wavelengths, usually through a relatively narrow spectral range and with a small step. In such a way we build a data matrix with wavelength information in one dimension and temporal information in the other.

The time-resolved profile is similar to the time-resolved spectrum but in this case the wavelength of the spectrometer stays fixed and the glass block in front of the spectrometer slit rotates with small step thus imaging different parts of the sample for each time measurement. Time-resolved profiles are particularly useful for transport and diffusion measurements.

The samples were square pieces of thin wafer (usually 150 μm thick) with 3-5 mm sides. The way the sample was mounted is described in detail in [26] and [27]. Schematically the mount is shown in Figure 1.7. The sample was positioned between two polished metal plates that were spring loaded to ensure good contact at low temperatures. Because this is a mechanical contact, however, the contact resistance varied from run to run. The excitation of the sample and the collection of the luminescence were performed through a 1.5 mm hole in the bottom plate. A glass prism was used as a mirror. The top plate could also have a hole in the middle to allow a stressor pin to reach the back surface of the sample. This type of mounting allowed us to apply voltage bias across the sample and simultaneously create a potential trap for the excitons by applying stress with the pin. The method of using stress to create a trap is discussed in [26].
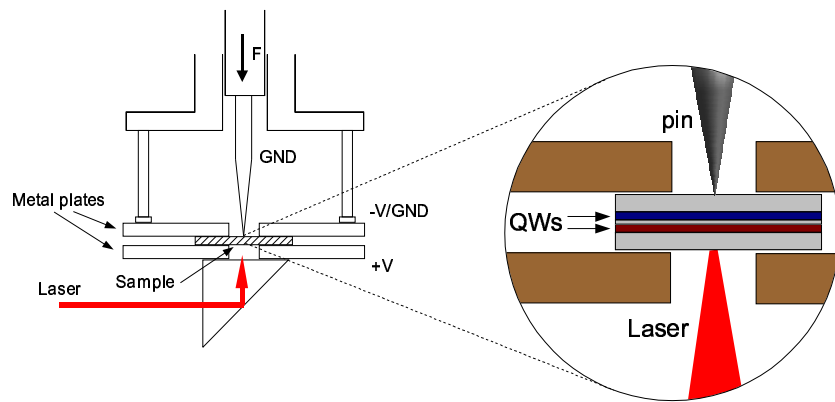
Figure 1.7: Experimental setup used for the mounting of the sample. It also allows us to apply stress to the sample.

2.0 THE $In_{0.1}Ga_{0.9}As$ COUPLED QUANTUM WELLS

2.1 SEMICONDUCTOR PROPERTIES

Most of the experiments were performed on high quality samples consisting of two 60 Å undoped $In_{0.1}Ga_{0.9}As$ coupled quantum wells separated by a thin 40 Å GaAs barrier. On the outside the structure is separated by 50 Å GaAs ledges from thick $Al_{0.32}Ga_{0.68}As$ layers. This structure along with its band structure (not to scale) is shown in Figure 2.1. The substrate and the capping layer are GaAs. The thicknesses of the $Al_{0.32}Ga_{0.68}As$ layers are 1000 Å on the substrate side and 300 Å on the capping layer side. The samples were grown using Molecular Beam Epitaxy by Loren Pfeiffer and Ken West at Bell Laboratories.

Previous coupled quantum well structures that were studied in the lab were based on GaAs where two GaAs quantum wells were separated by $Al_{0.3}Ga_{0.7}As$ barriers and the whole system was grown on GaAs substrate with GaAs capping layer. One disadvantage of such a system is that since the substrate and the quantum wells are grown using the same material, one has to excite the structure with light with energy above the band gap of that material and thereby creating photocarriers in the thick substrate and the capping layer. This will introduce current through the sample and will also lead to charge accumulation as described in [42]. It will also be difficult to separate the exciton luminescence from luminescence coming from the substrate. To avoid this, the quantum wells can be grown with material with band gap smaller than the rest of the structure, thus allowing the use of a laser with energy below the substrate band gap and avoiding the excitation of carriers in the substrate. This was one of the main reasons we chose $In_{0.1}Ga_{0.9}As$ as material for the quantum wells. The top of the valence band of $In_{0.1}Ga_{0.9}As$ lies around 20 meV above the valence band of GaAs and the conduction band is 163 meV lower than the one in GaAs [46]. This gives

17
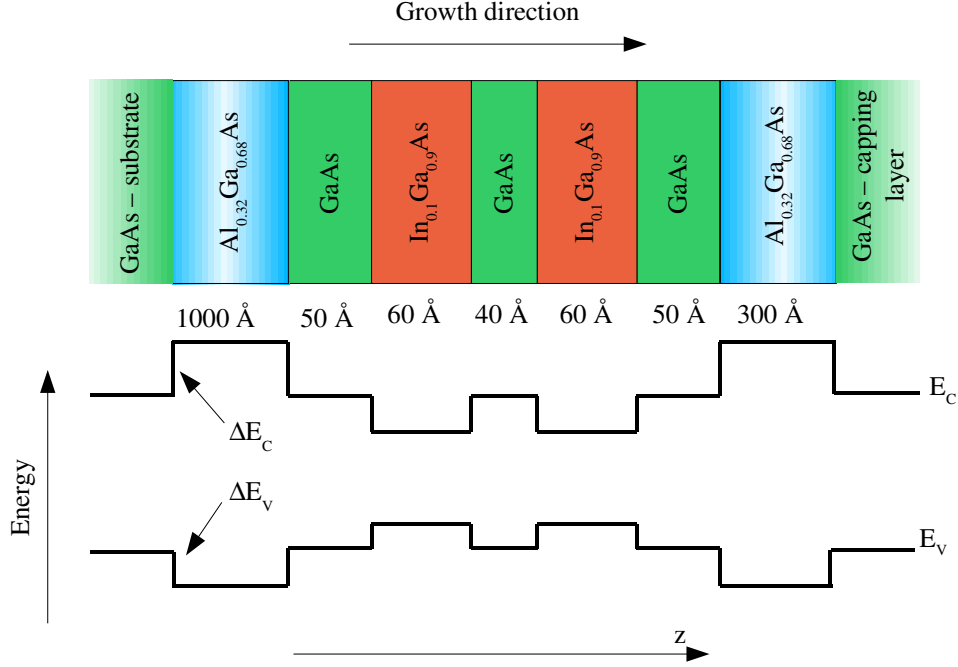
Figure 2.1: Coupled quantum wells structure used in the experiments

the opportunity for near resonant excitation of the excitons in the $In_{0.1}Ga_{0.9}As$ with a laser operating below the GaAs absorption edge. The concentration of indium was kept as low as possible in order to prevent big lattice mismatch with GaAs.

Some of the major properties of GaAs, InAs, AlAs and their alloys $In_{0.1}Ga_{0.9}As$ and $Al_{0.32}Ga_{0.68}As$ are shown in Table 2.1.

GaAs and AlAs crystallize in a zinc-blende type lattice. It has face-centered cubic symmetry where each atom of one type has four nearest neighbors of the other type located at the vertices of a tetrahedron. In reciprocal space, the top of the valence band of GaAs is located at the same place in **k**-space as the bottom of the conduction band, in this case the Γ point, *i. e.* the center of the Brillouin zone. This makes GaAs a direct gap semiconductor. In contrast, AlAs has the minimum of its conduction band at the X point of the zone, while the top of the valence band is still at the Γ point. Thus the Γ-Γ gap at the center of the zone is 3.13 eV and the Γ-X gap is 2.229 eV—AlAs is an indirect gap semiconductor. This means that at a certain concentration x, $Al_xGa_{1-x}As$ will have to change from direct to

Table 2.1: Material properties of GaAs, InAs, AlAs and their alloys, $In_{0.1}Ga_{0.9}As$ and $Al_{0.32}Ga_{0.68}As$, from [43] except where noted (l.a.=linear approximation).

Parameter	GaAs	InAs	$In_{0.1}Ga_{0.9}As$	AlAs	$Al_{0.32}Ga_{0.68}As$
E_g (eV)	1.5194	0.4180	1.376	2.229(ind.)/3.13(dir.)	1.9771 [45]
m_e (m_0)	0.067	0.0239	0.0615 (l.a.)	0.150	0.0869 [44]
m_{hh} (m_0)	0.51	0.35	0.501 (l.a.)	0.409	0.6332 [44]
m_{lh} (m_0)	0.082	0.026	0.076 (l.a.)	0.153	0.1056 [44]
a (Å)	5.6533	6.0583	5.6938	5.660	5.6556

indirect semiconductor. The exact concentration of Al at this crossover point is not firmly established but in most references it is assumed to be around $x = 0.45$.

The highest valence band of GaAs is degenerate and there are two hole masses defined by the curvature of the energy band with respect to $\mathbf{k}$. They are designated heavy and light hole masses. Quantum confinement in a narrow well lifts the degeneracy and two separate bands are formed. They have a very peculiar property—the heavy hole in the direction perpendicular to the well plane has light hole mass in direction parallel to the well plane. The same is true for the light hole as well. It has light hole mass in the direction of confinement and heavy mass in the other, as shown in Figure 2.2.

To describe fully the quantum well structure we need to know how the bands of the different materials align with each other, *i. e.* we need to know the band offsets between GaAs, $In_{0.1}Ga_{0.9}As$ and $Al_{0.32}Ga_{0.68}As$. There are numerous studies of $GaAs/Al_xGa_{1-x}As$ heterostructures and the band discontinuity values range between 60:40 and 90:10 for $\Delta E_c{:}\Delta E_v$ [44, pp. 180-190]. We accept an average value of $\Delta E_c(x) = (0.79 \pm 0.02)x$ for the $GaAs/Al_xGa_{1-x}As$ conduction band offset [44, p. 188]. Then for $x = 0.32$ this will give $\Delta E_c = 0.2528$ eV, and using the value for the band gap of $Al_xGa_{1-x}As$ from [45] we get $\Delta E_v = 0.2049$ eV, which gives band offset ratio $\Delta E_c{:}\Delta E_v$=55:45. It is different from the 60:40 ratio mainly because of the use of a different value for E_g of $Al_xGa_{1-x}As$.

The exact value of the band offsets between GaAs and $In_{0.1}Ga_{0.9}As$ is also not precisely
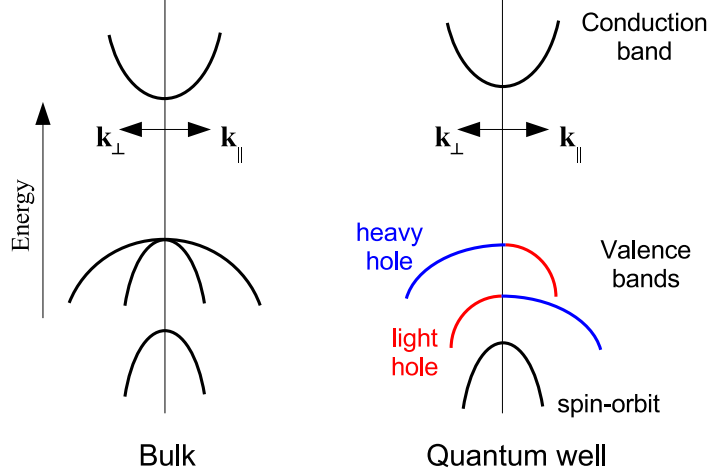
Figure 2.2: Effect of the quantum well on the band structure near the center of the Brillouin zone of GaAs. $\mathbf{k}_{\parallel}$ and $\mathbf{k}_{\perp}$ represent directions parallel and perpendicular to the quantum well plane [44].

established. From [46] we obtain $\Delta E_c = 0.163$ eV and $\Delta E_v = 0.0196$ eV.

2.2 THEORETICAL EXCITON PROPERTIES

Using these values for the band offsets we can now draw a somewhat realistic picture of our coupled quantum wells structure. A to-scale band structure is shown in Figure 2.3.

We can estimate the confinement energies of the electron and the hole in this structure. As a zeroth order approximation we can use the naive model of an electron and a hole in a single infinite quantum well. The energies of the electron and the hole are $E_e = \dfrac{\pi^2 \hbar^2}{2m_e L^2} = 170$ meV and $E_h = \dfrac{\pi^2 \hbar^2}{2m_{hh} L^2} = 21$ meV. Certainly, this very simple estimate doesn't work very well as it predicts confinement energies on the order of the depth of the wells. A better method is needed in order to obtain more realistic values. Since the structure is very complicated and straight-forward solution of the Schrödinger equation is not trivial, we will make several simplifications. First, we will consider only a one-dimensional problem,
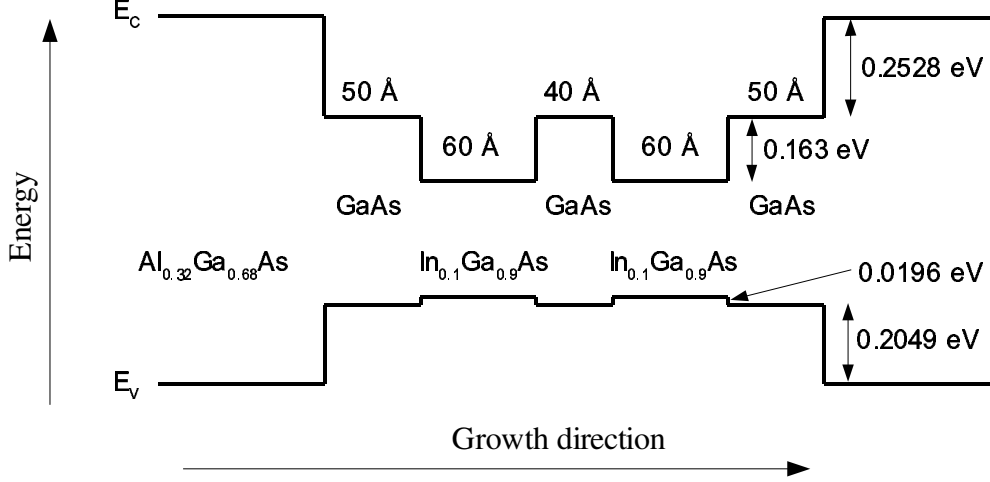
Figure 2.3: Band structure of the $In_{0.1}Ga_{0.9}As$ coupled quantum wells.

namely the confinement of the electron and the hole in the z-direction. In the plane of the quantum wells, the $x - y$ plane, we will assume that the particles are free. As a way to find the confinement energies we will employ a method of finding the bound states of a heterostructure proposed by Deck and Li [47]. The method is simple and is based on calculating the reflection coefficient of the particle from the first interface as a function of the particle energy and finding its poles, which will coincide with the bound states of the particle in that structure. We will summarize it below.

Let us consider a particle in a potential that consists of $n + 1$ regions (layers) each with thickness L_j and with constant potential V_j $(0 \leq j \leq n)$ (Figure 2.4). In each region the particle has mass m_j and wavevector k_j:

$$k_j = \sqrt{\frac{2m_j}{\hbar^2}(E - V_j)}, \tag{2.1}$$

where E is the total energy of the particle. For our calculation we assume the zero of energy to be at the bottom of the deepest well.

For zero external electric field we can assume that in each region the wave function has the form

$$\Psi_j(z) = a_j \exp(ik_j z) + a_j' \exp(-ik_j z), \tag{2.2}$$

21
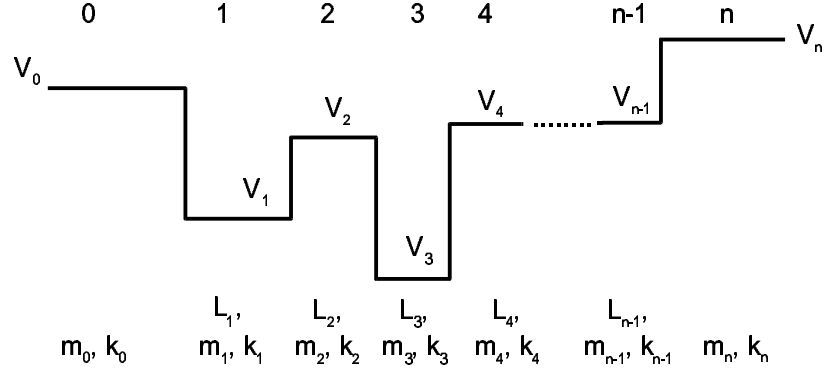
Figure 2.4: Heterostructure with $n + 1$ layers and n boundaries.

or, in other words, it is a superposition of plane waves. The continuity of the wavefunction and its derivative at each boundary i-j requires

$$\Psi_i(z) = \Psi_j(z) \tag{2.3}$$

$$\frac{1}{m_i} \frac{d\Psi_i(z)}{dz} = \frac{1}{m_j} \frac{d\Psi_j(z)}{dz}, \tag{2.4}$$

From these equations we can define at each boundary

$$S_{ij} = \frac{m_j k_i}{m_i k_j} \tag{2.5}$$

and

$$r_{ij} = \frac{S_{ij} - 1}{S_{ij} + 1}, \quad (i < j; \ i, j = 0, 1, \ldots, n) \tag{2.6}$$

22

Now we have $S_{01}, S_{12}, \ldots, S_{(n-1)n}$ and correspondingly $r_{01}, r_{12}, \ldots, r_{(n-1)n}$. Then we can define the recursive quantities:

$$r_{(n-2)(n-1)n} = \frac{r_{(n-2)(n-1)} + r_{(n-1)n} \, \exp(2ik_{n-1}L_{n-1})}{1 + r_{(n-2)(n-1)}r_{(n-1)n} \, \exp(2ik_{n-1}L_{n-1})} \tag{2.7}$$

$$r_{(n-3)(n-2)(n-1)n} = \frac{r_{(n-3)(n-2)} + r_{(n-2)(n-1)n} \, \exp(2ik_{n-2}L_{n-2})}{1 + r_{(n-3)(n-2)}r_{(n-2)(n-1)n} \, \exp(2ik_{n-2}L_{n-2})} \tag{2.8}$$

$$\vdots$$

$$r_{12345\ldots n} = \frac{r_{12} + r_{2345\ldots n} \, \exp(2ik_2 L_2)}{1 + r_{12}r_{2345\ldots n} \, \exp(2ik_2 L_2)} \tag{2.9}$$

$$r_{012345\ldots n} = \frac{r_{01} + r_{12345\ldots n} \, \exp(2ik_1 L_1)}{1 + r_{01}r_{12345\ldots n} \, \exp(2ik_1 L_1)} \tag{2.10}$$

$$R = r_{012345\ldots n} \tag{2.11}$$

It can be shown that R is the reflection coefficient of the particle at the interface 0-1. Obviously R is a complex function (in both meanings) of the energy of the particle E. It can be shown also that R has poles at the bound state values of E [47]. So if we plot $|R|^2$ vs. E we will obtain a graph with very sharp peaks at the bound states. Since the Q-factor of these peaks could be extremely high (sometimes $> 10^{13}$), the bound state energies can be obtained with very high accuracy from the positions of the peaks.

We can now apply the above procedure to our double quantum well system with values for the main parameters shown in Figure 2.3. The results for the electron, the heavy and the light holes are shown in Figure 2.5. On the right we have limited the horizontal axis only to the depth of the $In_{0.1}Ga_{0.9}As$ well which is 0.163 eV for electrons and 0.0196 eV for holes. The zero is always at the bottom of the well. The strong peaks are at 53.6 meV for the electron, 6.6 meV for the heavy hole, and 12.3 meV for the light hole. Adding the 1.376 eV band-gap for $In_{0.1}Ga_{0.9}As$ will give us the energy of 1.4362 eV for the e-hh exciton and 1.4419 eV for the e-lh exciton, not accounting for the binding energy of the exciton. On the left on Figure 2.5 the plot of $|R|^2$ is shown for the entire range of energies between the $In_{0.1}Ga_{0.9}As$ and $Al_{0.32}Ga_{0.68}As$ band edges. In that region the electron has 4 bound states while the heavy hole has 12. We have to point out that this calculation is not exact. The values of the band offsets are at best approximate since they are not precisely established.
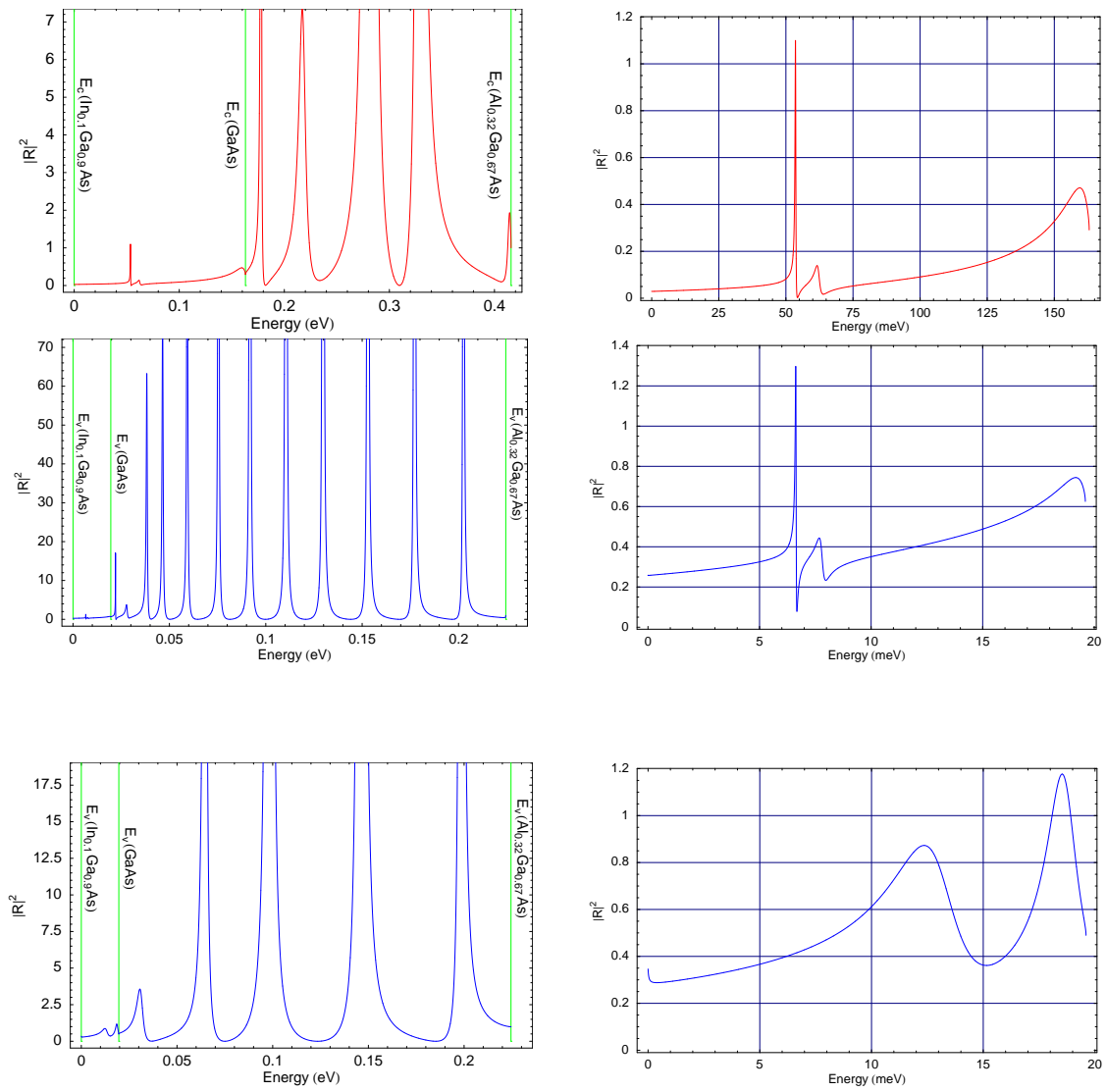
Figure 2.5: Bound state levels for the electron, the heavy hole, and the light hole (from top to bottom) in the double quantum well system. The right column shows an enlarged portion around the lowest levels.

In a recent paper Szymanska and Littlewood [48] have calculated the binding energies, the oscillator strength, and the exciton energies of two coupled quantum well structures subject to an electric field—$In_{0.1}Ga_{0.9}As/GaAs$ and $GaAs/Al_{0.33}Ga_{0.67}As$. The $In_{0.1}Ga_{0.9}As/GaAs$ system they have considered is equivalent to our sample—two 60 Å wells separated by 40 Å GaAs barrier and GaAs outside barriers. The $GaAs/Al_{0.33}Ga_{0.67}As$ is the one used by Butov's group [39]—two 80 ÅGaAs quantum wells separated by 40 Å $Al_{0.33}Ga_{0.67}As$ barrier and 2000 Å $Al_{0.33}Ga_{0.67}As$ outside barriers. Szymanska's method is based on the effective-mass approximation and is described in detail in [49]. For obtaining the results they used the following structure parameters: $\Delta E_g(In_{0.1}Ga_{0.9}As/GaAs)= 1070 \times 0.1$ meV $= 107.0$ meV, where 0.1 is the indium concentration; $\Delta E_g(GaAs/Al_{0.32}Ga_{0.68}As)= 1247 \times 0.32$ meV $= 399.04$ meV; conduction band offset ratio $Q_c = \Delta E_c/\Delta E_g$ of 0.65, which gives offsets $\Delta E_c(In_{0.1}Ga_{0.9}As/GaAs)= 69.55$ meV, $\Delta E_c(GaAs/Al_{0.32}Ga_{0.68}As)= 259.376$ meV, $\Delta E_v(In_{0.1}Ga_{0.9}As/Gaea)= 37.45$ meV, and $\Delta E_v(GaAs/Al_{0.32}Ga_{0.68}As)= 139.66$ meV. The effective masses used in the calculation are $m_e = 0.061m_0$, in-plane heavy hole mass $m_{hx} = 0.1m_0$, and out-of-plane heavy hole mass $m_{hz} = 0.339m_0$ for the $In_{0.1}Ga_{0.9}As$. The results from such calculation for $In_{0.1}Ga_{0.9}As/GaAs$ couples quantum structures are shown in Figure 2.6.

The dashed line and the diamonds represent the calculation for the $In_{0.1}Ga_{0.9}As/GaAs$ quantum well structure. The binding energy of the excitons decreases gradually from 6.5 meV at 0 V field to 3.5 meV at 4 meV/nm field. The oscillator strength (in the inset of Figure 2.6) also smoothly decreases. Since the inverse of the oscillator strength is proportional to the radiative excitonic lifetime, the increase of the electric field increases the lifetime of the excitons. The change of the binding energy for the $GaAs/Al_{0.33}Ga_{0.67}As$ structure (circles in the figure) is more dramatic, from 8.5 meV at zero field to about 4 meV at large fields. Calculation of the electron and hole wave functions shows that for the $In_{0.1}Ga_{0.9}As/GaAs$ structure, the electron and the hole are less confined than in the case of $GaAs/Al_{0.33}Ga_{0.67}As$ structure, due to the more shallow wells of the $In_{0.1}Ga_{0.9}As/GaAs$. Because of the broadness of the wave functions the exciton has 3D character in the absence of electric field. The separation of electrons and holes is much more dependent on the electric field in the $In_{0.1}Ga_{0.9}As/GaAs$ QW structure than in the $GaAs/Al_{0.33}Ga_{0.67}As$, where the quantum wells
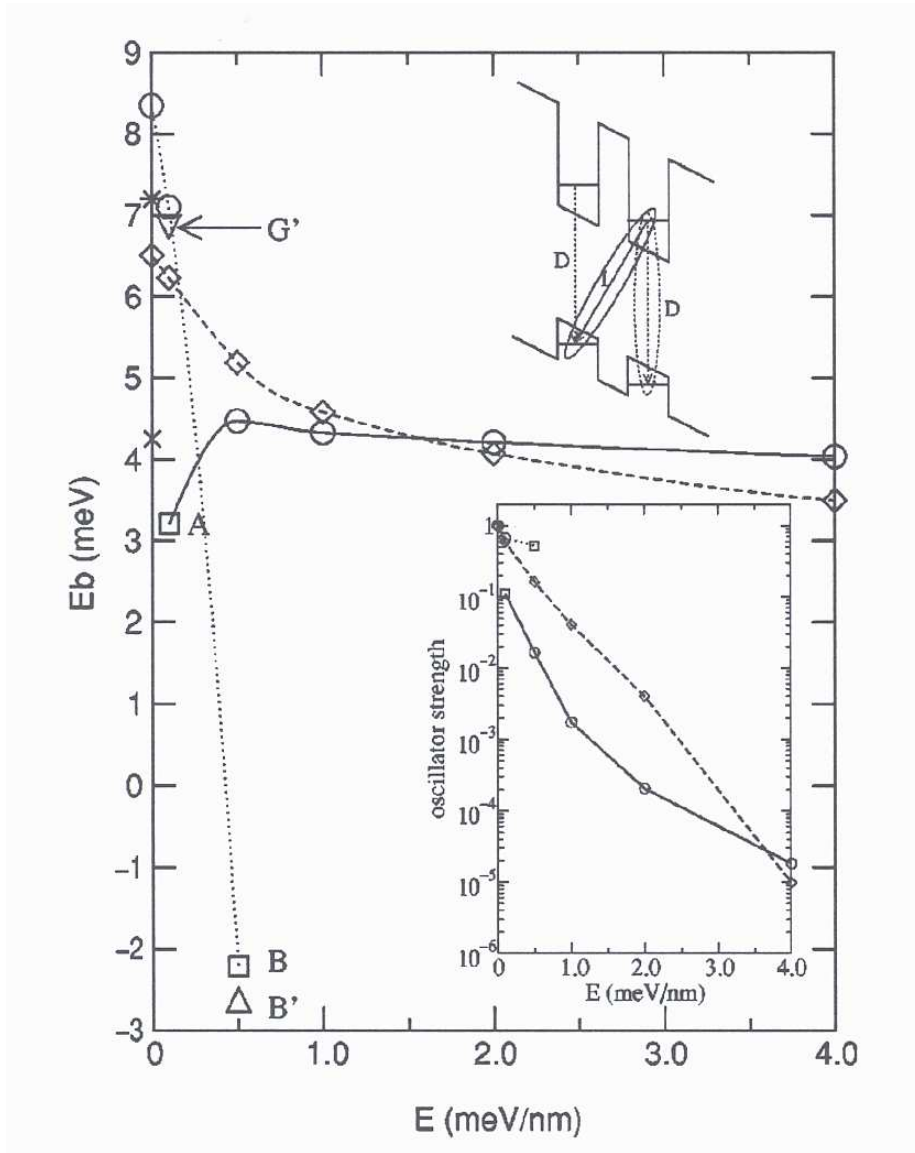
Figure 2.6: Binding energy of the ground-state exciton in coupled quantum wells structures as a function of the applied electric field: diamonds and dashed line—In$_{0.1}$Ga$_{0.9}$As quantum wells; solid line—indirect exciton in GaAs quantum wells; dotted line—direct exciton in GaAs quantum wells. Inset: Oscillator strength as a function of the applied field. From Ref. [48]
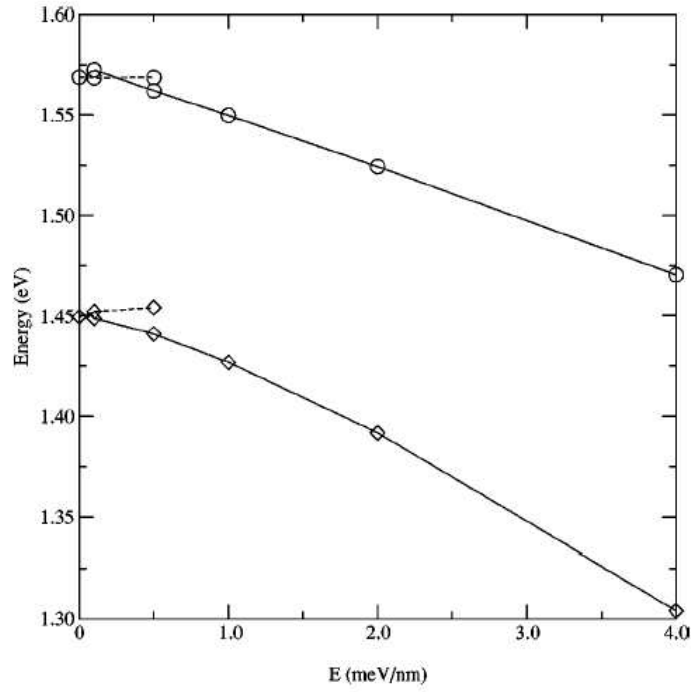
Figure 2.7: Energies of the indirect (solid line) and the direct (dashed line) excitons in $In_{0.1}Ga_{0.9}As/GaAs$ coupled quantum wells (lower curve) and $GaAs/Al_{0.33}Ga_{0.67}As$ coupled quantum well structure (upper curve). From Ref. [48]

are deeper and the barrier between them can provide effective confinement for the particles. Although the exciton binding energy decreases with the applied electric field, its value at high fields and low T is still high enough to claim that at low temperatures we have excitons and not a gas of separate electrons and holes.

Along with the exciton binding energies, Szymanska and Littlewood have also calculated the energy of the indirect exciton in both structures. The results for the $In_{0.1}Ga_{0.9}As$/GaAs (diamonds) and GaAs/$Al_{0.33}Ga_{0.67}As$ (circles) are shown in Figure 2.7. The energy of the direct exciton (at zero field) for the $In_{0.1}Ga_{0.9}As$/GaAs structure is calculated to be 1.45 eV, which compares very well with the experimental value of 852 nm = 1.455 eV. It is also close to the value we calculated in the beginning of the chapter. The main difference can be attributed to the slightly different structure parameters used in both models. At zero field there is splitting between the symmetric and the antisymmetric energy states in the wells which is too small to be resolved in our measurement. When the voltage is increased this splitting is transformed into direct and indirect states, as shown in the figure. As expected, the energy of the indirect exciton decreases with the increase of the electric field while the direct exciton (dashed line) remains at almost constant energy. At high fields the direct state is unpopulated since all excitons occupy the lowest energy state. It could get populated, for example at high temperature when there are excitons with energy high enough to occupy those states.

2.3   STUDY OF THE $In_{0.1}Ga_{0.9}As$ QUANTUM WELL SAMPLE

Chronologically, we used three different samples with the same 60-40-60 $In_{0.1}Ga_{0.9}As$/ GaAs double quantum well structure (60-40-60 refers to the thicknesses in Å of the wells and the barrier between them). They are summarized in Table 2.2.

The table shows the changes the design of the sample went through in order to make it more suitable to our specific purposes—study of indirect excitons.

Since the indirect excitons exhibit long lifetimes, they are our primary interest. To create

Table 2.2: The structure of the samples used in the experiments. S=substrate, CL=capping layer. The doping of the substrate and the capping layer is designated by i and n^+.

Designation	Sample structure						
	S	$Al_{0.32}Ga_{0.68}As$	GaAs	QWs	GaAs	$Al_{0.32}Ga_{0.68}As$	CL
sample-1	i	1000 Å	no	60-40-60	no	300 Å	i
sample-2	i	1000 Å	50 Å	60-40-60	50 Å	300 Å	i
sample-3	n^+	1000 Å	50 Å	60-40-60	50 Å	300 Å	n^+

indirect excitons we need to apply an electric field to the sample. This is usually done by placing electrical contacts on both sides of the sample and applying voltage between them. As mentioned earlier, in this case due to the finite resistance of the sample, current will flow, which will introduce additional scattering for the excitons (besides impurities and phonons) and this will ultimately reduce their mobility. So in order to minimize the current, the initial design of the sample included a thick 1000 Å $Al_{0.32}Ga_{0.68}As$ barrier on one side and 300 Å on the other side of the two 60 Å $In_{0.1}Ga_{0.9}As$ coupled quantum wells structure, thus separating it from the GaAs substrate and capping layer. $Al_{0.32}Ga_{0.68}As$ introduces a barrier of around 250 meV for the electrons in the conduction band and a 200 meV barrier for the holes in the valence band. The total thickness of the sample was 150 μm. This sample (sample-1) didn't have the GaAs ledges shown in Figures 2.1 and 2.3, and because of that the performance of the structure was quite poor due to the inhomogeneous broadening from the disorder and the lattice mismatch at the $Al_{0.32}Ga_{0.68}As/In_{0.1}Ga_{0.9}As$ interface. A typical CCD image of the luminescence is shown in Figure 2.8. The sample was excited with a 823 nm modelocked laser with power of 10 mW and repetition rate of 76 MHz. There wasn't any voltage applied to the sample and the exciton luminescence was observed at 859 nm. From this spectrum the measured inhomogeneous broadening was 4.3 meV.

In order to create indirect excitons with considerable population, the energy shift between the direct and the indirect (also called Stark shifted) states has to be greater than k_BT, a few meV for temperatures of the order of 10 K. For quantum well structure with thickness
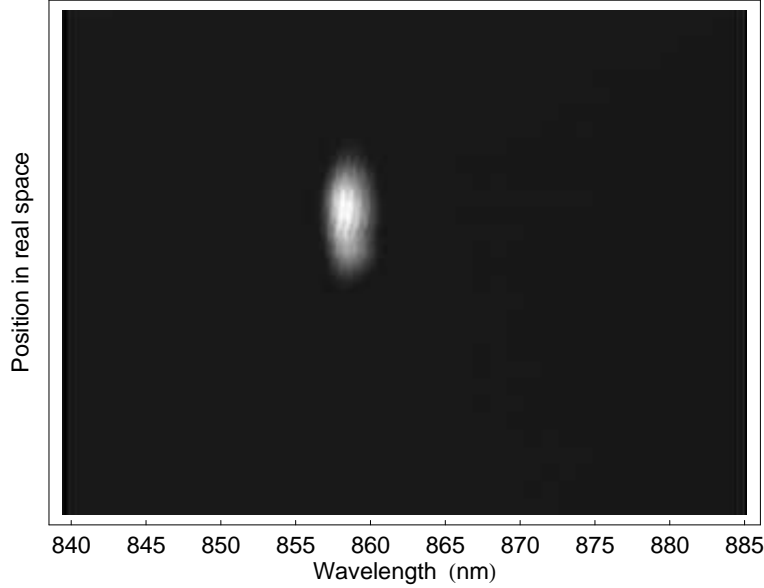
Figure 2.8: Image of the luminescence from sample-1 (without GaAs ledges).

of 160 Å (the wells plus the barrier between them) this corresponds to electric fields of the order of 10 meV/160 Å = 6.25 kV/cm. In our case this field corresponds to voltages of 100 V applied to the 150 μm thick sample. Indeed, the indirect exciton was observed at very high voltages—around 150 V. A CCD image of the luminescence at 200 V is shown in Figure 2.9. As with the direct exciton, the indirect line is very broad, with FWHM of 15 meV.

The very well-pronounced stripes in the images are due to interference—the 150 μm thick sample acts like a thin transparent plate for the 860 nm luminescence (the absorption edge of GaAs is around 820 nm). The sample was mounted between an indium tin oxide (In$_2$O$_3$-SnO$_2$ – ITO) coated glass plate on the side toward the laser and a brass plate on the other. The advantage of ITO glass is that it is transparent and provides electrical contact. The I-V curve is shown in Figure 2.10. Since most of the sample thickness is GaAs, this curve essentially represents the conduction of undoped GaAs.

We tried several different approaches to eliminate the current through the sample in order to reduce the inhomogeneous broadening. All evidence, however, showed that the broadening is due to disorder at the interface between the quantum wells and the barriers
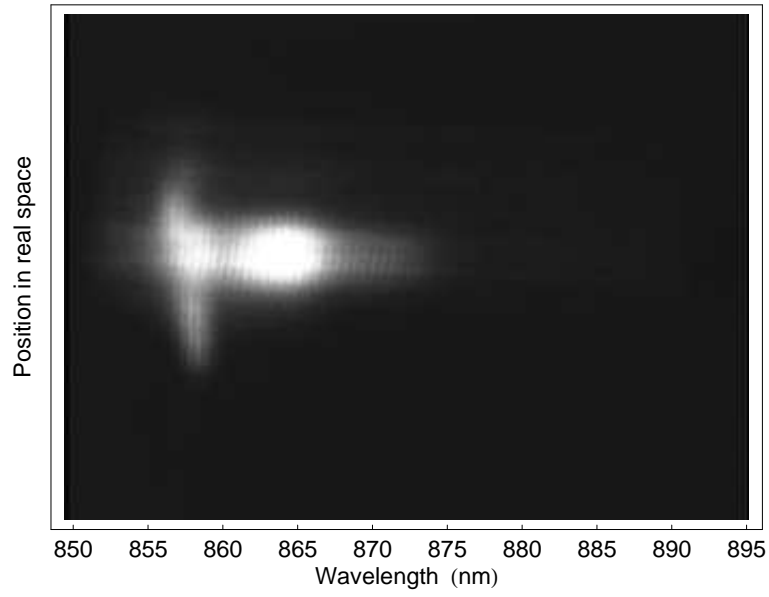
Figure 2.9: Image of the luminescence at 200 V from sample-1.
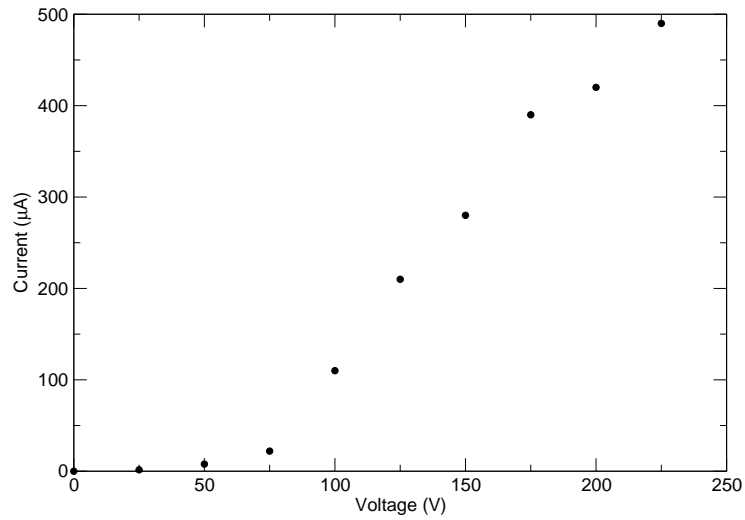
Figure 2.10: I-V curve for the InGaAs quantum wells sample-1.
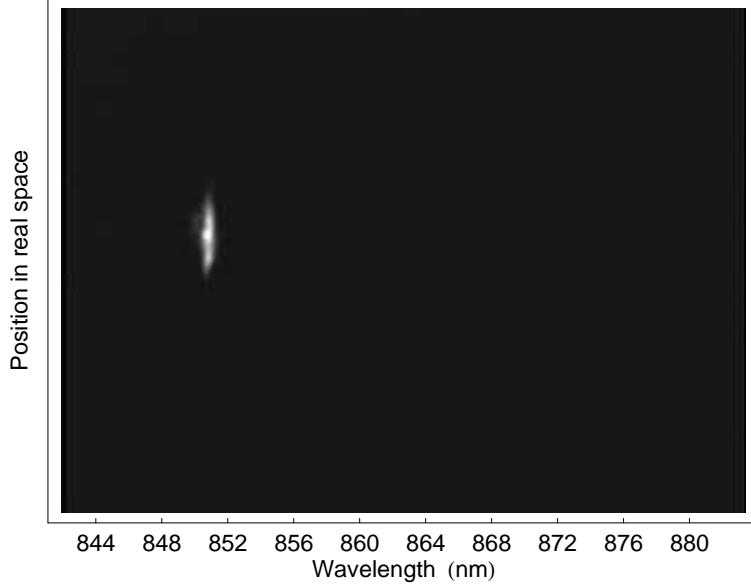
Figure 2.11: CCD image of the luminescence of the improved sample-2 (with GaAs ledges).

and not due to scattering off carriers. So in order to reduce the inhomogeneous broadening the design of the sample was changed and two 50 Å GaAs ledges were added on both sides of the quantum wells, as illustrated in Figure 2.1. A CCD image of the luminescence from this new sample is shown in Figure 2.11. There was drastic improvement in the quality. The inhomogeneous broadening was considerably reduced to 1.7 meV or less. Due to the very bad performance, sample-1 was no longer used. The difference in the position of the direct exciton luminescence from the two samples is due to the difference in the structures. In sample-1 the direct interface of $Al_{0.32}Ga_{0.68}As$ with the quantum wells introduces higher barriers leading to slightly higher confinement energies.

As we have mentioned earlier, Hohenberg [23] has shown that BEC cannot occur in an ideal 2D bosonic system while Bagnato and Kleppner [24] have suggested that in one and two dimensional systems BEC can take place in the presence of a confining or trapping potential. In previous experiments performed in the lab [26, 27], success has been achieved in creating such potential traps in quantum well samples using a stressor pin to apply inhomogeneous stress. In similar fashion we used a metal pin to push the sample from one side against

32
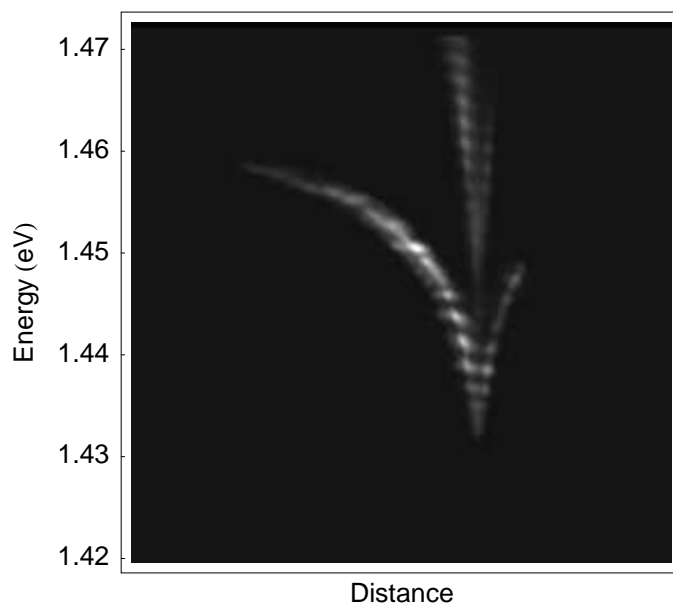
Figure 2.12: Shift of the exciton luminescence with applied stress

the observation hole on the other side, as illustrated in Figure 1.7. It was shown [26] that
in such geometry the hydrostatic and shear stress introduced in the sample contribute to
an overall negative shift of the exciton energy as opposed to the geometry in which the
sample sits flat against a glass slide in which case the energy shifts to higher values. Such a
negative shift in energy is evident in Figure 2.12. This is a very long exposure image of the
exciton luminescence taken with the CCD camera while the laser beam was scanned up and
down (effectively the imaging system sums a number of images—about 50—taken in rapid
succession). The image is rotated by 90 degrees to represent a plot of the energy change vs.
position on the sample. The maximum stress is at the contact point between the pin and
the sample surface. That point corresponds to the bottom of the potential trap where we
see maximum shift of the exciton line. The stress decreases with distance from the pin and
with it the shift of the observed luminescence. The very narrow faint line at higher energies
is due to the substrate luminescence.

With a potential trap created in such a way we could try to move the excitons toward
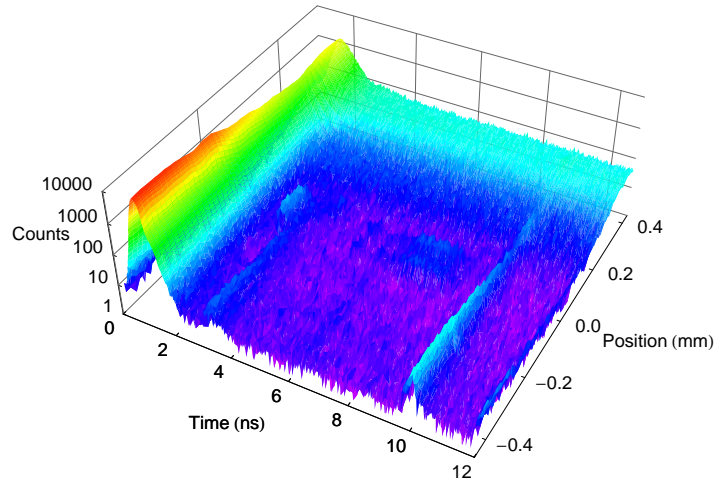
Figure 2.13: Time-resolved profile of the exciton luminescence in the stress well. The sample is excited at position -0.4 mm while the potential trap is at 0.4 mm.

the trap. This could be achieved by exciting the sample not exactly at the bottom of the potential well but slightly to the side, at the steep wall. This, in principle, will cause the hot excitons to fall down to the bottom of the well. A time-resolved profile of such an experiment is shown in Figure 2.13. One horizontal axis represents position on the sample surface while the other represents the time after the laser pulse. The shape of the stress well is the same as in Figure 2.12. The spectrometer was set at wavelength 863 nm, *i.e.* at the bottom of the well. The sample was excited by a 829 nm mode-locked laser and the excitation spot was at position -0.4 mm form a reference point (Figure 2.13), while the trap was at +0.4 mm. The laser spot was approximately 0.1 mm in diameter. The most prominent feature of Figure 2.13 is the long lifetime of the luminescence at the bottom of the trap while the excitons at the excitation spot have lifetime of one nanosecond or less. Although we see excitons at the bottom of the trap, we didn't observe any transport—the luminescence from the trap appears at the same time as the luminescence from the laser spot.

2.4 LUMINESCENCE ENHANCEMENT BY VOLTAGE

The stressor pin could also be used as one of the electrical contacts for applying voltage across the sample. In such a configuration the required high electric fields to create indirect excitons could be achieved at lower voltages due to the high curvature of the pin. Using this kind of setup we observed that applying voltage caused a sudden increase of the exciton luminescence. The effect under typical conditions is shown in Figure 2.14. The sample was excited exactly at the bottom of the potential well created by the pin (the laser shines exactly under the pin, shown in Figure 1.7) by a laser with power of about 3 mW. There was a voltage of 60 V applied between the bottom metal plate and the pin in Figure 2.14(a). The image shows the well pronounced potential trap created by stressor. The bright feature at high energies is due to bulk luminescence. Increasing the voltage to about 80 V resulted in an abrupt change of the luminescence pattern. The brightness of the exciton luminescence increased with a jump while the substrate luminescence decreased in brightness. The intensity of the exciton line remained approximately constant upon further increase of the voltage. A CCD image at 110 V is shown in Figure 2.14(b). There was also observed a slight shift of the luminescence to longer wavelengths which did not change with the increase of the applied voltage.

Another notable feature of this effect was the hysteresis with voltage. The voltage at which the enhanced light emission appeared was higher than the voltage at which it disappeared which hinted that there could be a self sustained effect at lower voltages. We have to point out that the effect was occurring only when the excitation was at the bottom of the potential trap (Figure 2.15). That point also corresponds to the highest electric field. Later experiments showed that the stress well wasn't necessary in order to reproduce the effect—just a good contact between the pin and the back surface of the sample was enough.

Naturally, the question of the nature of this enhanced light emission arises. One possibility is that lasing was taking place. We performed several tests to determine if that was the case. A measurement of the polarization of the luminescence showed that the light wasn't polarized. Visual observation of the sample and its projection on the spectrometer slit couldn't confirm the presence of bright light which was expected if lasing was taking
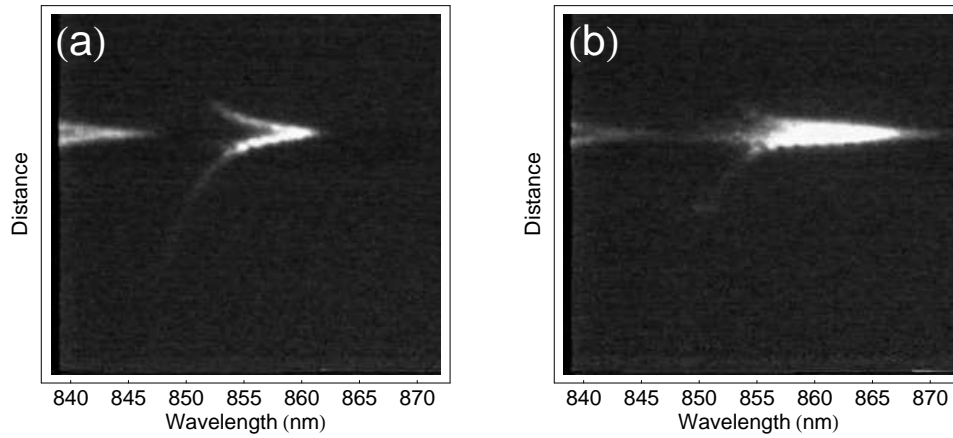
35

Figure 2.14: Enhanced light emission at high voltage: (a) V=60 V; (b) V=110 V. The jump in the luminescence brightness occurs at 80 V in this case.
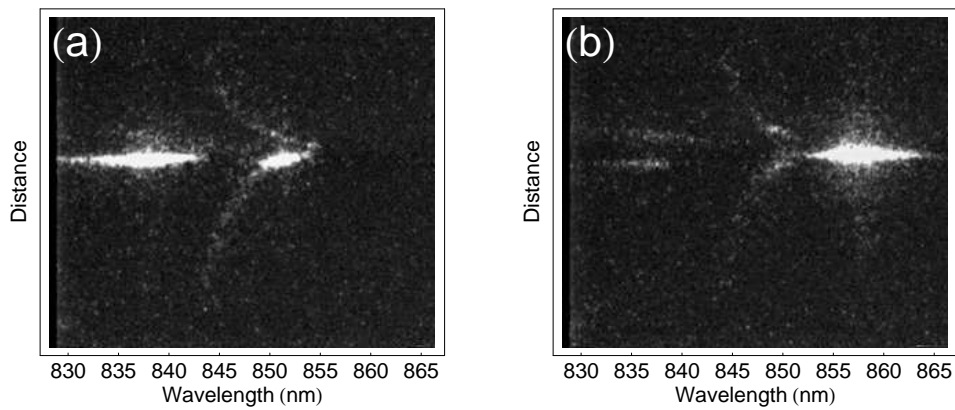
Figure 2.15: The effect of enhanced light emission occurs only when the laser excites the sample at the point of highest stress: (a) The laser is slightly off-center; (b) The laser is under the pin. V=141 V.

place. Nevertheless, this does not rule out lasing as an explanation of the enhanced light emission effect. It is possible that the high electric field at the pin's tip was causing electrical breakdown of the sample substrate, which led to strong current injection into the quantum wells.

2.5   DOPED $In_{0.1}Ga_{0.9}As$ SAMPLE

The design of sample-2 proved to be quite successful and the sample had indeed very good performance with respect to the inhomogeneous broadening. However, using 200 V to create indirect excitons was not very practical so the design of the sample was modified and heavily n-doped GaAs was used for the substrate and capping layer. In such a way they become highly conductive and the voltage needed to create indirect excitons was effectively applied to the 1560 Å quantum wells/barriers region. Now with only a few volts applied across the sample the required high electric field across the QW region could be achieved. The change of the position of the indirect exciton versus the applied voltage for this sample is shown in Figure 2.16. There is an apparent increase in efficiency of creating indirect excitons at low voltages.

Again, our interest was centered around observing some transport of excitons. We performed a series of time-resolved measurements. A time-resolved profile of the luminescence is shown in Figure 2.17. There is a stress well similar to the one shown in Figure 2.12 and the spectrometer is set to a wavelength corresponding to the bottom of the trap. In this case the well is at 0° position of the scanner and the laser spot is at 2°. Several important features are noticeable. The lifetime of the exciton species is extremely short—less than 1 ns—and there isn't really any measurable transport. The failure to observe any transport of excitons has two main reasons—short exciton lifetime and low carrier mobility. While the exciton lifetime can be extended by increasing the voltage, it is still of the order of a few nanoseconds. The mobility of the exciton as well as the lifetime may be affected by the fact that the semiconductor material for quantum wells is an alloy with small concentration of indium in it which may introduce disorder and reduce the mobility and shorten
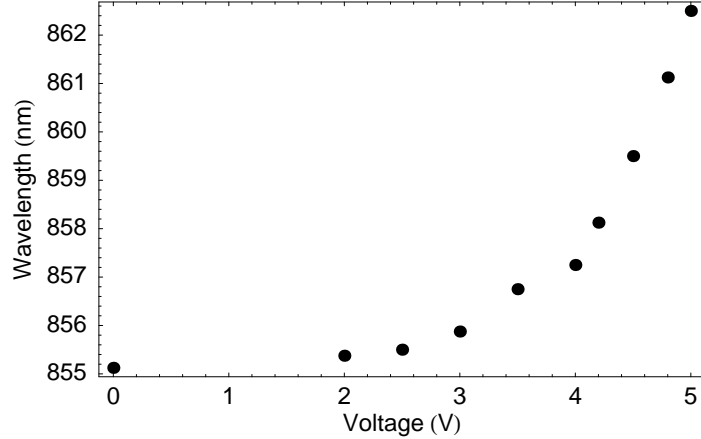
Figure 2.16: Indirect exciton position vs. the applied voltage for the sample with doped substrate (sample-3)

the lifetime of the excitons. Wang *et al.* [50] have performed a calculation of the mobility of a double GaAs quantum well system with an AlAs barrier separating the wells and have found a noticeable increase of the mobility as the barrier width is increased. Sakaki *et al.* [51] have measured the mobility in single GaAs quantum wells and observed L^6 power law dependence of the electron mobility on the well width. On the other hand, Xu *et al.* [52] have studied the dependence of the radiative excitonic lifetime on the well width for high quality GaAs/AlGaAs double quantum well systems. They also have observed an increase of the lifetime with the increase of the well width. These and similar observations suggest that the way to improve the performance of our quantum well structure probably is to increase the well width. Experiments with samples with 100 Å wells are currently under way.

Finally, on a more applied note, we performed a test to see if the quantum well structure could be used as a switching device. Since the exciton line shifts with the change of the applied voltage, it can be used to selectively change the absorption edge of the sample. For this experiment the sample was mounted in a way so that transmission measurements were possible. The laser was tuned to the indirect exciton wavelength for a selected voltage, in our case 5 V. In such a way when the the applied voltage was 0 V the laser energy was below the band gap and the sample was transparent and most of the light would go through which
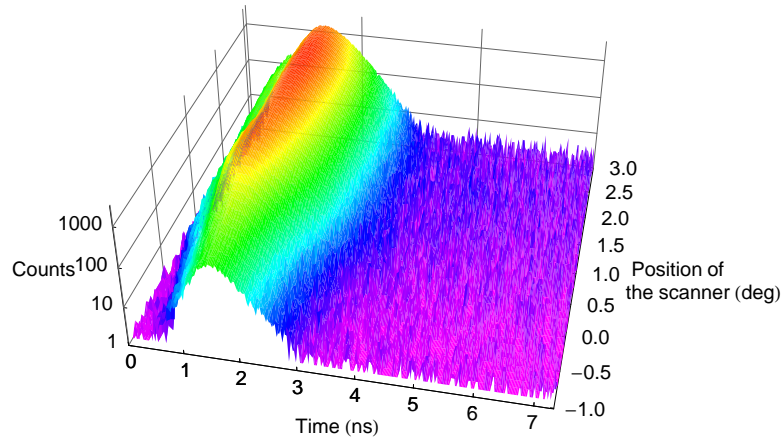
Figure 2.17: Time-resolved profile of the exciton luminescence of the doped sample in the presence of a stress well. The well is at 0° and the laser is at 2°.
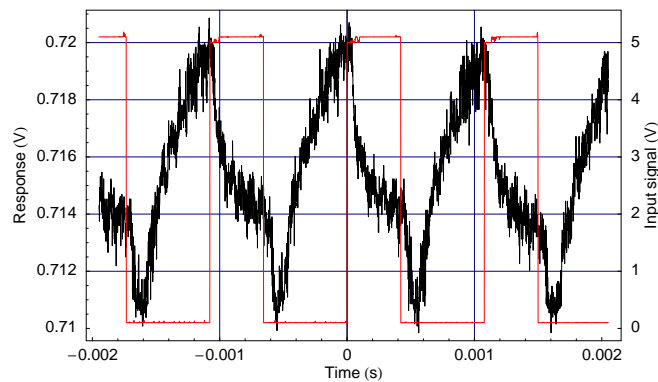
Figure 2.18: Using the quantum well structure as a switching device. Red trace: the input signal; black trace: the response of the system.

then could be detected by a photodiode. When, on the other hand, 5 V was applied, the laser resonantly excited the indirect exciton line and some of the light would be absorbed and we would see reduced photodiode current. The results from such an experiment are shown in Figure 2.18. The applied voltage (red on the figure) has a frequency of approximately 990 Hz. Indeed, the measured voltage through the diode shows modulation with the frequency of the driving signal. Obviously the performance is not very good—1 kHz is practically DC compared to the modern switching rates of GHz—but it demonstrates the concept that at least in principle quantum well structures could find use in optical switching devices.

3.0   MAGNETORESISTANCE OF COUPLED QUANTUM WELLS

Magnetoresistance is the property of certain materials to change their electrical resistance when subject to a magnetic field. Copper at 4 K, for example, can change its resistance 14 fold under fields of up to 10 T. It is an effect known for quite some time but measuring the change of the resistance of heterostructures in the presence of magnetic fields started in the early to mid 1980s when quality semiconductor structures could be grown. Choi *et al.* [53] studied the effect of the magnetic field on the tunneling current and the negative differential conductance through structures with multiple GaAs quantum wells. Magnetoresistance in superlattices was observed by Lee *et al.* [54]. They used a number of $GaAs/Ga_{0.7}Al_{0.3}As$ superlattice samples and measured the dependence of the longitudinal magnetoresistance on the temperature of the samples and the applied magnetic field. A quadratic increase of the resistance with the magnetic field was observed.

The appeal of the magnetic field to studies of Bose condensation of excitons in quantum wells is the possibility of creating potential traps using nonuniform fields.

This study [55] is a continuation of previous experiments with GaAs coupled quantum wells in low and high magnetic fields [56]. The original experiments were done at the National High Magnetic Field Laboratory in Tallahassee, Florida. The system was subject to magnetic fields as high as 30 T and the most striking result was the observation of a red shift of the luminescence line at low fields. The purpose of the current study was to reproduce the results of [56] at low fields and further investigate the red shift of the exciton line in $In_{0.1}Ga_{0.9}As$ coupled quantum wells and determine the cause of the effect. Since our interest was in the low magnetic field region, we decided to build a magnet that could be used in our laboratory conditions. It had to be able to produce a magnetic field of at least 1 T at the location of the sample and at the same time to be small enough to fit in our cryostat. The solution
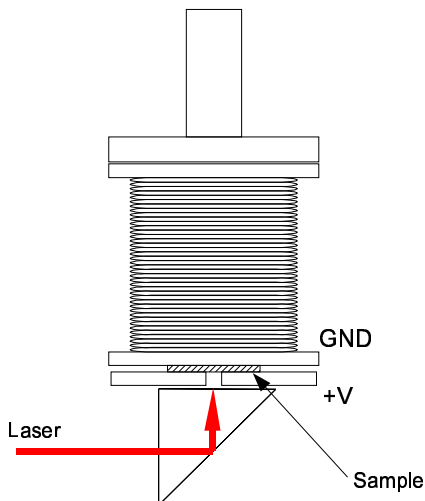
Figure 3.1: Setup used with the superconducting magnet.

was to use thin superconducting wire and make a solenoid compact enough to be mounted at the end of the manipulator and capable of generating 1 T. The design is shown in Figure 3.1. The magnet solenoid was 30 mm long and 28 mm in diameter. It was wound using type 54S43 multistrand superconducting wire with thickness 140 μm (including the Formvar insulation) manufactured by Supercon, Inc. The setup allowed us to apply simultaneously magnetic field and voltage bias to the sample.

A calibration curve of the magnet is shown in Figure 3.2. It was calculated using the geometry of the magnet—the number of layers of wire, the distance of each layer from the center, and the number of wounds per layer. On the vertical axis is shown the coefficient of proportionality between the magnetic field B and the electrical current I: $B = \alpha I$.

Negoita et $al.$ [56] observed that at low fields (up to 1 T) the indirect exciton line exhibited an unusual red shift (Figure 3.3). The shift was proportional to B^2 for both positive and negative small magnetic fields perpendicular to the plane of the wells. The red line on the figure is a B^2 fit to the data. When the magnetic field was increased further a blue shift was observed, which showed a linear dependence on the field, and it was attributed to the electron Landau level energy. The shift was similar to the observations of Krivolapchuk [57], although much stronger (20 meV vs. 5 meV). The magnitude of the shifts was dependent
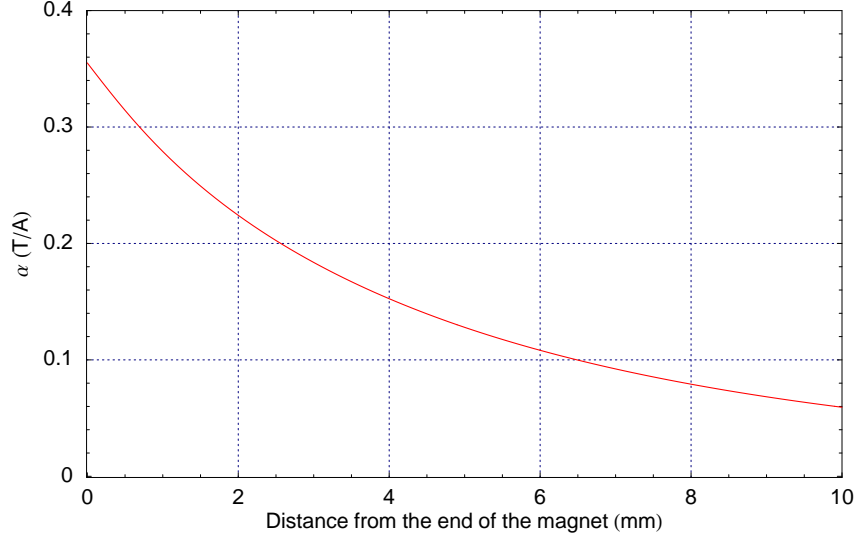
Figure 3.2: Calibration curve for the magnet. The distance is measured from the end of the solenoid (edge of the wires).

on the applied electric field–the higher the electric field, the stronger the observed shift with magnetic field.

The low magnetic field results were reproduced with the $In_{0.1}Ga_{0.9}As$ sample-3 with the doped substrate. This showed that the observed effects were not due to some specifics of the GaAs structure. The sample was mounted on the magnetic holder and kept at temperature of 2 K. It was excited with a modelocked laser with wavelength 846.5 nm which, is below the absorption edge of the GaAs substrate which makes it transparent. A shift with the magnetic field is shown in Figure 3.4. The fringes are due to interference from the transparent substrate. The position of the indirect luminescence peak vs. the applied magnetic field with 3.8 V bias is shown in Figure 3.5. The red line is a fit of B^2 to the data for $B < 0.2$ T. The data also shows one important feature of the effect—the shift is larger than the luminescence line width, which makes it easy to detect and measure.

The red shift of approximately 12 meV can be understood in terms of change of the magnetoresistance of the structure. Such an idea is supported by a measurement of the current through the sample, which changes over the same range of B as the spectral line
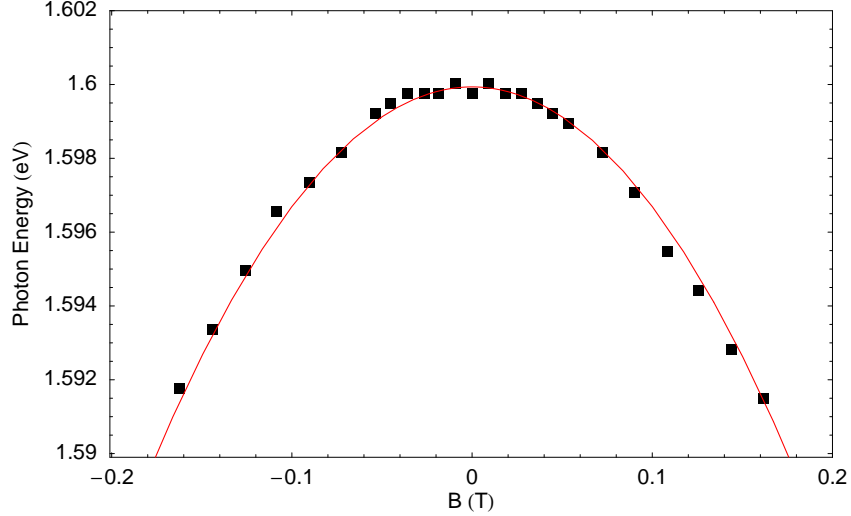
Figure 3.3: Shift of the photon energy of the luminescence of the indirect exciton in GaAs coupled quantum wells.

position. This is shown in Figure 3.6. Although the sample has very thick barriers ($\sim$1000 Å), there is a finite current due to the tilting of the bands when a high electric field is applied, which allows a non-negligible tunneling rate for the electrons. The narrowing of the indirect line observed in Figure 3.4 is in agreement with similar narrowing observed by Aksenov *et al.* [58] who studied single GaAs quantum well with 170 Å width in magnetic fields up to 6 T. The observed width of the exciton line decreased with increasing magnetic field. A fit to the shape of the line also showed that the Lorentzian contribution to the width (the homogeneous broadening) also decreases with the increasing the field.

A simple two-resistor model can be used to explain the relationship between the spectral shift and the current. The sample can be represented as two resistors connected in series—R_w, which represents the resistance of the quantum well region, and R_0, which represents the resistance of the substrate, capping layer and outer barriers, and the electrical contacts (Figure 3.7). R_w will depend on the tunneling rate through the inner barrier and will be much smaller than R_0, which includes the thick outer barrier resistance. With constant R_0, the voltage drop across the quantum well region, which will control the band tilt, is
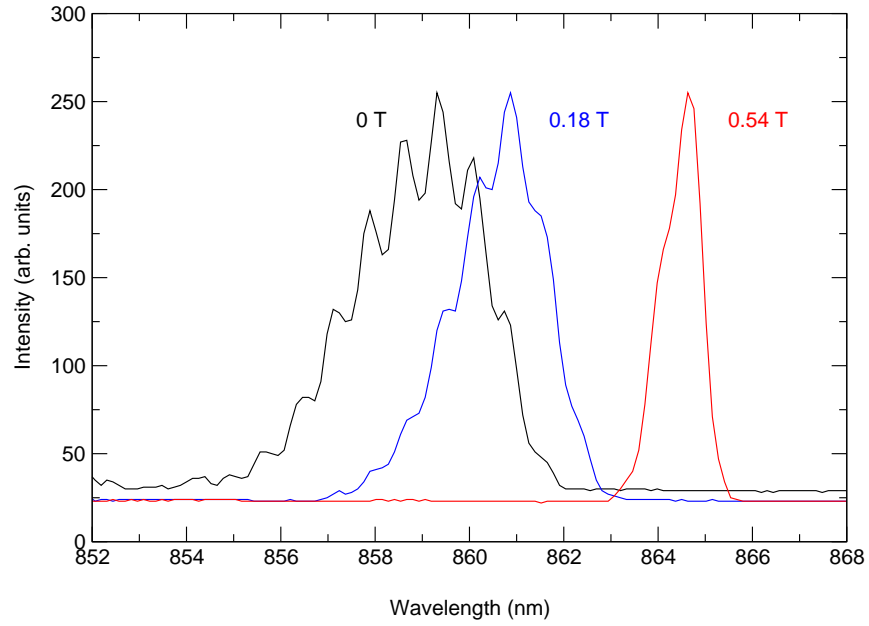
Figure 3.4: Indirect exciton luminescence shift with magnetic field in $In_{0.1}Ga_{0.9}As$ coupled quantum wells
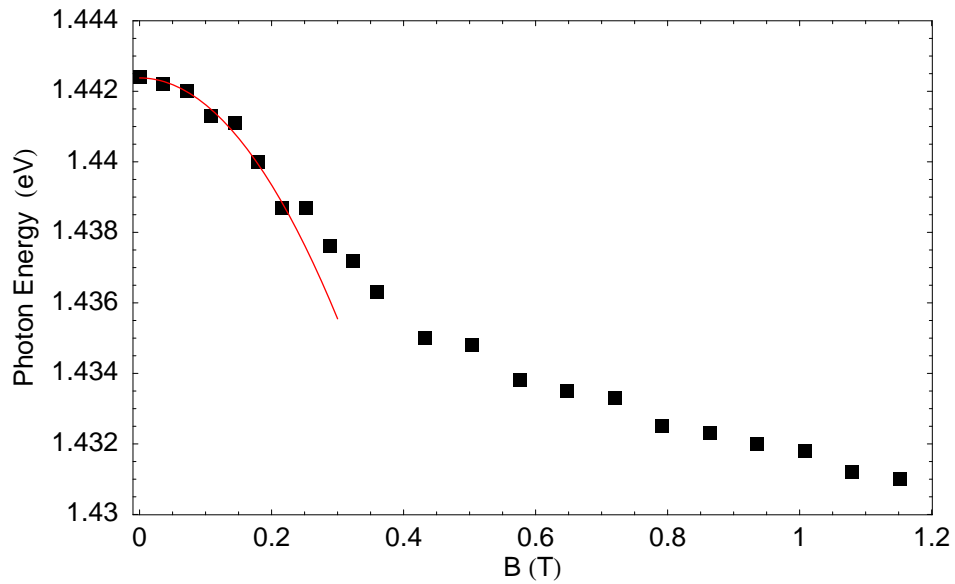
Figure 3.5: Luminescence line positions a function of the magnetic field. Sample is at T=2K with 3.8 V applied.
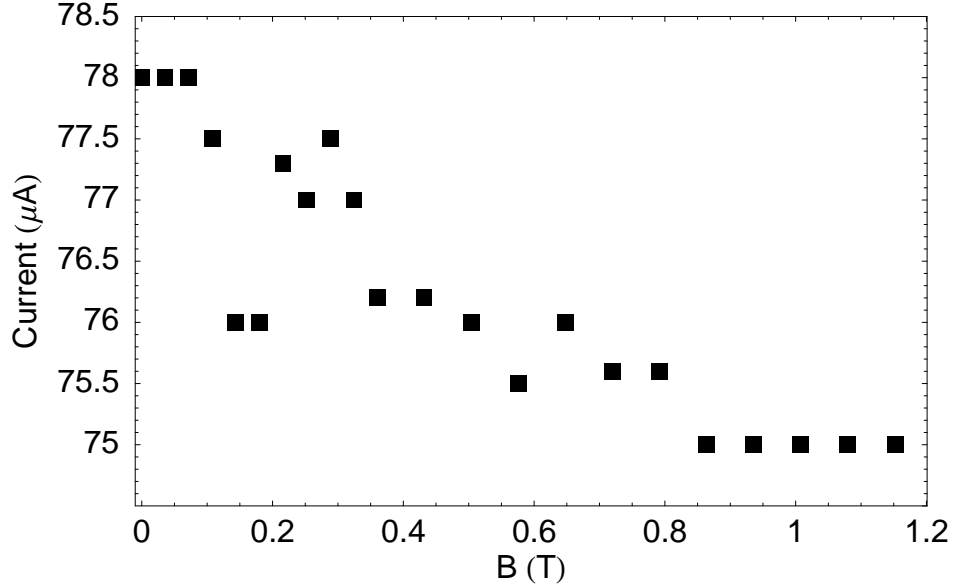
Figure 3.6: Current through the sample as a function of the magnetic field. V=3.8 V

$V_w = \dfrac{R_w V}{R_0 + R_w} = \dfrac{V}{1 + R_0/R_w}$, where V is the voltage across the whole sample. If R_w increases with magnetic field, the voltage across R_w will also increase and because of the quantum confined Stark effect, this will lead to a red shift of the indirect luminescence. In the opposite event, if R_w is decreased the red shift will be decreased also.

Although the positive magnetoresistance is a plausible explanation, there was at first no obvious reason why the resistance should change with magnetic field since there is no magnetic material in our samples. Also, the magnetic field is parallel to the applied electric field (perpendicular to the wells), in the same direction as the current. In collaboration with B. Laikhtman we proposed a model which is similar to the one suggested by Lee *et al.* [54] to explain the magnetoresistance of superlattices. While they observed a change of the magnetoresistance by a factor of up to 4 for fields of up to 9 T, the effect in our case occurs at much lower fields–less than 1 T.

Since the electric and the magnetic fields are parallel, one might think that the influence of the magnetic field on the current is small. There will be, however, carrier diffusion in the direction perpendicular to the magnetic field. In general, since the resistance parallel
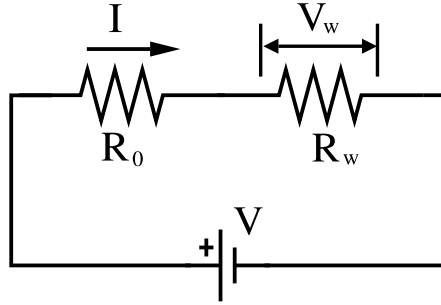
Figure 3.7: Two resistor model of the system of quantum wells and barriers

to the quantum wells is less than the resistance perpendicular to them (in which case the carriers must tunnel through the thick barriers), there will be some carriers that will diffuse in the plane of the wells, perpendicular to the magnetic field, and the diffusion constant can depend on the strength of the field.

While moving in the plane of the quantum wells, the carriers will encounter regions with different barrier thickness or height (due to variation of the In concentration). In general there is some level of disorder in all quantum well structures. The inhomogeneous line broadening is an indication of such disorder. In our samples it is quite small—of the order of 1-3 meV. Figure 3.4 is an example of the line width for the sample used. Usually this broadening is due to uneven well thickness over the excitation region. In our samples the quantum wells consist of approximately 10 monolayers (ML) of $In_{0.1}Ga_{0.9}As$ and 1 ML difference of thickness is 10% of the total well width, which corresponds to 6 meV broadening, which is much larger than the inhomogeneous broadening we see. This suggests that the disorder leading to the observed inhomogenous broadening cannot come from the well width variation. Our system consists of quantum wells composed of $In_{0.1}Ga_{0.9}As$ alloy and GaAs barriers, so any change of the concentrations in the alloy will result in change of the energy bands and the band offsets between the wells and the barriers which will lead to change of the barrier height felt by the carriers. Any such change will create regions where the tunnelling rate through the barriers, especially the thin 40 Å GaAs barrier between the wells, will be different. So with high diffusion rate in the plane of the wells, the carriers will be able to

find regions with high tunneling rate which results in low overall resistance.

On the other hand, when magnetic field is applied, the orbits of the electrons and the holes will be constrained to the Landau orbits, and the electrons are less likely to move to regions of high tunneling rate. Essentially, the Landau orbit causes the electrons to feel the average barrier height instead of local minima. The stronger the field the more constrained the carriers will be. In such a way the resistance of the sample will increase.

Miller and Laikhtman [59] have developed the theory of the magnetoresistance for superlattices and we use a similar model for quantum wells. In this model the quantum wells are between contacts with potentials U and $-U$. The potential of the first quantum well, separated by a barrier from the contact U, is $\phi_1(\mathbf{r})$ and the potential of the second quantum well is $\phi_2(\mathbf{r})$. We have assumed that the potential in the wells depends on the in-plane coordinate $\mathbf{r}$ because of the previously discussed nonuniformity of the barriers. The magnetic and electric fields are applied in the direction perpendicular to the quantum wells plane (z direction which is the same as the growth direction). If the conductances of the two outside barriers are $\Sigma_1(\mathbf{r})$ and $\Sigma_3(\mathbf{r})$, and the conductance of the middle barrier is $\Sigma_2(\mathbf{r})$ then we can write the current densities across the barriers as

$$j_{z1}(\mathbf{r}) = \Sigma_1(\mathbf{r})[U - \phi_1(\mathbf{r})], \quad j_{z2}(\mathbf{r}) = \Sigma_2(\mathbf{r})[\phi_1(\mathbf{r}) - \phi_2(\mathbf{r})], \quad j_{z3}(\mathbf{r}) = \Sigma_3(\mathbf{r})[\phi_2(\mathbf{r}) + U]. \quad (3.1)$$

The current conservation law in the wells gives

$$j_{z2} - j_{z1} = \nabla \hat{\sigma} \nabla \phi_1, \quad j_{z3} - j_{z2} = \nabla \hat{\sigma} \nabla \phi_2 \quad (3.2)$$

where $\hat{\sigma} \nabla \phi_{1(2)}$ is the in-plane electric current in the $1^{st}(2^{nd})$ well, ∇ is the in-plane gradient, and $\hat{\sigma}$ is the two-dimensional conductivity tensor of the well, which is assumed to be the same in both wells. It is antisymmetric, $\sigma_{xy} = -\sigma_{yx}$, and its diagonal elements depend on the magnetic field as

$$\sigma_{xx} = \sigma_{yy} \equiv \sigma_\parallel = \frac{\sigma_0}{1 + (\mu\, B/c^2)} \quad (3.3)$$

with σ_0 and μ being the conductivity and the mobility at zero field. Substituting j_{z1}, j_{z2}, and j_{z3} from Eq. (3.1) into Eq. (3.2) we find

$$\Sigma_2(\mathbf{r})[\phi_1(\mathbf{r}) - \phi_2(\mathbf{r})] - \Sigma_1(\mathbf{r})[U - \phi_1(\mathbf{r})] = \sigma_\parallel \nabla^2 \phi_1, \tag{3.4}$$

$$\Sigma_3(\mathbf{r})[\phi_2(\mathbf{r}) + U] - \Sigma_2(\mathbf{r})[\phi_1(\mathbf{r}) - \phi_2(\mathbf{r})] = \sigma_\parallel \nabla^2 \phi_2.$$

The measured current density can be defined as the current density through the intermediate barrier averaged over the spatial fluctuations

$$\langle j \rangle = \langle j_{z2} \rangle = \langle \Sigma_2(\mathbf{r})[\phi_1(\mathbf{r}) - \phi_2(\mathbf{r})] \rangle. \tag{3.5}$$

If we neglect that the resistance fluctuations of the barriers, $\Sigma_1 = \Sigma_3 \equiv \Sigma_0 = \text{const}$, $\Sigma_2 = \text{const}$, then $\nabla^2 \phi_{1(2)} = 0$ and Eqns. (3.4) and (3.5) lead to

$$\phi_1 = -\phi_2 = \frac{\Sigma_0}{2\Sigma_2 + \Sigma 1} U \tag{3.6}$$

and

$$j = \frac{2\Sigma_0 \Sigma_2}{2\Sigma_2 + \Sigma_0} U. \tag{3.7}$$

This expression is equivalent to total barrier resistance $1/\Sigma = 1/\Sigma_0 + 1/\Sigma_2 + 1/\Sigma_0$.

Our outside barriers are much thicker and much higher than the intermediate GaAs barrier, so their conductance is much smaller, $\Sigma_2 \gg \Sigma_1, \Sigma_3$. This allows us to neglect Σ_1 and Σ_3 in Equation (3.4) which is reduced to

$$\Sigma_2(\mathbf{r})[\phi_1(\mathbf{r}) - \phi_2(\mathbf{r})] - \Sigma_1(\mathbf{r})U = \sigma_\parallel \nabla^2 \phi_1, \tag{3.8}$$

$$\Sigma_3(\mathbf{r})U - \Sigma_2(\mathbf{r})[\phi_1(\mathbf{r}) - \phi_2(\mathbf{r})] = \sigma_\parallel \nabla^2 \phi_2.$$

If we subtract one of these equations from the other we get

$$2\Sigma_2 \phi - \sigma_\parallel \nabla^2 \phi = (\Sigma_1 + \Sigma_3)U \tag{3.9}$$

where $\phi = \phi_1 - \phi_2$. But according to Eq. (3.5)

$$\langle j \rangle = \langle \Sigma_2 \phi \rangle \tag{3.10}$$
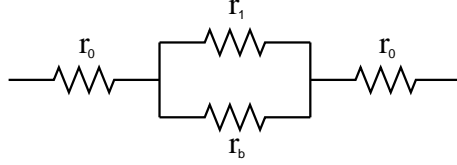
Figure 3.8: Resistor model of the quantum well structure with the inner barrier resistance replaced by two resistors.

so Equation (3.9) is sufficient to calculate the average current. According to it the average current is linear in fluctuations of Σ_1 and Σ_3, so these fluctuations are averaged and we can substitute $\Sigma_1 = \Sigma_3 = \Sigma_0$. Then Eq. (3.9) becomes

$$2\Sigma_2\phi - \sigma_\parallel \nabla^2 \phi = 2\Sigma_0 U \tag{3.11}$$

If the fluctuations of Σ_2 are small, the average current $\langle j \rangle$ can be calculated. But in the experiment the resistance of the QW structure changes by a factor of three, so the conductance fluctuations are significant. The analytical solution of Eq. (3.11) is difficult and the unknown statistics of the fluctuations imposes additional problems. So instead of trying to solve it analytically we employ a simple model where the circuit of Figure 3.7 is extended as shown in Figure 3.8. Here the outside barriers have resistance r_0, the average resistance of the second intermediate barrier is r_b, and r_1 is the sum of the in-plane resistance and the minimum resistance of the barrier, r_m. The in-plane resistance can be written as $l^2/\sigma_\parallel$, where l is the characteristic length of the barrier conductance fluctuations. Then the resistance of the intermediate part of the structure can be written as

$$\frac{1}{R} = \frac{1}{r_b} + \frac{1}{r_m + l^2/\sigma_\parallel} \tag{3.12}$$

$\sigma_\parallel$ can be substituted from Eq. (3.3) and the above becomes

$$\frac{1}{R} = \frac{1}{r_b} + \frac{1}{r_m + r_\parallel} \left[1 + \frac{r_\parallel}{r_m + r_\parallel}(\mu B/c)^2\right]^{-1} \tag{3.13}$$

where $r_\parallel = l^2/\sigma_0$.

When the magnetic field is low $[r_\parallel/(r_m + r_\parallel)](\mu B/c)^2 \ll 1$ and Eq. (3.13) becomes

$$\frac{1}{R} = \frac{1}{r_b} + \frac{1}{r_m + r_\parallel} - \frac{r_\parallel}{(r_m + r_\parallel)^2}(\mu B/c)^2 \qquad (3.14)$$

The minimum resistance at $B = 0$ is simply the two resistors, r_b and $r_1 = r_m + r_\parallel$, in parallel: $R_{min} = r_b(r_m + r_\parallel)/(r_b + r_m + r_\parallel)$.

At high magnetic fields, on the other hand, $[r_\parallel/(r_m + r_\parallel)](\mu B/c)^2 \gg 1$ and Eq. (3.13) leads to

$$R = \frac{r_b r_\parallel}{r_\parallel + r_b(c/\mu B)^2} \qquad (3.15)$$

with maximum resistance $R_{max} = r_b$ as B approaches infinity.

One of the main concepts of the model of positive magnetoresistance is that there are regions in the intermediate barrier with lower resistance for the carriers. It is then a legitimate question to ask what happens when $r_m = r_b$, *i. e.* when the resistance variations of the barrier are smoothed out. According to Eq. (3.13) there will be some magnetoresistance present. Obviously the model breaks down in this limit. We can think of it in another way, however. The difference $r_b - r_m$ represents some characteristic distance the carriers must travel in order to find a place with substantially lower resistance–the higher the difference, the "rougher" the barrier is and the shorter the distance the carrier must travel. When $r_b - r_m$ decreases, the characteristic distance increases and as r_m approaches r_b, the distance the carriers must travel in the lateral direction in order to see changes of the resistance approaches infinity. So in principle, one might say that there will be magnetoresistance even as r_m approaches r_b but in this case it should be considered an infinite current sheet with infinite time for the carriers to diffuse.

To fit the theory to the experimental data, we use $E = E_0 - IR$, where E is the energy of the indirect exciton luminescence, E_0 is the energy of the direct, unshifted line, I is the current through the sample, which we assume constant, since it changes less than 4% as shown in Figure 3.6, and R is the resistance. From Eq. (3.13) we have

$$R = r_b\frac{r_m + r_\parallel + r_\parallel(\mu B/c)^2}{r_b + r_m + r_\parallel + r_\parallel(\mu B/c)^2} \qquad (3.16)$$
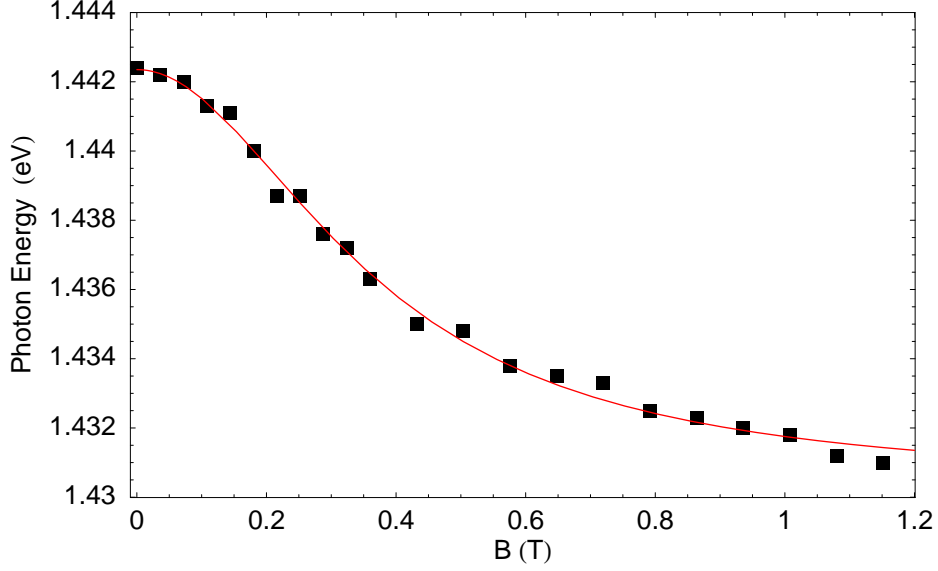
Figure 3.9: Fit of the magnetoresistance theory to the data from Figure 3.5

with the use of which IR can be rewritten as

$$IR = a\frac{1 + bB^2}{1 + dB^2} \tag{3.17}$$

with

$$a = Ir_b\frac{r_m + r_\parallel}{r_b + r_m + r_\parallel}, \quad b = \frac{r_\parallel}{r_m + r_\parallel}(\mu/c)^2, \quad d = \frac{r_\parallel}{r_b + r_m + r_\parallel}(\mu/c)^2. \tag{3.18}$$

Then

$$E = E_0 - a\frac{1 + bB^2}{1 + dB^2} \tag{3.19}$$

where E_0, a, b, and d are fit parameters. This system is underdetermined, however, (it has more fit parameters than degrees of freedom), and as such the parameters are linearly dependent and their values are strongly dependent on the starting conditions of the fit. To remedy that we rewrite the above equation as

$$E = E_0' - \frac{b'B^2}{1 + dB^2} \tag{3.20}$$

where $E_0' = E_0 - a$ and $b' = a(b - d)$. This can be fitted easily and the fit to the data from Figure 3.5 is shown in Figure 3.9. It implies parameter values $E_0' = 1.4423 \pm 0.0001$ eV, $b' = 0.089 \pm 0.006$, and $d = 7.4 \pm 0.5$.

One may ask what is, if any, the practical application of this effect. While not very strong, it is still a measurable effect of the magnetic field on the resistance of the sample. We can imagine a local magnetic probe where the field is measured by shining focused laser light and the shift of the exciton line is recorded. Or even obtaining a broad picture of the local magnetic field by flooding the sample area with light. In GaAs the effect appears to be limited to low temperatures but in other materials with more deeply bound excitons, the same effect could exist at higher, even room temperature.

4.0 RING STRUCTURES IN QUANTUM WELLS

Along the way to achieve BEC one wants to use higher exciton densities and low temperature in order to reach the required critical density for the specific temperature. In that case, in order to create relatively "cold" excitons, usually a resonant excitation is used, *i.e.* exciting the direct excitonic line resonantly or as close as practically possible. Probably this is the reason why the effect which we will discuss in the next chapters was never seen before although coupled quantum wells have been studied for a long time. Instead of driving the sample hard with resonant excitation, this effect requires extremely low powers and non-resonant laser which can excite the structure above the band gap.

We used a CW HeNe (632.8 nm) laser to excite the doped $In_{0.1}Ga_{0.9}As$ sample (sample-3 from Table 2.2) at 2 K very high above the band gap of the GaAs substrate and thus creating hot excitons that can fall into the quantum wells. Using very low power this excitation produced an extremely unusual effect [60]. When voltage was applied to the sample we observed an indirect exciton line that, as usual, shifted with voltage, but at around 2 V two bright spots appeared above and below the excitation spot, and the distance between them could be varied by changing the applied voltage. A typical image is shown in Figure 4.1. The laser power is 2 mW and the applied voltage is 1.5 V. It should be noted that since the spectrometer shows just a thin spatial slice of the actual luminescence pattern projected on its slit, the actual image was determined to be a ring around the central luminescence spot. This was verified by moving the imaging lens (and thus the image) from side to side and observing the spots moving closer to each other and finally merging. Later, we took images by projecting the luminescence directly on the CCD camera through a narrow-band spectral filter without the use of the spectrometer. Such an image is shown in Figure 4.2 and is the actual shape of the luminescence on the sample. Indeed the bright spots are part
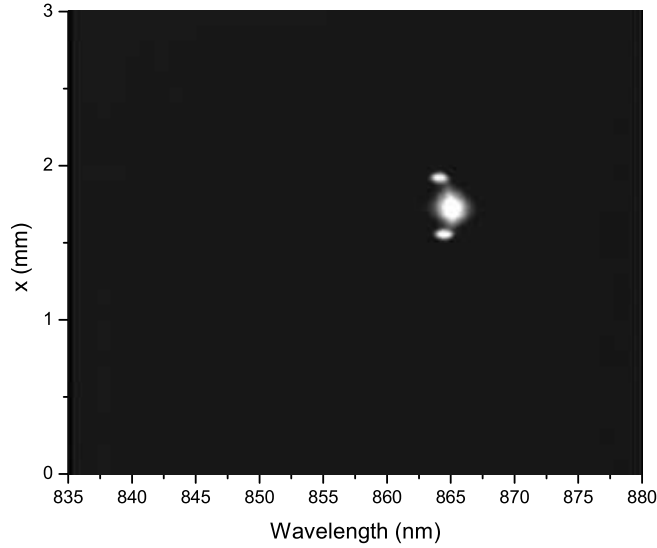
Figure 4.1: Spectral image of the indirect luminescence for 2 mW power.

of a ring around the central spot. There are several interesting features. First, the region between the central spot and the ring is completely dark. Second, the ring is very narrow spectrally and sharp and very narrow spatially—narrower than the excitation laser spot. In fact, it is spectrally narrower than the central spot. Third, the ring luminescence is slightly blue shifted with respect to the central luminescence. One can also notice the irregular (not completely circular) shape of the ring which we attribute to the asymmetry of the applied voltage. The ring followed the central spot when it was moved around the sample surface.

We should mention that a nearly identical effect was observed independently by Butov *et al.* in GaAs quantum wells [39] (Figure 4.3). Their sample was a n^+-i-n^+ structure consting of double 80 Å GaAs quantum wells separated by a 40 Å $Al_{0.33}Ga_{0.67}As$ barrier. It was excited by a red HeNe laser with λ=632 nm, and a voltage of 1.22 V was applied across the sample. They observed the appearance of a ring structure around the excitation spot at high laser powers (around 100 μW). The interesting thing was a claim of the existence of a second ring just at the edge of the excitation spot. The outside ring was as wide as 170 μm
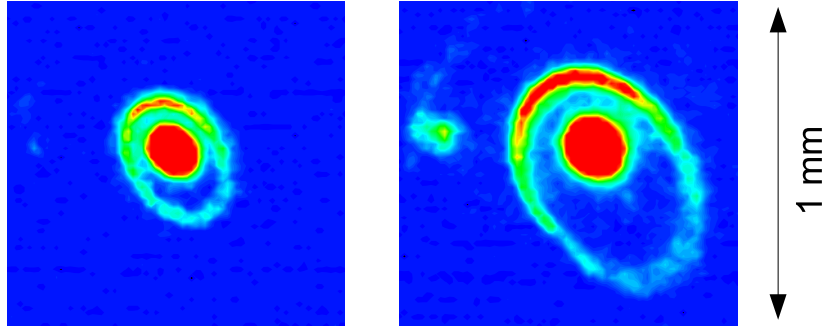
Figure 4.2: Two false color images of the ring projected directly on the CCD camera. T=2 K.

at 770 μW laser power. We could not verify the existence of a second ring in our samples.

There are two other interesting features of Butov's result. The first is the breaking of the outside ring into a periodic structure of bright spots. This periodic structure followed the ring when the excitation spot was moved and when the ring radius was varied by changing the excitation power. The spot structure was observed at temperatures as low as 0.5 K and disappeared when the temperature was increased to 4 K. Again, as with the inner ring, we could not reproduce this effect with our sample. This could be due to the low temperature required to observe it (Butov reports temperatures below 1.8 K). We can achieve it but there may be an issue of thermal equilibration of the carriers. It could be also due to the lack of enough spatial resolution to discern such fine features.

The second feature is the presence of bright spots in the region between the central spot and the ring and only there. Butov called them localized bright spots since they did not follow the excitation spot movement and preserved their position on the sample. We did not observe this effect either.
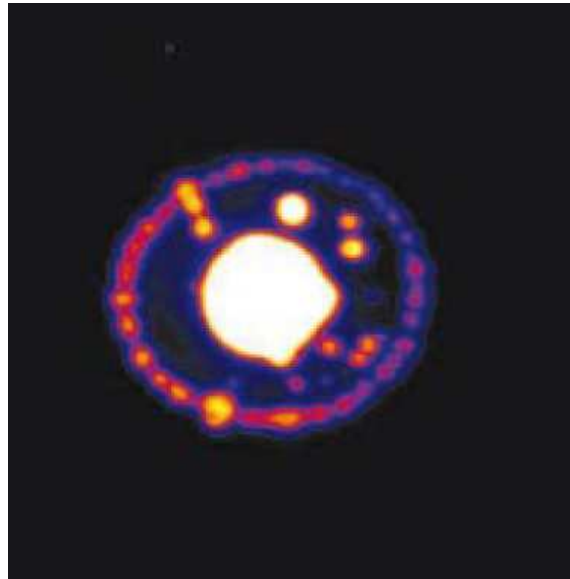
Figure 4.3: Ring pattern observed by Butov *et al.* Note the fragmentation of the ring into bright spots and the presence of local bright spots between the central spot and the ring. From Ref [39]
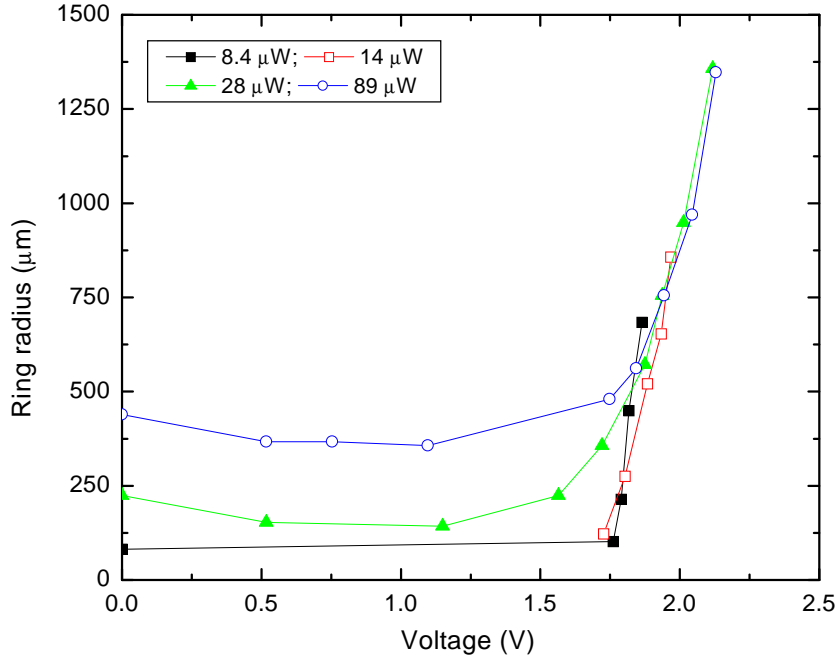
Figure 4.4: The size of the ring at different applied voltages and laser powers.

4.1 RADIUS VS. VOLTAGE AND LASER POWER

The first observation was that the ring radius could be manipulated by changing the voltage applied to the sample. Initial measurements showed that the ring radius decreased with increasing voltage—it entered the field of view from the outside at around 2 V and merged with the indirect exciton spot at around 2.5 V. At all times the ring luminescence followed the indirect luminescence spectrally, but it was at about 1 meV higher energy. This slight blue shift can be noticed in Figure 4.1. A more detailed investigation, however, showed that the ring structure actually exhibited a dependence opposite to the initial observation. At certain laser power lower than the one used initially, increasing the voltage from 0 V produced a faint ring around the indirect exciton luminescence that increased its radius from 0 (the ring emerged from the central spot) to a size beyond the field of view.

The dependence of the ring size on voltage is also related to the power of the excitation laser. We noticed that at higher power a lower voltage was required to create a ring with the same radius. This means that at higher power the creation of the ring is more efficient.

58

We took a series of curves for different voltages and different powers. The resulting graph is shown in Figure 4.4. It shows the radius of the ring as a function of voltage for several different powers. It can be noticed that the ring size increases both with increasing voltage at fixed power and increasing power at fixed voltage. The figure also shows that at fixed power the ring has a minimum size, which could be hundreds of microns. Although the ring size depends on the laser power, it is most sensitive to the applied voltage, especially in the range above 1.5 V. A plot of the ring radius as a function of the applied voltage at 160 μW laser power is shown in Figure 4.5. Between 3 and 4 volts the ring radius rapidly increases and at around 4 V is larger than the field of view. Increasing the voltage further brings the ring back into view and the radius decreases. This is the effect as initially observed.

During the course of these studies it was found that it wasn't necessary to apply voltage across the sample in order to observe the ring, as seen in Figure 4.4. However, the voltage makes the creation of the ring more efficient. This is evident form Figure 4.6. The graph shows the ring radius versus the laser power for four different voltage biases. The excitation was with a pulsed red laser with wavelength 612.7 nm and the sample was at 2 K. The ring can be created even at 0 V but it requires more power. The efficiency of the process is increased more than twice by just applying 1 V across the sample—just half of the power at 0 V is required to create a ring with the same radius at 1 V. Figure 4.6 also shows the rather linear dependence of the ring radius on the laser power with a slope increasing with voltage, which is an indication of the increasing efficiency of the ring creation process.

4.2   LIFETIME AND TRANSPORT

Observing such an unusual phenomenon one is inevitably tempted to think of it as somehow related to superfluidity of excitons. So a logical next step is to measure the transport of excitons from the center to the ring. In order to reach such distances of hundreds of microns they should have long enough lifetime and we should be able to observe their outward motion.

We performed a time resolved measurement of the ring structure using a modelocked pulsed red laser with a pulse duration of 50 ps. A time resolved profile is shown in Figure
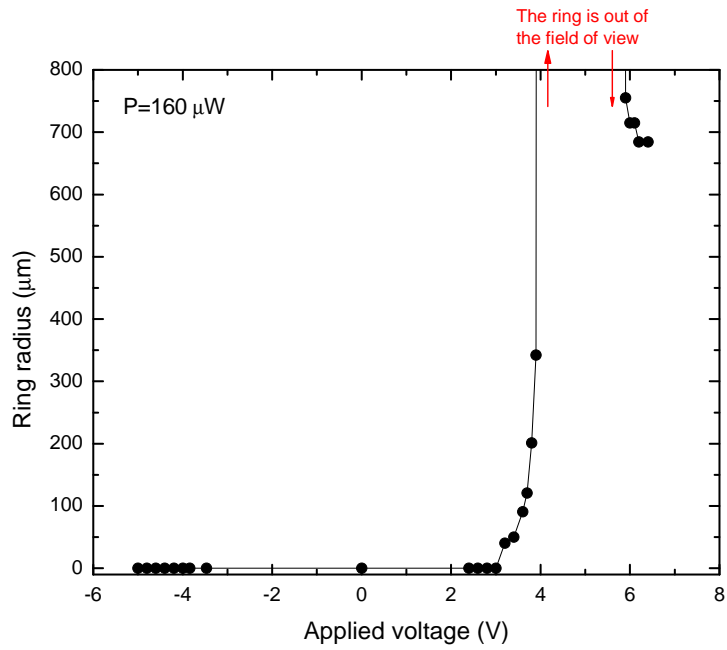
Figure 4.5: Radius of the ring vs. the applied voltage at 160 μW laser power.
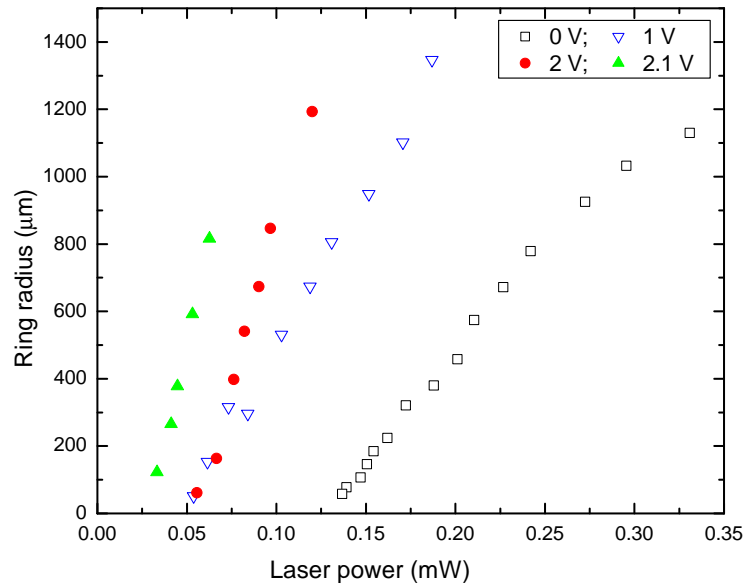

Figure 4.6: Radius of the ring vs. laser power for four different applied voltages.

60

4.7. The repetition rate of the pulses was 76 MHz (period 13 ns). The ring is 400 μm away from the central spot. The central spot is at angle of the glass block at 0 degrees (straight through) while the ring is projected on the spectrometer slit at an angle of -5 degrees. The data show that the indirect exciton dies quickly with a lifetime of the order of 3 ns, while the ring luminescence persists for a very long time—more than 13 ns, the period between the laser pulses. Another measurement with lower repetition rate of the laser allowed us to observe lifetimes of the ring in excess of 200 ns—Figure 4.8. The period of the laser was 260 ns and the ring was 500 μm away from the central spot. The intense peak at $t = 0$ we attribute to overlap of the ring luminescence with the central spot. At long times the luminescence reaches a saturation level and the counts just before the laser pulse are the intensity from the previous pulse 260 ns before.

If excitons were moving from the center outward, their transport would show up as luminescence that shifts with time from the central spot to the ring. A typical phonon speed in GaAs is on the order of 10^5 cm/s [61]. With that speed it will take 400 ns for the excitons to travel a distance of 400 μm. Such an effect is not observed in Figure 4.7. Transport wasn't present even with applied stress where we were exciting the sample on the side of the stress well and were trying to observe luminescence in the bottom of the well. The lack of transport is mainly due to the very short lifetime of the exciton species at the central spot. Nevertheless, something must be moving from the center to the ring since our excitation is confined to the central region. With such a long lifetime it appears to be some kind of a steady state process.

4.3 HIGH TEMPERATURE MEASUREMENTS

We also performed measurements at high temperature, which provided us with information about the temperature limits of the ring effect. The ring persisted up to 110 K at which point it became extremely blurry and disappeared. A CCD image of the luminescence at 90 K is shown in Figure 4.9. The sample was excited by a HeNe CW laser ($\lambda = 632.8nm$) with average power 2.5 mW and spot size of 60 μm. The applied voltage was 5.84 V and
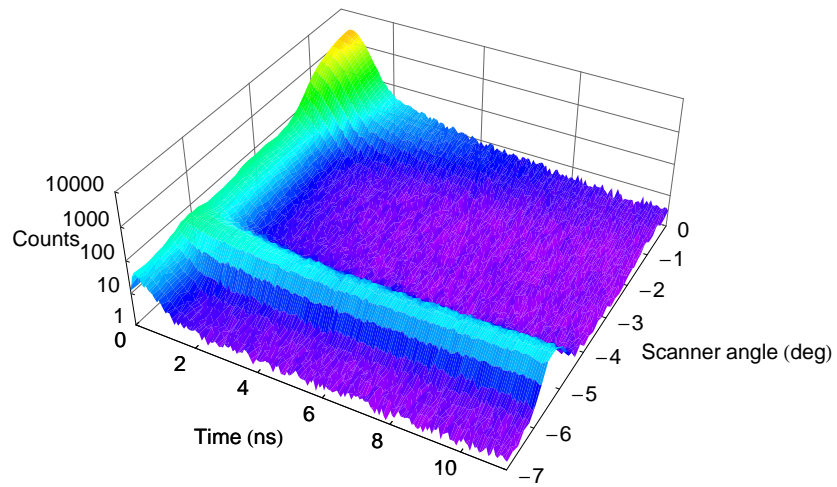
Figure 4.7: Time-resolved profile of the ring luminescence on a logarithmic scale. The central spot is at 0 degrees and the ring is at -5 degrees.
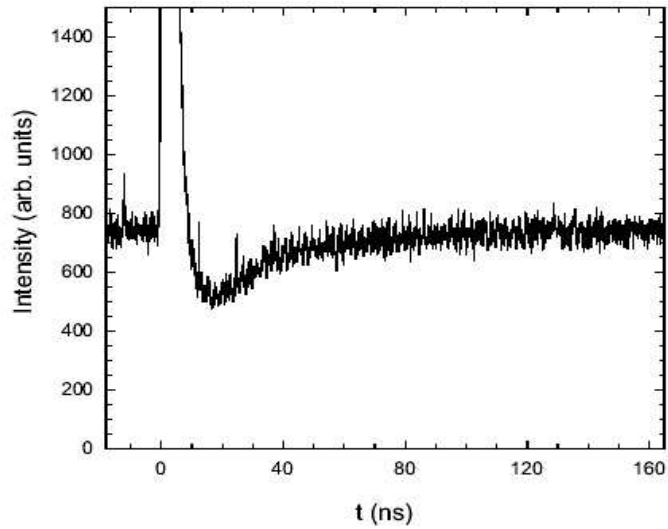
Figure 4.8: Time trace of the ring with 500 μm radius at T = 2 K.
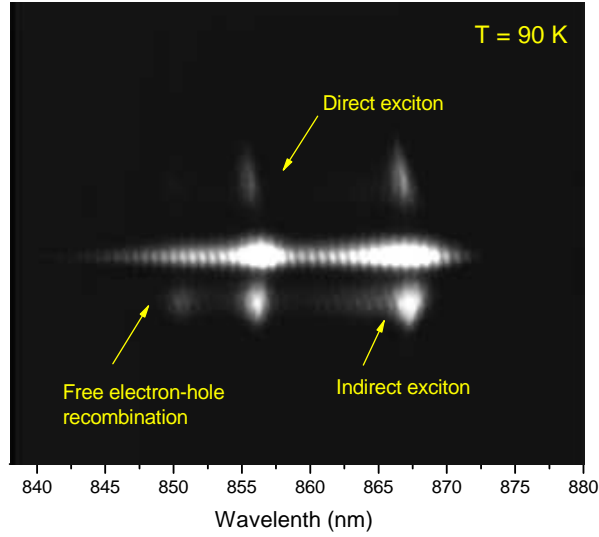
Figure 4.9: CCD image of the luminescence at 90 K. Ring is observed for the direct and indirect exciton species as well as for the free electron-hole recombination.

the current through the sample was 30 μA. The most prominent feature of the luminescence at high temperature is the appearance of the ring structure not only for the indirect exciton for which it was observed initially but also for the direct exciton and the free electron-hole recombination. The latter are thermally excited at this temperatures since the exciton binding energy is of the order of 10 meV which corresponds to a temperature of 116 K. The fact that the ring appears also for non-excitonic species suggests that probably this effect is not entirely related to excitons.

The high temperature results show another difference with the ring effect as observed by Butov. Their ring structure disappears at around 10 K while ours persists to temperatures ten times as high. The reason for this difference is probably due to the difference in the quantum well structures or even the quality of the samples.

4.4   OTHER SAMPLES

We used several other samples to explore the ring effect. First, we studied the undoped $In_{0.1}Ga_{0.9}As$ sample with the same 60-40-60 geometry (again, 60-40-60 refers to the thicknesses of the quantum wells and the barrier between them). We couldn't reproduce the results at any power and voltage. This suggests that the ring effect is related to the n-i-n doping, *i.e.* tunneling current through the barriers.

Another sample we used was an identical $In_{0.1}Ga_{0.9}As$ structure but with p-i-n doping of the substrate and the capping layer. There wasn't a ring at any positive voltage bias and any power.

Probably the most surprising result was when a ring was observed with a single 60 Å $In_{0.1}Ga_{0.9}As$ quantum well sample with similar GaAs and $Al_{0.32}Ga_{0.68}As$ barriers. In a single QW, the applied voltage is irrelevant to the exciton lifetime since there is no Stark shift and hence no indirect species. The dependence of the lifetime in the single and double quantum well samples is shown in Figure 4.10. The excitons in single quantum well have short lifetime practically independent on the applied voltage, whereas the double quantum well sample exhibits a noticeable increase of the lifetime with the applied voltage. Theoretical calculations show a similar result. The inset in Figure 2.6 shows an exponential decrease of the oscillator strength which is inversely proportional to the exciton lifetime.

Since in the single quantum well we cannot create indirect excitons whose density could be controlled by changing the applied voltage, the required power to create a ring in this sample was higher than in the case with the double quantum well.

Another sample that we studied was a 60-40-60 $In_{0.1}Ga_{0.9}As$ double quantum well structure with 44% Al in the outside barriers. The ring was also observed in this structure. Using a sample with identical geometry to the one used by Butov we were able to reproduce his result but without the ring fragmentation. We tried both single and double quantum well samples and in both a ring was observed.
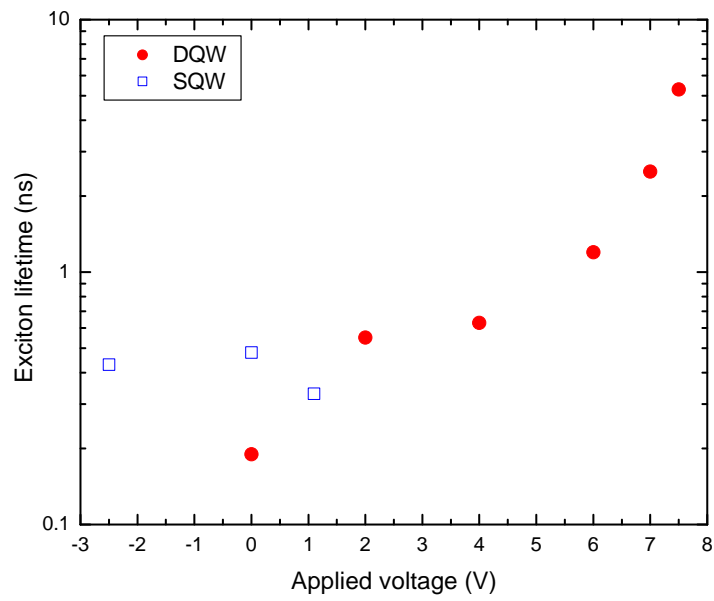
Figure 4.10: Lifetime of the excitons measured in single (open squares) and double (filled circles) quantum well samples vs. applied voltage.

5.0 AN EXPLANATION OF THE RING EFFECT

After giving the description of the ring phenomenon in the previous chapter we will now attempt to present an explanation of this unusual effect. Several different explanations were proposed to explain the ring. Among them are a simple optical effect where the ring is due to photons propagating in the medium with reabsorption and secondary emission of photons. Another explanation is a shock wave that piles up excitons at a certain distance from the central spot. A third explanation is an actual superfluid state of excitons. We will consider and discuss each one of these.

The first possible explanation that comes to mind is an optical effect of some sort. While it is not clear how changing the applied voltage across the sample can affect photons travelling through the sample (if indeed this is an optical effect), we performed an experiment to rule this option out. We produced the "collision" of two rings created by two separate laser beams. We used a 50/50 beamsplitter to split the input laser beam into two beams with approximately equal intensities. The experimental setup is shown in Figure 5.1. The distance between the two spots on the sample can be controlled by slightly offsetting one of the mirrors M1 and M2. The beams are then focused on the sample by a single lens.

The results of this experiment are shown in Figure 5.2. When the spots from the two beams are near each other, the rings don't overlap or collide with a bright region between them, but instead merge in a single ring. This argues against a simple optical effect where the rings would be expected to pass through each other and overlap (very much like Olympic circles).

This result also rules out a shock wave as an explanation of the ring. If shock waves were travelling through the sample they would collide in the middle between the spots and form a bright region instead of a dark one as observed. We can also exclude ballistically moving
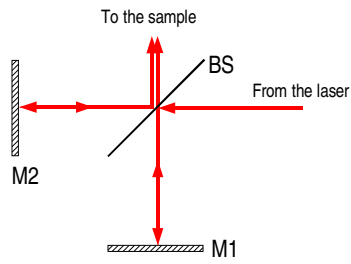
66

To the sample

BS

From the laser

M2

M1

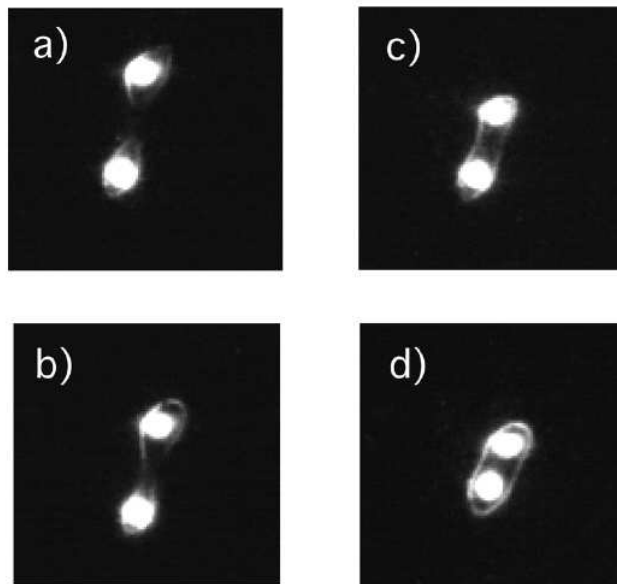Figure 5.1: Splitting of the input beam in two

a)

b)

c)

d)

Figure 5.2: Still images from the two beam experiments. From (a) to (d) the two spots are approaching each other

excitons, since they will either pass through each other leading to overlapping rings or, if the interaction between them is strong enough, will collide as in the case of shock waves and will form a bright middle region.

Looking at the behavior of the two rings one might speculate that the result looks very much like two droplets of liquid merging into one.

An explanation given by Butov [39] involves excitons travelling the macroscopic distance between the central spot and the ring. He suggested that at higher densities the long lifetime of the indirect excitons permits them to travel large distances and move away from the central spot. Only excitons with small wave vector k located in the so called radiative zone determined by the intersection of the photon dispersion cone and the exciton dispersion curve will be able to emit light, Figure 5.3. The gradient of the exciton density will produce drift and diffusion of excitons away from the central spot. Also, due to their repulsive interaction, the same gradient will result in a pressure pushing the excitons outward. Butov's explanation of the dark region between the central spot and the ring involves the inability of the excitons to emit light while not in the radiative zone. Due to the density gradient the excitons will move outward from the central spot down the potential energy hill and thus will have large k. Far from the excitation spot the energy gradient disappears and the excitons relax to the low energy states and enter the radiative zone.

However, as we have pointed out, the two beam experiment argues against ballistic exciton propagation over macroscopic distances. Butov argued that there is a long-range attraction, but this is unlikely over distances of 100 μm.

Our time-resolved measurements show that the effect is not due to reabsorption and secondary emission of photons. If that were the case the ring luminescence would have been present only during the laser pulse. The data, on the other hand, show that the ring and the central spot luminescence have different time characteristics. The one from the center lasts a very short time—a few nanoseconds, while the one from the ring persists for hundreds of nanoseconds. This fact suggests that the ring luminescence and the central spot luminescence originate from different species—the central spot from "normal" excitons and the ring from some sort of quasi-stable state with very long lifetime.

One suggested explanation is superfluidity of excitons. One can imagine a superfluid that
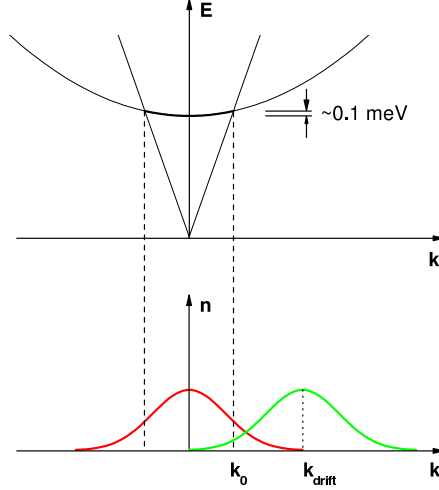
Figure 5.3: Energy diagram of the exciton and photon dispersion and momentum distributions of excitons without (red) and with (green) drift velocities. After Ref. [39].

prevents excitons from emitting light as it prevents phonon emission. The observation of pattern formation and its macroscopic nature, as well as the appearance of bright spots along the ring, prompted Butov to suggest that the ring could be a superfluid state of excitons, drawing a parallel with the vortices of the atomic Bose condensates [39]. In the following we examine arguments for and against the idea of superfluid.

As discussed earlier, in two dimensions Bose-Einstein condensation cannot occur, but a transition to a superfluid state nevertheless can take place—a Kosterlitz-Thouless transition. In the dilute Bose gas limit the critical density for the transition is given by [30]

$$k_B T_c \approx \frac{4\pi\hbar^2 n}{2m \ln\ln(1/\gamma)} \tag{5.1}$$

where

$$\gamma = na^2 \tag{5.2}$$

where a is the range of the interaction, which can be approximated by the Bohr radius of the excitons, m is the mass of the particle, and n is the 2D density of the particles. The factor $1/\ln\ln(1/na^2)$ varies between 0.34 and 0.65 for na^2 in the range $10^{-8} < na^2 < 10^{-2}$ so we

can approximate $n/\ln\ln(1/na^2)$ by n/2 and solve (5.1) for n. When the spin degeneracy is taken into account we have:

$$n_c = \frac{0.32 g m k_B T}{\hbar^2} \tag{5.3}$$

The temperature dependence is the same as in the original Kosterlitz-Thouless prediction (1.11). If we take into account the disorder in the system, the relation becomes much more complex as shown by Berman [41], Equation (1.13). Figure 5.4 shows a plot of the temperature of the Kosterlitz-Thouless transition as a function of the exciton density for several different magnitudes of the disorder. From the figure for temperature of 2 K and disorder Q of 0.4 meV, an estimate from the inhomogeneous broadening of our samples, we find a critical density of $\sim 7 \times 10^{10}$ cm^{-2} (see Eq. (1.13)). In comparison, the critical exciton density deduced from Equation (5.3) for a temperature of 2 K is 7.2×10^{10} cm^{-2} using an exciton mass of 0.25 m_0 [62] and a spin degeneracy of 4.

In practice, however, it is usually much easier to control the exciton density than the temperature. The density of the excitons can be changed by changing the excitation laser power. Then according to the theory there should be a power at which a ring should not appear. Indeed, we observed such behavior. Figure 5.5 shows the ring radius vs. power at applied voltage of 1 V. It can be seen that at powers less than 0.05 mW there is no ring. With a laser spot of approximately 70 μm in diameter and 76 MHz repetition rate of the pulsed laser this corresponds to a power density of 1.7×10^{-8} W/cm^2 per pulse, which for wavelength of 612 nm—the excitation wavelength used—translates to 5.27×10^{10} photons/cm^2 per pulse. From the absorption of GaAs and the relative intensity of the luminescence from the quantum wells and the bulk GaAs we estimate that approximately 30% of the input photons excite excitons in the quantum well region. This gives an exciton density of 1.57×10^{10} cm^{-2}, which is in the range of the Kosterlitz-Thouless transition calculated both with and without disorder.

This result seems to support the idea that the ring arises from a Kosterlitz-Thouless superfluid transition. On the other hand, several other results are inconsistent with such an explanation.

One basic test for superfluidity is the temperature dependence of the critical density.
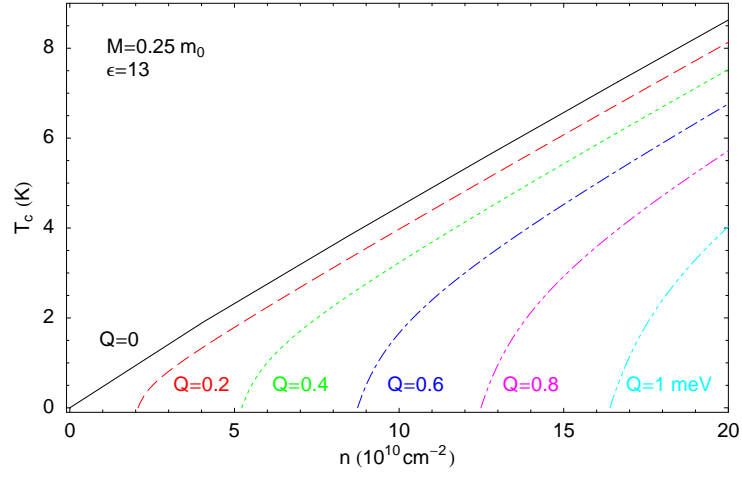
Figure 5.4: Dependence of the Kosterlitz-Thouless transition temperature on the 2D exciton density for various degrees of disorder. After Ref. [41]
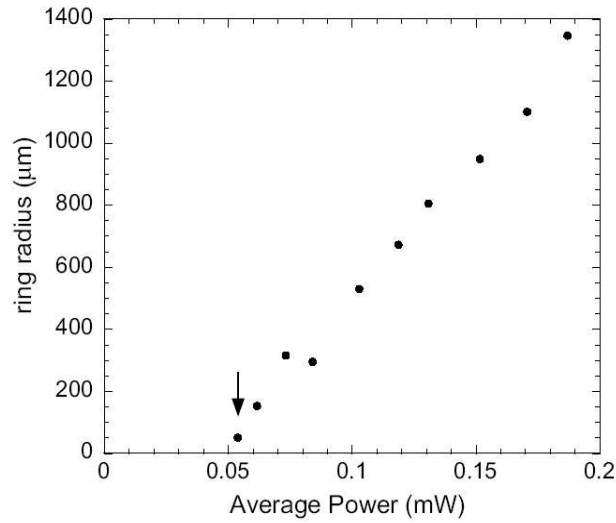

Figure 5.5: Ring radius vs. average excitation power. T = 2 K, modelocked laser, $\lambda = 612$ nm, rep. rate 76 MHz, spot size 70 μm.

71
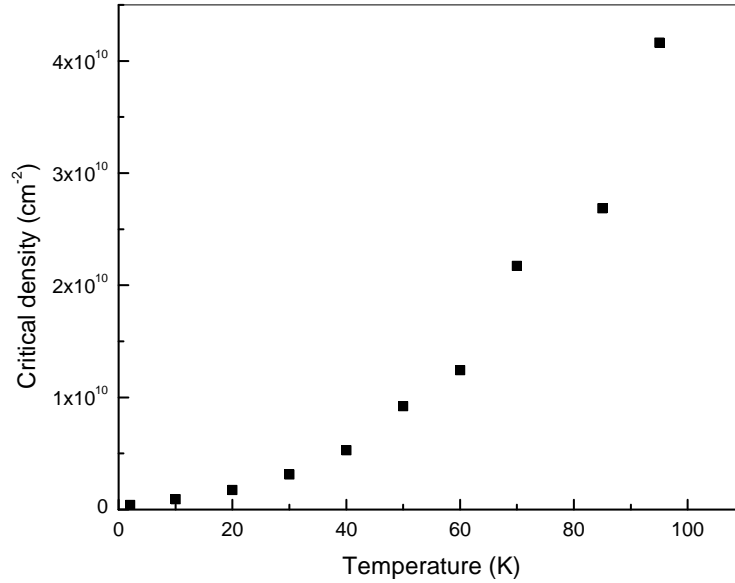
Figure 5.6: Critical density for appearance of the ring vs. temperature

The simple relations from Equation (1.11) and (5.3) show that we should expect a linear dependence. We measured the minimum power needed to create a ring (*i.e.* ring with radius almost 0) at various temperatures and from that we calculated the critical exciton density. The result is shown in Figure 5.6. It displays a different temperature dependence than Equation (1.11)—it is superlinear, close to quadratic, instead of linear. This seems to suggest an argument against superfluidity. On the other hand, for a two-dimensional system in a potential trap the critical density could depend on the square of the temperature [63]. Is it possible for the excitons to be trapped? Initially, Butov suggested that their observed localized bright spots (Figure 4.3) are due to trapping of indirect excitons in potential traps formed by in-plane potential fluctuations. One could also speculate that the superlinear dependence is due to exciton ionization at higher temperatures, which will make their creation less efficient and hence the need for higher laser powers to achieve the required critical density.

Another experiment, however, is even more inconsistent with the superfluid transition
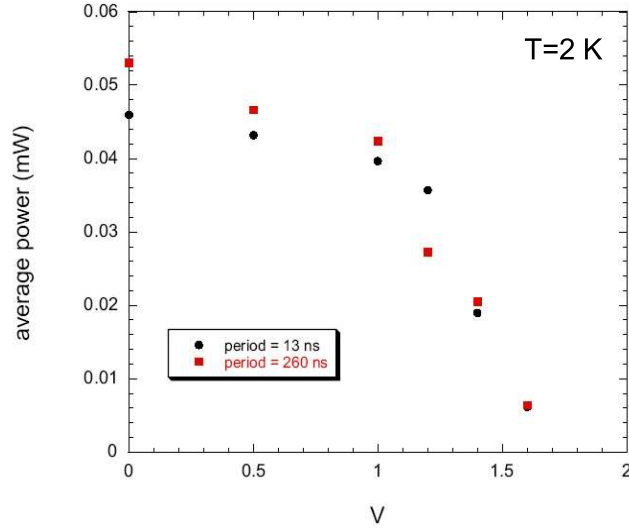
Figure 5.7: Average critical power needed to create the ring vs. applied voltage across the sample for two different excitation regimes: black dots–pulsed laser with 13 ns period; red circles–pulsed laser with 260 ns period.

idea. Figure 5.7 shows the average critical power vs. the applied voltage for two different excitation regimes. One is with a pulsed laser with period between the laser pulses of 13 ns and the other with period of 260 ns. The two sets of average powers have strikingly close values. This means that the instantaneous power is not that important for the creation of the ring but rather the average power is the one that matters—the instantaneous power (or the energy per pulse) of the 13 ns period pulses is 20 times lower than the 260 ns period pulses and yet the average critical power is the same. On the other hand the indirect exciton lifetime is of the order of 5 ns, which is much shorter than the period between the laser pulses. This means that the ring effect does not depend on the instantaneous population of the indirect excitons but on the population of another state which has an intrinsically long lifetime. A Kosterlitz-Thouless superfluid transition, on the other hand, would depend on the exciton population in one laser pulse.

An important step in the understanding of this unusual ring effect was the dependence of the critical density on the excitation wavelength. We used a dye laser which allowed us

to tune the wavelength and changing the laser dye provided a broad range of wavelengths. For each wavelength the minimum excitation power required to create a ring was measured. The results are shown in Figure 5.8. The top axis shows the energy of the photons for the corresponding wavelength. The lack of data points above 660 nm is not due to the lack of data but due to the fact that the ring wasn't observed for wavelengths above 660 nm. In fact, the power was increased up to 1000 times the usual values—up to a few milliwatts— without success in reproducing the ring. With increasing the photon energy from 1.9 eV (or decreasing the photon wavelength from 660 nm) one observes a sudden jump of the critical power at around 630 nm after which it stays almost constant to at least 532 nm, the shortest measured wavelength. One could argue that the change of efficiency of the ring creation is due to different absorption in the barriers at different wavelengths. But the difference should not be so drastic. The total width of the quantum well region is 260 Å and the $Al_{0.3}Ga_{0.7}As$ barriers are 1300 Å thick or 5 times thicker. This would mean that a laser with energy slightly higher than the barrier band gap will create excitons in the quantum well region with density comparable to the density created by a laser with energy lower than the barrier band gap but with five times lower power. We, however, used laser powers in a range of three orders of magnitude with no success. The red and the green lines in Figure 5.8 correspond to the energies associated with the indirect and direct transitions shown on the band diagram on the right. The 660 nm corresponds to indirect transition of 1.88 eV between the valence band of GaAs and the Γ valley of $Al_{0.3}Ga_{0.7}As$, and 630 nm corresponds to the direct transition of 1.98 eV in the $Al_{0.3}Ga_{0.7}As$ barriers. This kind of relation suggests strongly that the ring effect is related to hot carriers, created by high energy photons jumping over the barriers.

To confirm that the barrier height was important, similar experiments were performed with samples with slightly different structure. A sample with identical thicknesses of the various layers (60-40-60 structure) but with 44% Al in the barrier alloy was grown and studied as well as a sample identical to Butov's [39] (*i.e.* 80-40-80 structure of GaAs wells and $Al_{0.33}Ga_{0.67}As$ barriers).

The results are shown in Figure 5.9. Indeed, we see a similar cutoff and jump of efficiency at energies consistent with the indirect GaAs–$Al_{0.33}Ga_{0.67}As$ and the direct within the

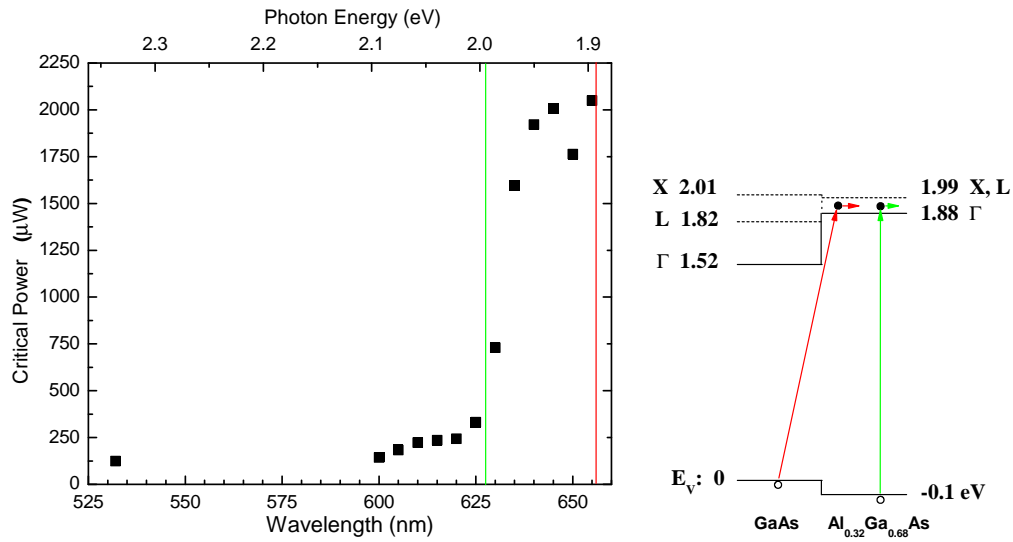Figure 5.8: Critical power for the creation of the ring as a function of the excitation wavelength and an energy band diagram of the possible processes.
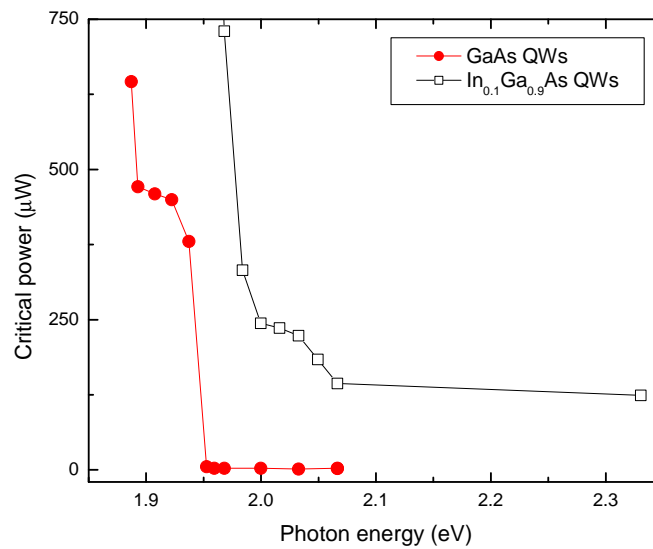

Figure 5.9: Wavelength dependence of the critical power for two different samples: filled red circles, 80-40-80 GaAs/AlGaAs structure with $Al_{0.33}Ga_{0.67}As$ outer barriers; open squares, 60-40-60 $In_{0.1}Ga_{0.9}As$/GaAs structure with $Al_{0.32}Ga_{0.68}As$ outer barriers

$Al_{0.33}Ga_{0.67}As$ transitions. The ring was not observed in the high barrier sample for wavelengths longer than 591 nm, which is equivalent to 2.1 eV photon energy which is consistant with the $Al_{0.44}Ga_{0.56}As$ band gap of 2.16 eV. This leads us to believe that the jumping of carriers over the AlGaAs barriers plays an important role in the ring effect. The inability to reproduce a ring in the undoped sample also suggests that the presence of free carriers in the well region is crucial for the ring. Since the $In_{0.1}Ga_{0.9}As$ has a conduction band lower than the one of GaAs, the well region of the doped samples will be populated with electrons with concentration of a few times 10^{10} cm^{-2} due to tunneling from the outer n-doped layers. The observation of the ring in the single quantum well sample shows that the indirect exciton is not a factor in the process since there are no indirect exciton species in a single quantum well structure.

After examining all the evidence we proposed the following explanation [64]. Apparently the ring effect is not entirely related to excitons. Due to modulation doping the quantum well region will be populated with electrons. When hot carriers are created by above-the-gap excitation, they will have several options under applied voltage. First, they can cool down and fall into the well region and get trapped there. They can also drift to the contacts under the applied voltage. The carriers in the wells can leak slowly through the barriers to the contacts and contribute to the measured current. Of course, the carriers trapped in the wells are free to diffuse within the plane of the quantum wells. A diagram of the processes is shown in Figure 5.10.

Due to their higher mass and slower drift velocity the holes will get trapped in the well region faster than the electrons. As a result there will be more cold holes than electrons near the excitation spot. Holes will recombine with the cold electrons trapped in the QW region, in such a way depleting it. Under the proper conditions with appropriate electron-hole generation rate, the entire region around the laser spot will be devoid of electrons and filled entirely with holes. This will result in a "puddle" of holes around the laser spot surrounded by a "sea" of electrons. Due to diffusion the holes will want to move outward, away from the excitation spot whereas the electrons will move inward, toward the excitation spot. As a result, at the border of the hole puddle, electrons will recombine with the holes and luminescence in the form of a sharp ring will be observed. Figure 5.11 shows schematically
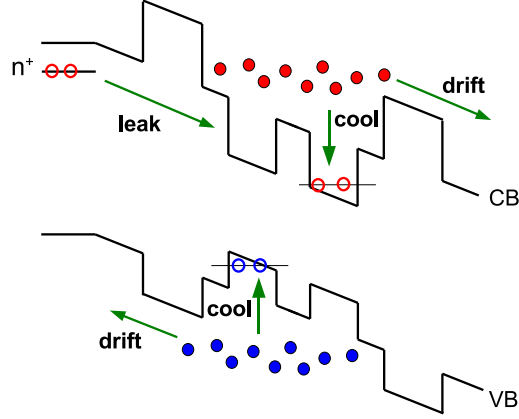
Figure 5.10: Proposed processes occurring in the coupled quantum wells sample upon light excitation

the process in the plane of the quantum wells. The size of the ring will be determined by the size of the hole puddle which is determined by the rate of hole generation and electron depletion in the central region. This rate ultimately will depend on the excitation power.

The time-resolved measurement from Figure 4.8 shows the luminescence of the ring that is 500 μm away from the central spot. We observe a dip just after the laser pulse and after that the count rate recovers to its value at long times. This dip can be understood now as a propagation of the laser disturbance through the hole puddle. From the distance, 500 μm, and the time it takes the ring to recover to its steady state we can calculate the speed, with which the disturbance travels: $\sim 5 \times 10^6$ cm/s. In contrast, the acoustic phonons have speeds limited to 5×10^5 cm/s.

The idea of a puddle of holes is supported also by the results from the two beam experiment. The rings didn't collide but merged in one without sharp boundary just as two puddles of liquid.

We also performed several sets of measurements under different conditions. Some of them can be explained by the proposed model.

The first one is the effect of a magnetic field on the ring properties. The results are shown in Figure 5.12. It shows the dependence of the ring radius on the applied perpendicular
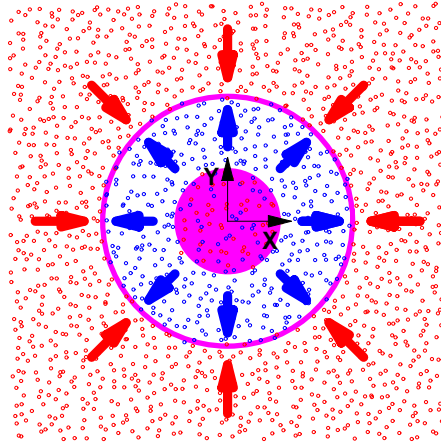
Figure 5.11: The in-plane distribution of electrons (red circles) and holes (blue circles). The laser excites the sample at the center (purple circle) and the ring is formed at the boundary between the holes and the electrons.

magnetic field, using the setup described in Chapter 3, for two different voltage biases across the sample. It is not immediately obvious how the magnetic field will influence the ring since it doesn't create indirect excitons or change the exciton density as the electric field does. Nevertheless, the dependence is similar to the external electric field, namely the size of the ring increases with increasing magnetic field. The interesting feature is the presence of a plateau at around 0.3 T which wasn't observed with electric field only.

This effect can be understood in the framework of the hole puddle model by assuming that the magnetic field changes the electron and hole diffusion coefficients in different manners. If the hole diffusion increases faster with magnetic field, the holes will travel farther and the ring will increase its radius, exactly as it is observed in the experiment. Another possible explanation is the magnetoresistance change as described in Chapter 3. With increase of the magnetic field the magnetoresistance of the quantum wells will increase which will lead to an increased voltage drop across the quantum wells and higher electric field. The ring radius is proportional to the applied voltage and is expected to increase as indeed is observed.

Another set of experiments which is somewhat explainable, although not completely, by
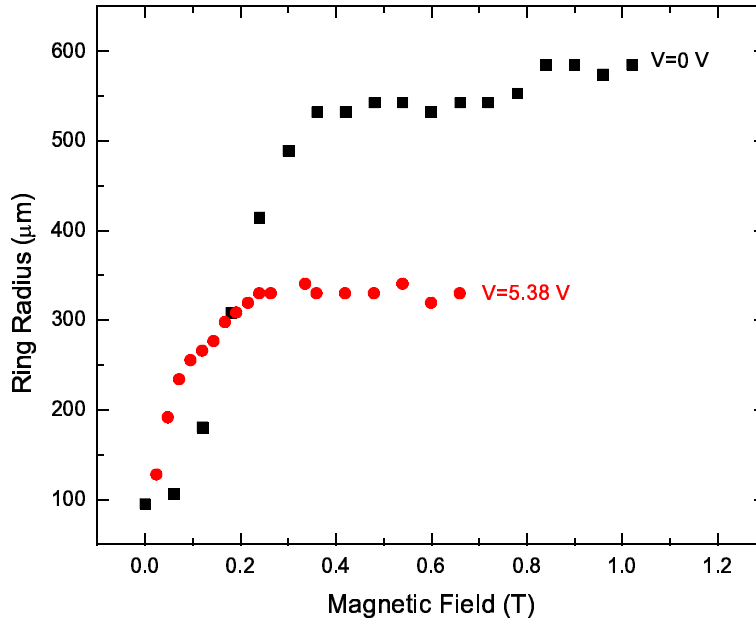
Figure 5.12: Radius of the ring vs. applied magnetic field for two voltage biases

the model is the influence of stress on the ring. The way the stress was applied is described in Chapter 1. The best way to observe the effect of stress on the ring was to project the luminescence on the CCD camera through a long pass filter and polarizer in order to reduce the reflected laser light as much as possible. The image of the ring in the vicinity of maximum stress is shown in Figure 5.13. The ring is attracted by the stress and at the point of contact with the stressor pin where the stress is highest it exhibits very sharp curvature. When the excitation spot was moved around the ring followed it but it was strongly attracted and distorted by the high stress point. A sequence of images of the central spot moving through the point of highest stress is shown in Figure 5.14. On these images the point of maximum stress is manifested by the dark region with two bright fragments of the ring on its sides.

The sharp ring features in the stress results can be understood as sinkage of the electrons and the holes toward the point of maximum stress and minimum energy. The dark region which we sometimes observe at that point can be explained as filling of the available radiative states.

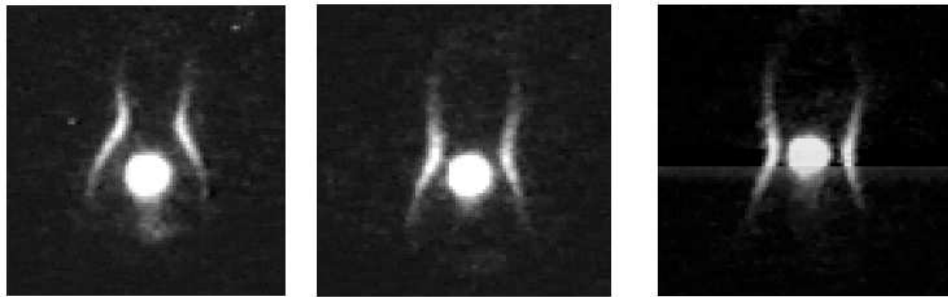Figure 5.13: Image of the ring with applied stress to the sample.

Figure 5.14: Sequence of images of the laser spot passing through the point of highest stress.

6.0 MODELLING OF THE RING

6.1 SIMPLE MODEL WITHOUT COULOMB INTERACTION

A theoretical model which describes the electron-hole dynamics was proposed by D. Snoke and later refined in collaboration with S. Simon at Bell Labs [65]. A similar model was simultaneously proposed by Butov *et al.* [40, 66]. It models the processes taking place in the quantum well structure upon excitation depicted in Figure 5.10. It does not, however, take into account the Coulomb interaction between the charged particles. A model including such an interaction will be discussed in the next section. In this simple model the laser creates hot electrons and holes that can either drift over the barriers to the contacts or cool down and get trapped in the wells. Cold carriers also can tunnel through the barriers to the contacts. We also allow for diffusion in the plane of the quantum wells. These processes can be described by the following diffusion equations introducing the electron-hole recombination as nonlinear terms:

$$\frac{\partial n_{hot}(\mathbf{r})}{\partial t} = D_{hot}^e \nabla^2 n_{hot}(\mathbf{r}) - \frac{n_{hot}(\mathbf{r})}{\tau_{cool}^e} - \frac{n_{hot}(\mathbf{r})}{\tau_{drift}^e} + G(\mathbf{r}) \tag{6.1}$$

$$\frac{\partial p_{hot}(\mathbf{r})}{\partial t} = D_{hot}^h \nabla^2 p_{hot}(\mathbf{r}) - \frac{p_{hot}(\mathbf{r})}{\tau_{cool}^h} - \frac{p_{hot(\mathbf{r})}}{\tau_{drift}^h} + G(\mathbf{r}) \tag{6.2}$$

$$\frac{\partial n_{cold}(\mathbf{r})}{\partial t} = D_{cold}^e \nabla^2 n_{cold}(\mathbf{r}) + \frac{n_{hot}(\mathbf{r})}{\tau_{cool}^e} - \frac{n_{cold}(\mathbf{r}) - n_{eq}}{\tau_{leak}^e} - \xi n_{cold}(\mathbf{r}) p_{cold}(\mathbf{r}) \tag{6.3}$$

$$\frac{\partial p_{cold}(\mathbf{r})}{\partial t} = D_{cold}^h \nabla^2 p_{cold}(\mathbf{r}) + \frac{p_{hot}(\mathbf{r})}{\tau_{cool}^h} - \frac{p_{cold}(\mathbf{r})}{\tau_{leak}^h} - \xi n_{cold}(\mathbf{r}) p_{cold}(\mathbf{r}) \tag{6.4}$$

The problem is two dimensional and $\mathbf{r}$ represents the in-plane coordinate. Equations (6.1) and (6.2) describe the dynamics of the hot carriers created by the non-resonant laser.

$n_{hot}(\mathbf{r})$ and $p_{hot}(\mathbf{r})$ are the density distributions of the hot electrons and holes in the plane of the quantum wells. The first term on the right hand side describes the diffusion of hot carriers in the plane of the well, the second term describes the cooling of the particles with characteristic cooling times τ_{cool}^{e} and τ_{cool}^{h}. The third term is the drift of the particles over the quantum well barriers toward the contacts. This process is described by the drift times τ_{drift}^{e} and τ_{drift}^{h}. The last term is the carrier generation rate, $G(\mathbf{r}) = Af(\mathbf{r})$, where $f(\mathbf{r})$ is the normalized laser beam profile and A is the total flux of absorbed photons.

Equations (6.3) and (6.4) describe the dynamics of the cold particles with diffusion coefficients D_{cold}^{e} and D_{cold}^{h}. The second term on the right hand side describes the generation of cold carriers by cooling. The third term is the tunnelling through the barriers toward and from the contacts that tries to bring the electron-hole population to equilibrium with characteristic times τ_{leak}^{e} and τ_{leak}^{h}. The equilibrium electron distribution, n_{eq}, is determined by the modulation doping and is assumed to be constant; the equilibrium distribution for holes is assumed 0. The last term represents the recombination of cold electrons and holes and is the nonlinear term in the equations. ξ is the electron-hole capture coefficient. We also make the assumption that the electron and the hole form an exciton after they meet, since the luminescence from the ring appears to be excitonic. The recombination term is written as proportional to $n_{cold}p_{cold}$ which assumes that the electron and the hole recombine immediately after they find each other. The actual luminescence is also assumed to be proportional to $n_{cold}p_{cold}$.

Some simplifications to these equations can be made. First, the in-plane diffusion of hot carriers can be neglected compared to the drift and cooling rates—usually the carriers diffuse much slower than the cooling (scattering off phonons and other carriers) or the drifting (jumping over the barriers). In these circumstances the first two equations can be solved exactly for the steady state where $\partial n_{hot}/\partial t = 0$ and $\partial p_{hot}/\partial t = 0$:

$$\frac{n_{hot}}{\tau_{cool}^{e}} = C_{e}G(r) \tag{6.5}$$

$$\frac{p_{hot}}{\tau_{cool}^{h}} = C_{h}G(r) \tag{6.6}$$

where $C_{e(h)} = 1/(1 + \tau_{cool}^{e(h)}/\tau_{drift}^{e(h)})$ and basically represents the ratio of the carriers cooling into the wells to the carriers drifting over the barriers.

Then equations (6.3) and (6.4) become:

$$\frac{\partial n_{cold}(\mathbf{r})}{\partial t} = D^e_{cold}\nabla^2 n_{cold}(\mathbf{r}) + C_e G(\mathbf{r}) - \frac{n_{cold}(\mathbf{r}) - n_{eq}}{\tau^e_{leak}} - \xi n_{cold}(\mathbf{r})p_{cold}(\mathbf{r}) \qquad (6.7)$$

$$\frac{\partial p_{cold}(\mathbf{r})}{\partial t} = D^h_{cold}\nabla^2 p_{cold}(\mathbf{r}) + C_h G(\mathbf{r}) - \frac{p_{cold}(\mathbf{r})}{\tau^h_{leak}} - \xi n_{cold}(\mathbf{r})p_{cold}(\mathbf{r}) \qquad (6.8)$$

Since the system has azimuthal cylindrical symmetry, the problem can be reduced to one dimension and ∇^2 replaced by the radial second derivative in cylindrical coordinates, $\frac{1}{r}\frac{d}{dr}\left(r\frac{d}{dr}\right)$. These equations can be solved numerically by discretely propagating the time with a step Δt and at each time step calculating the changes Δn and Δp by evaluating the right hand side:

$$\Delta n = \Delta t\left(D_e(n'/r + n'') + C_e G(r) - \frac{n - n_{eq}}{\tau^e_{leak}} - \xi\, n\, p\right) \qquad (6.9)$$

$$\Delta p = \Delta t\left(D_h(p'/r + p'') + C_h G(r) - \frac{p}{\tau^h_{leak}} - \xi\, n\, p\right) \qquad (6.10)$$

where n' and p' are the numerical derivatives with respect to r. For the parameters we can either use standard values or estimate them from the experimental conditions. The initial conditions for the electron and the hole distributions are $n_0(r) = n_{eq}$ and $p_0(r) = 0$. The intensity of the laser is determined by the value of the total flux A (*i.e.* the total number of photons per unit time absorbed over the entire area of the laser spot), while the profile of the beam, $f(r)$, is usually assumed to be a Gaussian. We are interested in steady state solutions and the way to find them is to propagate Equations (6.9) and (6.10) until Δn and Δp are essentially zero.

A solution of the model for laser power of 94.2 μW at 632.8 nm, which corresponds to absorbed photon flux of 3×10^5 ns^{-1} over the entire laser spot, is shown in Figure 6.1. The laser is modelled as continuous wave, providing constant generation rate, with Gaussian profile with FWHM of 60 μm. The electron and hole distributions are shown in red and blue, respectively. Indeed, depletion of electrons is observed for distances less than 350 μm and after that the density steadily rises to its equilibrium value, n_{eq}, shown by a dashed line in the figure. The hole distribution extends farther than the laser spot (purple dots in Figure 6.1) due to diffusion. The product of both distributions, np, is proportional to the luminescence intensity and it is shown in green. A peak in the intensity appears at a distance 357 μm
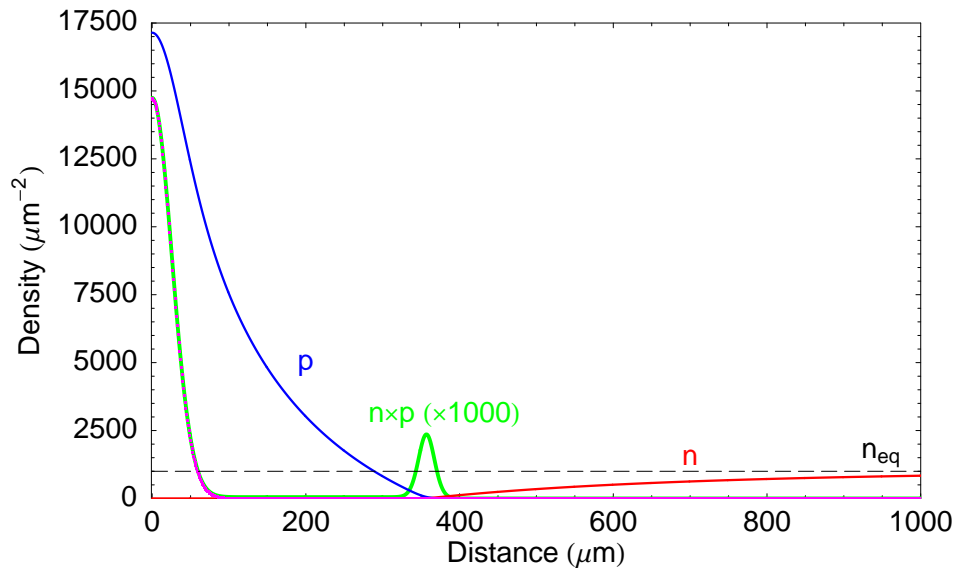
Figure 6.1: Solution of the model for CW excitation. Red–electron density profile; blue–hole density profile; green–their product; purple dots–the excitation profile ($\times 1000$); dashed line–the equilibrium electron density.

where nonzero values of the electron and hole distributions overlap. Since this is actually a one-dimensional radial picture, this peak corresponds to a ring as observed in the 2D luminescence. The calculation is performed with the following parameters: $C_e = 0.2; C_h = 1; 1/\xi = 300\ ns\ \mu m^{-2}; \tau^h_{leak} = \tau^e_{leak} = 20\ \mu s; D_e = 20\ \mu m^2/ns; D_h = D_e m_e/m_h = 5\ \mu m^2/ns$; and $n_{eq} = 10^{11} cm^{-2} = 10^3 \mu m^{-2}$.

For carrier density of 10^{10} cm^{-2} = $100\,\mu m^{-2}$ the value of ξ implies recombination lifetime $\tau_{rec} = 1/\xi n$ of 3 ns which is close to the one observed in the experiment. $C_e = 0.2$ and $C_h = 1$ imply the ratios $\tau^e_{cool}/\tau^e_{drift} = 4$ and $\tau^h_{cool}/\tau^h_{drift} = 0$, $i.e.$, the electrons drift over the barriers four times faster than they cool into the wells and the holes practically don't drift over the barriers at all.

The diffusion coefficient can be calculated from the Einstein relation:

$$\mu k_B T = eD, \tag{6.11}$$

which for hole mobility $\mu = 3 \times 10^5 cm^2/V \cdot s$ gives $D \approx 5\ \mu m^2/ns$.

We can also calculate the decay of the luminescence when the laser is turned off, simulating a pseudo-pulsed laser source. The results from such calculation are shown in Figure 6.2. The laser is turned off at time 0 after we have reached a steady state solution (in practice we solve Eqns. (6.9) and (6.10) with a steady state solution as an initial condition and without a generation term). The central spot decays within 40 ps while the ring persists for some 300 ns. Certainly, the model cannot predict the right time behavior with the proper lifetime but the important feature here is the fact that we indeed see a long lasting ring and quickly dying central spot, similar to the experimental observations from Figure 4.7.

As a more realistic approach to the temporal behavior of the ring we can attempt to model a laser source consisting of real pulses and look at the ring after very long time when it has reached some steady state, if any. In this case, however, since we create hot carriers only during the short laser pulses, we cannot assume steady state conditions when simplifying Equations (6.1) and (6.2) and therefore the full set of four equations (6.1)-(6.4) must be considered. The diffusion of hot carriers can still be neglected since the time scales for carrier thermalization are on the order of 10 ps. The source used in the calculation has 50 ps pulses with 10 MHz repetition rate and average photon flux $A = 3 \times 10^6$ ns^{-1}, which corresponds
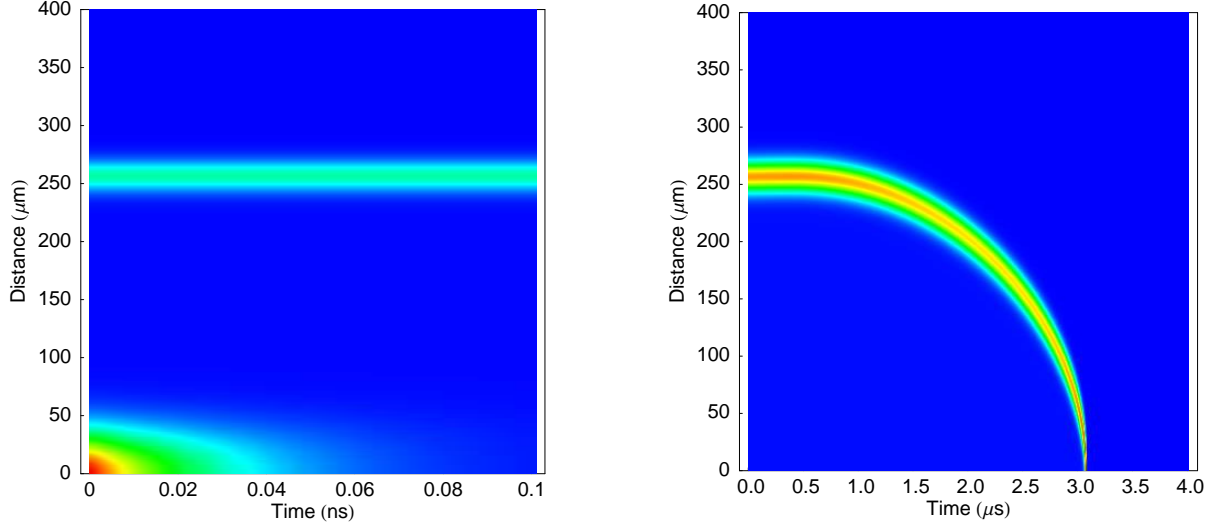
Figure 6.2: Evolution of the ring when the laser is turned off

to 0.9 mW excitation at 632.8 nm. The spatial profile of the source is a Gaussian with FWHM of 60 μm. The other model parameters are $C_e = 0.2, C_h = 1, b = 100\,ns\,\mu m^{-2}, n_{eq} = 10^{11}cm^{-2}, \tau_{leak}^h = \tau_{leak}^e = 2\,\mu s, D_e = 20\,\mu m^2/ns, D_h = 5\,\mu m^2/ns, \tau_{cool}^e = 10\,ps, \tau_{cool}^h = 5\,ps$. Figure 6.3 shows the result of the calculation. It is a steady state with constant ring radius of 340 μm. A comparison with the experimental data for the temporal behavior of the ring (Figures 4.7 and 4.8) shows that the model cannot describe exactly the measured results. It produces the long-time features of the ring but it cannot account for the dip in the time trace observed in Figure 4.8. The numerical simulation also shows a central spot with a very short lifetime, which in this particular case is due mainly to the very short cooling times.

Changing the value of ξ while keeping the other parameters constant doesn't change the size of the ring but only its width. A log-log plot of the FWHM of the ring vs. $1/\xi$ is shown in Figure 6.4. It exhibits a power law dependence. The following parameters were used for the calculation: $A = 3 \times 10^5 ns^{-1}$, $C_e = 0.2$, $C_h = 1$, $n_{eq} = 10^3 \mu m^{-2}$, $\tau_{leak}^e = 6\,\mu s$, $\tau_{leak}^h = 200\,\mu s$, $D_e = 20\,\mu m^2/ns$, $D_h = 5\,\mu m^2/ns$, FWHM of the laser spot 60 μm. Since the radius of the ring doesn't change with ξ, the ring will have the same long-time behavior as in Figure 6.2 independent of the value of ξ.
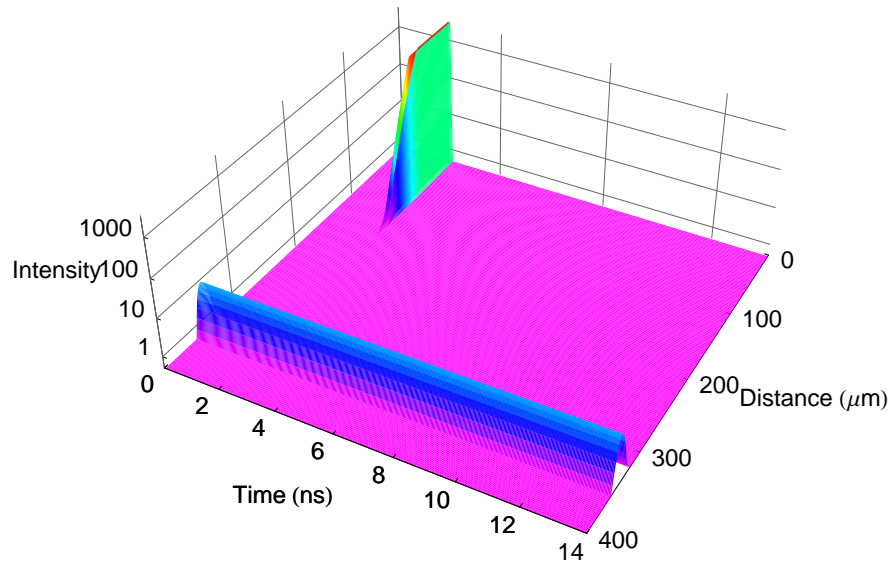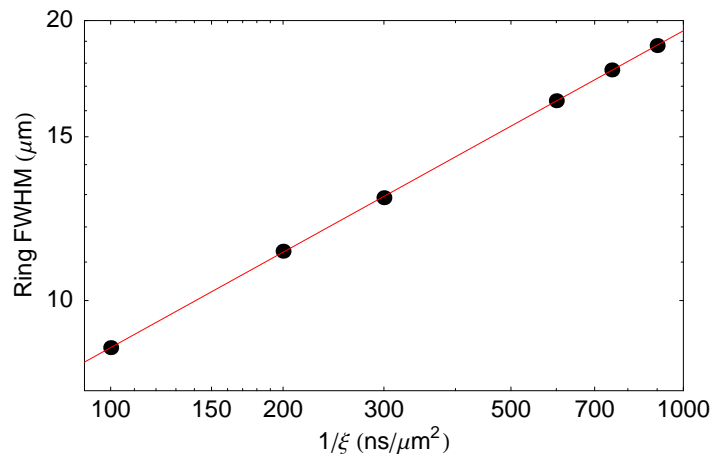
Figure 6.3: Evolution of the ring with pulsed source

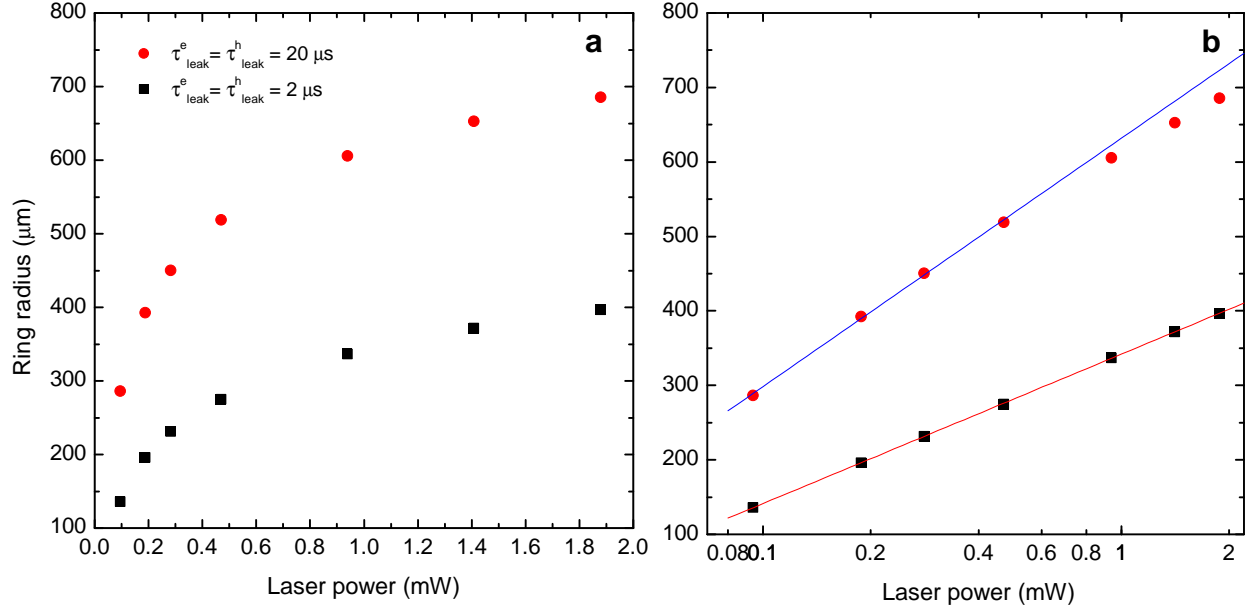Figure 6.4: Calculated FWHM of the ring vs. the parameter ξ.

Figure 6.5: (a) Calculation of the dependence of the ring radius on the laser power for two different values of the leak time. (b) Logarithmic fit to the numerical data.

The model, Eqns. (6.7) and (6.8), also predicts correctly the increase of the ring radius with laser power. The results from such calculation for two different leak times, 2 μs and 20 μs, are shown in Figure 6.5. The power is calculated assuming a laser with wavelength 632.8 nm. The figure shows similar increase of the radius with increasing of the power (or the total photon flux A) as in Figure 4.6 but instead of the pronounced linear dependence of the experimental data it exhibits more logarithmic growth. Figure 6.5(b) shows a logarithmic fit to the numerical data. The parameters used in the calculation are the same as the ones used in Figure 6.1.

One feature we haven't modelled is the dependence on the applied voltage across the quantum well structure. Such dependence ultimately will manifest itself in the change of the equilibrium density of the electrons, since the exciton lifetime depends on the voltage, as well as in the change of the tunneling times.

There are some features of the ring that the model cannot predict correctly. The most prominent one is the failure to describe the proper dependence of the radius on the laser spot

size. The experimental results are shown in Figure 6.6. During the measurement the power of the laser was kept constant and the size of the excitation spot was changed by means of a focusing lens. The measurement was repeated at two different temperatures—2 K and 15 K. In both cases a 4 mW HeNe laser at 632.8 nm was used for excitation. The sample was biased with 0.857 V at 2 K and 0.842 V at 15 K. Both data sets show a monotonic decrease of the ring radius as the laser spot size is increased. The dashed curve in Figure 6.6 is a fit of x^{-2} to the 2 K data. It suggests that the ring radius is proportional to the photon density.

The model prediction, however, differs dramatically from the experimental data. Calculations for two different leak times are shown in Figure 6.7. It is in sharp contrast with the experimental result from Figure 6.6—the model predicts widening of the ring, while the experimental data shows narrowing. The calculation was performed using the parameters from Figure 6.1 and photon flux of 3×10^5 ns^{-1}. A wide range of different parameters was also used in an attempt to get the correct behavior but without success.

Although we have a pretty good understanding of the ring effect, there are still some experimental results that cannot fit into the model. First, sometimes we see non-monotonic dependence of the ring size on the applied voltage and the laser power. Figure 4.5 shows such behavior—increasing the voltage doesn't produce an infinitely large ring. After some point it shrinks back to the central spot. A similar effect at specific conditions was also observed with the power dependence shown in Figure 6.8. At very low excitation power, but above the critical threshold, applying voltage creates a ring which then shrinks when the power is increased while the voltage is kept constant. After reaching a minimum it starts expanding again.

Another effect that is not well understood is the opposite dependence of the ring radius on the excitation spot for the single quantum well sample. Figure 6.9 shows a comparison between the single and double quantum well samples under the same excitation conditions— using a 4 mW 632.8 nm laser. Although the single quantum well data has dependence similar to the numerical model, it is not clear why the behavior of the ring in this structure should differ from the double quantum well sample.

Figures 6.5 and 6.7 also show the increase of the ring when the leak time is increased. It can be explained by the increased number of carriers in the central region which leads to
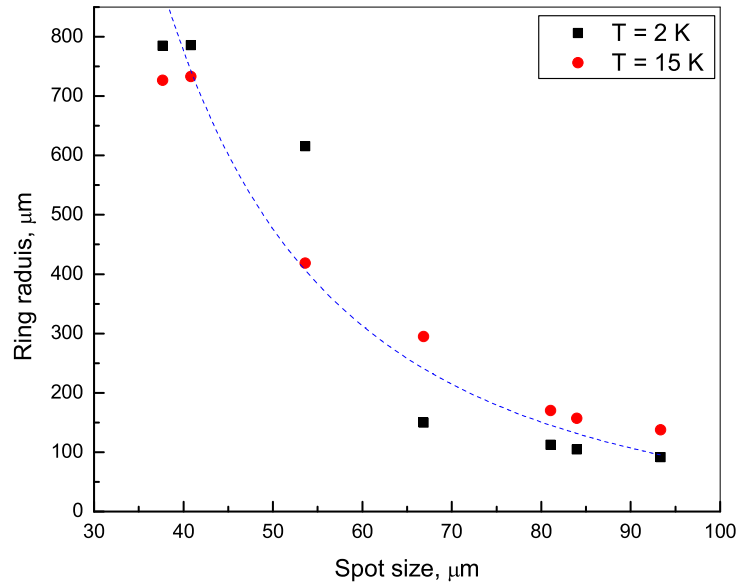
Figure 6.6: Radius of the ring vs. the size of the excitation spot for two different temperatures.

Figure 6.7: Calculation of the dependence of the ring radius on the laser spot size.

Figure 6.8: Non monotonic dependence of the ring radius on the laser power for the double quantum well sample #3. The applied voltage for the 4 K data is 3.43 V and for the 30 K data is 3.79 V.

Figure 6.9: Dependence of the radius of the ring on the laser spot size for the single quantum well sample, compared to the double quantum well sample #3.

larger depletion of electrons and thus to larger ring.

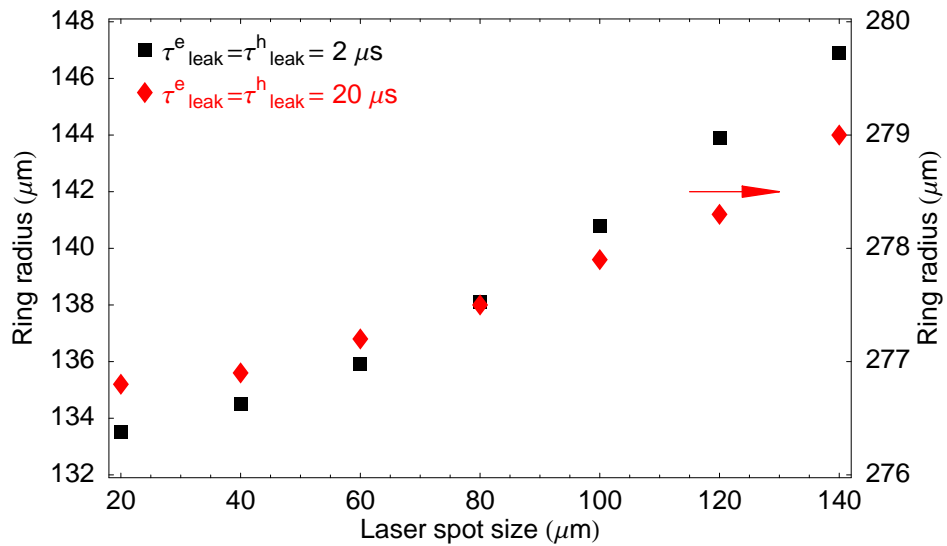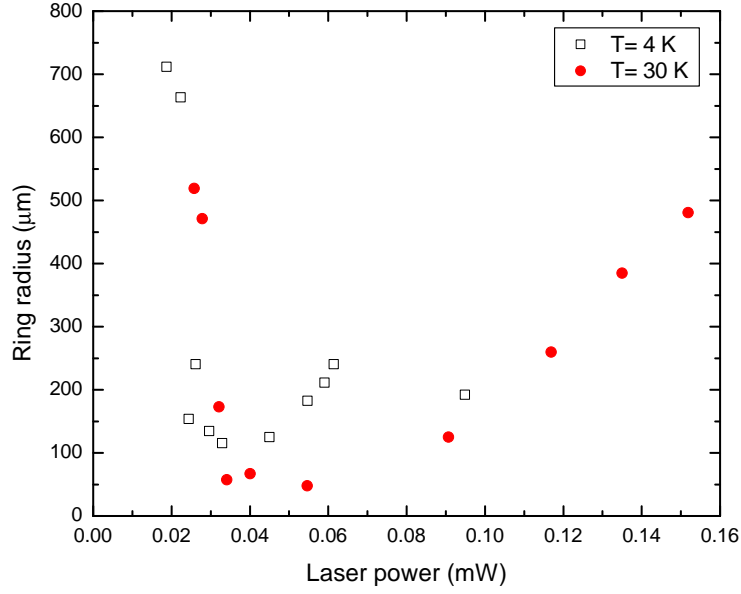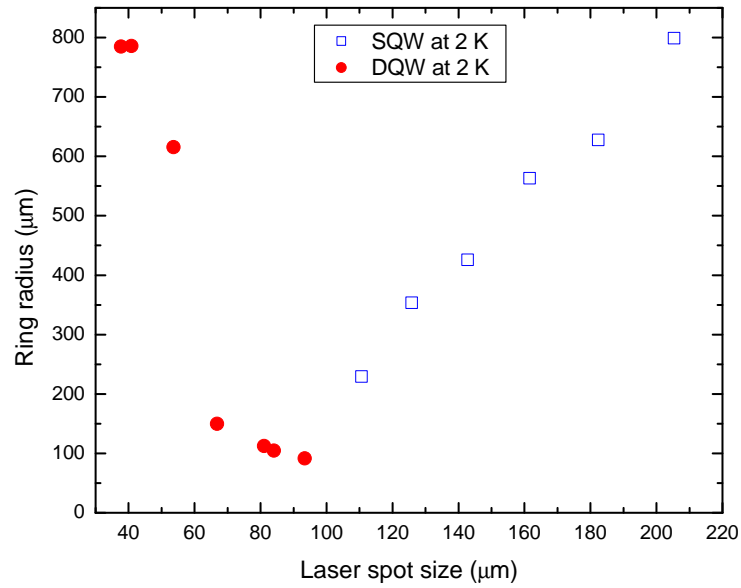Since we assume azimuthal symmetry and solve Eqns. (6.7) and (6.8) in one dimension, we cannot simulate any features that occur along the ring (in ϕ direction). Butov *et al.* [39, 66, 40] have repeatedly reported the fragmentation of the ring into bright spots. As discussed, we haven't succeeded to observe such a phenomenon. In any case, the appearance of such a pattern along the ring may be due to Coulomb interaction between the electron and hole gasses. The model described above doesn't include such interaction but it will certainly play an important role in the ring dynamics. The competition between attractive and repulsive forces at the boundary where the hole puddle meets the electron sea, which marks the location of the ring, may lead to spontaneous breakdown of that smooth boundary and the formation of electron or hole droplets.

In a very recent paper L. Levitov [67] proposed a mechanism of the ring breakdown and pattern formation based on stability analysis of the differential equations describing the ring dynamics. He suggests that local fluctuations in the exciton density can lead to an increase of the electron-hole binding rate and thus deplete locally the carriers which will cause the neighboring carriers to stream toward the fluctuation thus providing positive feedback.

6.2 INCLUSION OF A COULOMB INTERACTION TERM

Recently, we proposed an improved model in which the Coulomb forces between the carriers and their image charge are taken into account [68]. If we consider electrons in the presence of electric field the diffusion equation will have an additional drift term:

$$\frac{\partial n}{\partial t} = D\nabla^2 n + \mu_e \nabla \cdot (\mathbf{E}n) \tag{6.12}$$

To calculate the electric field in the plane of the wells we consider the effect of the heavily doped substrate, which in this case will behave almost like a metal and will produce an image charge which will effectively screen the field. We will consider the metallic surface to be at a distance d from the charge density in the wells, Figure 6.10. We will also assume slowly varying charge density over a region of size d. In our case this assumption is reasonable since
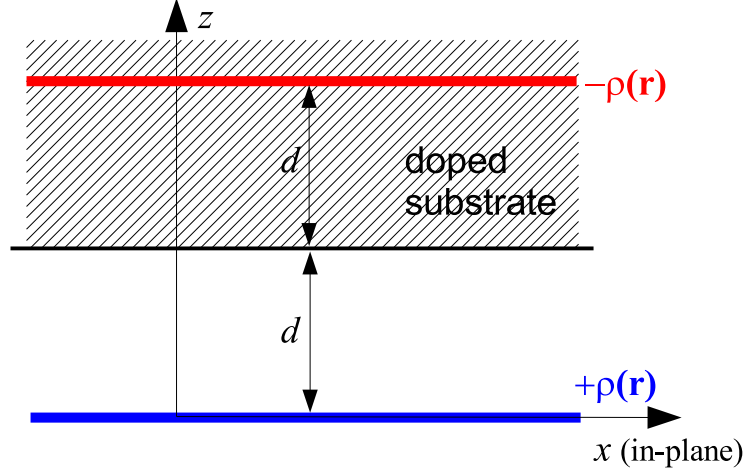
Figure 6.10: The charge density in the quantum well region and its image charge created by the heavily doped substrate.

$d \sim 1000$ Å while the electron and the hole densities change on a scale of microns. Then on the length scale of d we can assume that the gradient of the charge density is constant:

$$\rho(\mathbf{r}) = \rho_0 + \mathbf{r} \cdot \mathbf{G}, \quad \mathbf{G} = \nabla \rho(\mathbf{r}) \tag{6.13}$$

where $\mathbf{r}$ is the coordinate in the x-y plane. The in-plane electric field can be written as

$$\mathbf{E}(\mathbf{r}) = \frac{1}{4\pi\epsilon_0\epsilon} \int \rho(\mathbf{r}') \frac{\mathbf{r} - \mathbf{r}'}{|\mathbf{r} - \mathbf{r}'|^3} d^2 r' \tag{6.14}$$

To simplify the calculation we will consider only the x-component of the field and will assume that the gradient of ρ is in the x direction:

$$\rho_x = \rho_0 + x\, G_x \tag{6.15}$$

Then the x-component of electric field from the in-plane charge density and the image charge at a distance $2d$ is

$$E_x = \frac{1}{4\pi\epsilon_0\epsilon} \int \rho_x \left[\frac{x}{(x^2 + y^2)^{3/2}} - \frac{x}{(x^2 + y^2 + 4d^2)^{3/2}} \right] dx\,dy. \tag{6.16}$$

93

The integral over ρ_0 will vanish since the integrand will be an odd function of x. Thus the expression for the field becomes

$$E_x = \frac{G_x}{4\pi\epsilon_0\epsilon} \int x^2 \left[\frac{1}{(x^2 + y^2)^{3/2}} - \frac{1}{(x^2 + y^2 + 4d^2)^{3/2}} \right] dx dy. \tag{6.17}$$

The integration over y will produce the integral

$$\int_{-\infty}^{\infty} \frac{dy}{(x^2 + y^2)^{3/2}}. \tag{6.18}$$

Making the substitution $y = x \tan\theta$ with $dy = \frac{x d\theta}{\cos^2\theta}$ we get

$$\frac{1}{x^2} \int_{-\pi/2}^{\pi/2} \frac{d\theta}{\cos^2\theta(1 + \tan^2\theta)^{3/2}} = \frac{1}{x^2} \int_{-\pi/2}^{\pi/2} \cos\theta \, d\theta = \frac{2}{x^2} \tag{6.19}$$

This gives for the field

$$\begin{aligned}
E_x &= \frac{G_x}{4\pi\epsilon_0\epsilon} \int 2x^2 \left[\frac{1}{x^2} - \frac{1}{x^2 + 4d^2} \right] dx \\
&= \frac{2G_x}{4\pi\epsilon_0\epsilon} \int \frac{4d^2}{x^2 + 4d^2} dx \\
&= \frac{2G_x d^2}{\pi\epsilon_0\epsilon} \frac{1}{2d} \arctan\left(\frac{x}{2d}\right) \Big|_{-\infty}^{+\infty} \\
&= \frac{G_x d}{\epsilon_0\epsilon}
\end{aligned} \tag{6.20}$$

The calculation in the y direction can be performed in a similar fashion. We can now write the general expression for the field:

$$\mathbf{E} = \frac{d}{\epsilon_0\epsilon} \nabla\rho, \tag{6.21}$$

or expressed in electron and hole population densities

$$\mathbf{E} = \frac{e\,d}{\epsilon_0\epsilon} \nabla(p - n). \tag{6.22}$$

Then the diffusion equations (6.7) and (6.8) will become

$$\frac{\partial n}{\partial t} = D_e \nabla^2 n + C_e G(\mathbf{r}) - \frac{n - n_{eq}}{\tau_{leak}^e} - \xi\, n\, p - \frac{e\mu_e d}{\epsilon_0\epsilon} \nabla \cdot n \nabla(p - n) \tag{6.23}$$

$$\frac{\partial p}{\partial t} = D_h \nabla^2 p + C_h G(\mathbf{r}) - \frac{p}{\tau_{leak}^h} - \xi\, n\, p + \frac{e\mu_h d}{\epsilon_0\epsilon} \nabla \cdot p \nabla(p - n) \tag{6.24}$$

These two equations when solved in two dimensions may produce an instability that can result in breaking of the ring into localized spots of bright luminescence. The first step, however, is to establish if this model can reproduce the ring effect at all.

An estimate for the value of the coefficient of the Coulomb term $M_{e(h)} = \dfrac{e\mu_{e(h)}d}{\epsilon_0\,\epsilon}$ gives 8.3 $\mu m^4/ns$ (for $\mu = 3 \times 10^5 cm^2/V \cdot s$; $d = 2000$ Å; $\epsilon = 13$). If we consider a degenerate Fermi gas in 2D the diffusion coefficient will be $D = v_F^2\tau$, where τ is the scattering time. In 2D, however, v_F^2 is proportional to the density, since the Fermi energy is

$$E_F = \frac{\pi\hbar^2 n}{m} = \frac{mv_F^2}{2}. \tag{6.25}$$

Then $D = \dfrac{2\pi\hbar^2 n\,\tau}{m^2}$ will depend on the density and the diffusion term $D\nabla^2 n$ has to be changed to $\nabla \cdot D\nabla n = C\nabla \cdot n\nabla n$, where $C = \dfrac{2\pi\hbar^2\tau}{m^2}$, in which case it will have the same form as the Coulomb term. An estimate of the constant C gives us $C = (8.42\tau)\mu m^4/ns^2$. For typical values of τ on the order of 10 ps, $C \sim 0.08\ \mu m^4/ns$ which means that the Coulomb pressure term is the dominating one in (6.23) and (6.24).

Numerical calculations show that indeed the Coulomb pressure term can generate a ring in a way similar to the simple diffusion case. Some results are shown in Figures 6.11 and 6.12. Figure 6.11 shows the electron and hole distributions (red and blue, respectively), their product which is proportional to the luminescence intensity, and the profile of the excitation. The parameters used are as follows: $C_e = 0.2$; $C_h = 1$; $1/\xi = 300\ ns/\mu m^2$; $\tau_{leak}^e = \tau_{leak}^h = 2\ \mu s$, $D_e = D_h = 0$; $M_e = 1.5\ \mu m^4/ns$; $M_h = 0.3\ \mu m^4/ns$, where M_e and M_h are the two Coulomb terms and we have accounted for the reduced mobility of the carriers in the wells [51]. Figure 6.12 shows a comparison between two excitations with two different excitation powers and two different excitation spot sizes. The values of the parameters are the same as in the previous figure. This calculation shows an excitation power dependence in the right direction—the ring increases with increasing power—but on the other hand doesn't produce any dependence on the laser spot size.

Apparently this model is successful in reproducing the ring effect but more detailed study is required in order to balance all parameters and describe the experimental data.
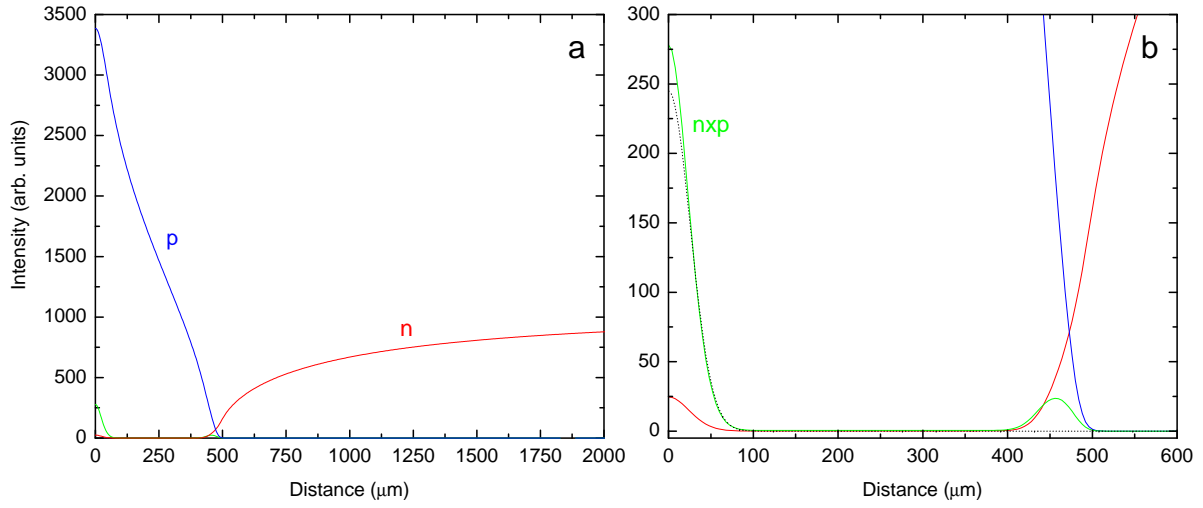
Figure 6.11: Solution of (6.23) and (6.24): (a) The electron and hole densities. (b) Blowup of (a) showing the luminescence intensity. The dotted line in (b) is the profile of the excitation
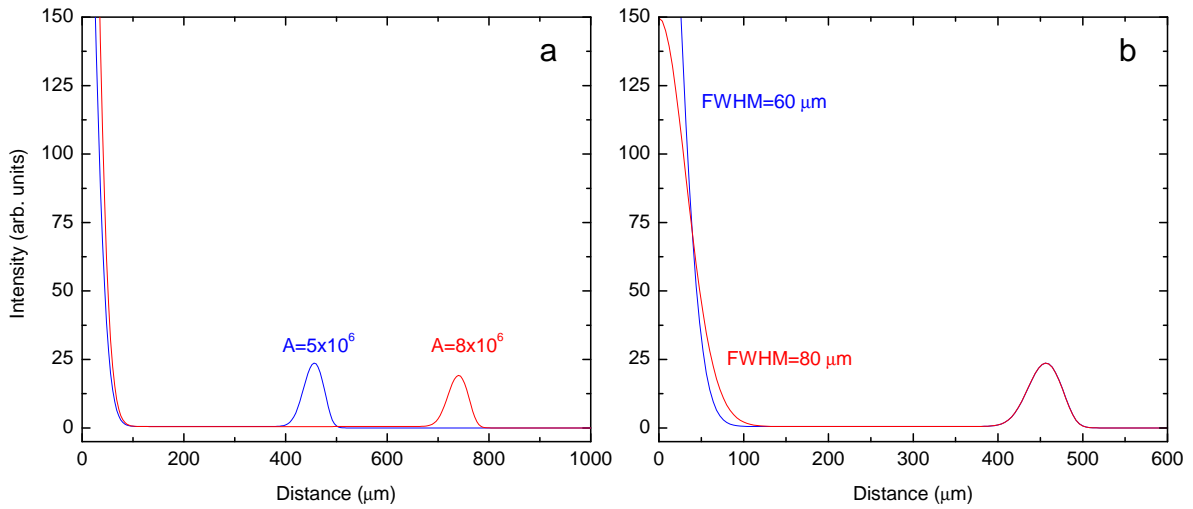

Figure 6.12: Solutions of (6.23) and (6.24) for two different excitation powers, (a), and two different laser spot sizes, (b). In (a) the laser spot is 60 μm and in (b) the photon flux is $A = 5 \times 10^6 ns^{-1}$. All other parameters are the same in both figures.

7.0   CONCLUSIONS AND FUTURE DIRECTIONS

The main motivation for the experiments was to study exciton dynamics in coupled quantum well structures as possible systems for BEC. The advantages of such systems were discussed earlier. We certainly have not achieved BEC but the work provided us with some very interesting and unique effects. The ring effect was an unexpected surprise and although it may have little to do with superfluidity of excitons, nevertheless it is an intriguing phenomenon in a two-dimensional electron system. This shows that the quantum wells indeed have potential in studies of dynamics of 2D electron gases.

Our sample, $In_{0.1}Ga_{0.9}As$ quantum wells with GaAs barriers, is not perfect for studying dynamics of excitons. Although it was initially designed so that the band gap of $In_{0.1}Ga_{0.9}As$ would be below the band gap of GaAs which allowed for resonant excitation without creating carriers in the sample substrate, still the current through the sample when voltage was applied was quite high. This ultimately reduces the mobility of the excitons. Another big factor for the low mobility is the presence of alloy disorder in the quantum well region. Indium provides the necessary lower band gap, but it is of very low concentration and in fact can be considered as an impurity. In the pursuit of low current the thick $Al_{0.32}Ga_{0.68}As$ barriers outside the quantum well region were grown. They, however, turned out to be not that effective in blocking the current as originally thought. Figure 7.1(a) shows one of the problems. Because of the tilt of the bands due to the applied voltage the thick $Al_{0.32}Ga_{0.68}As$ barrier now presents only a portion of its thickness to the electrons which makes it easier for them to tunnel. A solution to this problem would be instead of one very thick barrier to build a superlattice of $Al_{0.32}Ga_{0.68}As$ and GaAs as shown in Figure 7.1(b). In such a way the GaAs wells will be natural traps for the tunneling electrons and the current will be quenched effectively. Another problem we have encountered was the short lifetime and
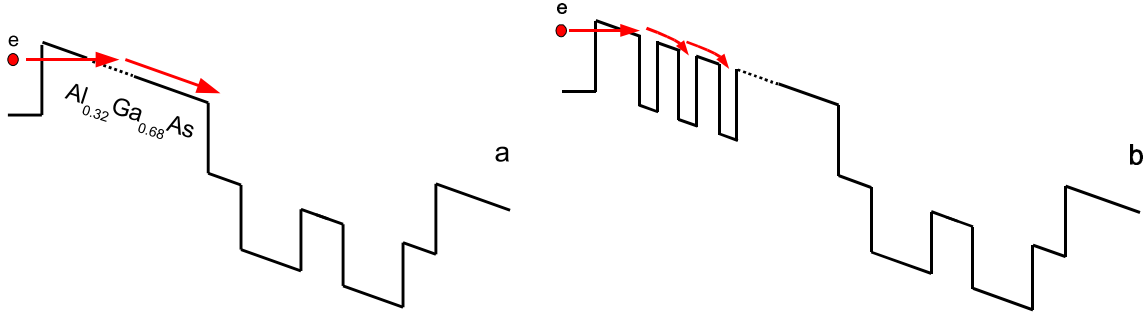
97

Figure 7.1: (a) Tunneling through the $Al_{0.32}Ga_{0.68}As$ barrier when voltage is applied. (b) Superlattices in the barriers provide effective traps for the hot carriers.

very low mobility of the excitons. The reason for this could be two fold. On one hand increasing the quantum well width increases the lifetime and the mobility, but on the other hand this will reduce the confinement energy and will bring the exciton luminescence from the quantum well closer to the substrate luminescence.

So there seems to be several things that can be done to improve the performance of the samples. First, use pure GaAs instead of the $In_{0.1}Ga_{0.9}As$ alloy. This will reduce the impurities in the quantum wells and arguably will increase the mobility of the excitons. The problem with this approach is that, since the whole structure is grown on a GaAs substrate, the exciton luminescence from will be very close to the substrate luminescence which will make them hard to separate. The increased background from the substrate will make threshold measurements, like those we performed with the ring, virtually impossible.

Second, make the wells wider. This will increase the exciton mobility [51]. Third, instead of having one thick $Al_{0.32}Ga_{0.68}As$ barrier build a superlattice of $GaAs/Al_{0.32}Ga_{0.68}As$ which will act as series of traps for the hot carriers. The current can be reduced further if the doping is p-i-n instead of n-i-n and apply reverse bias. The n-i-n doping of the $In_{0.1}Ga_{0.9}As$ sample provided the required high electric field to create indirect excitons. The problem with it is that the hot carriers are free to flow in both directions through the quantum well region. A reversely biased p-i-n structure has the benefit of the high electric field across the quantum wells and at the same time separates the charges so that the current through the
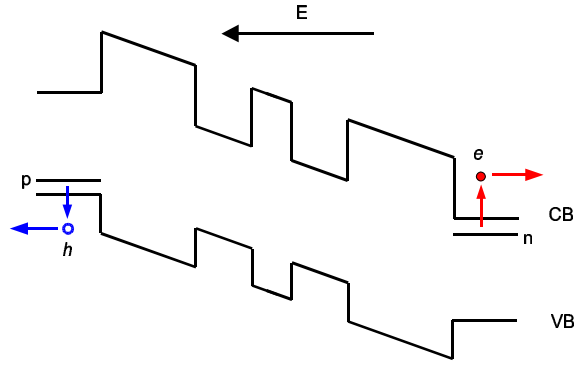
Figure 7.2: In reversely biased p-i-n structure the electrons and the holes move in opposite directions, thus reducing the current through the sample.

sample is minimal. Figure 7.2 shows a diagram of such structure. Photogenerated electrons and holes from the donor and acceptor levels in the doped regions will tend to move in opposite directions thus reducing the current through the sample.

Taking all these considerations into account, new samples were designed and grown by the same team at Bell Labs. They consist of two 100 Å GaAs quantum wells separated by a 40 Å $Al_{0.32}Ga_{0.68}As$ barrier. On each side of the QW region there are 300 Å thick $Al_{0.32}Ga_{0.68}As$ barriers and series of 10 periods of $GaAs/Al_{0.32}Ga_{0.68}As$ with 40-60 Å thickness. The results from this sample are indeed very encouraging. An image of the indirect luminescence is shown in Figure 7.3. The sample is excited by an almost resonant laser with 60 μm spot size. The image is in focus—this is the actual size of the exciton cloud diffusing in the plane of the quantum wells reaching distances 200 μm away from the excitation spot. The blue shift of the center is due to band renormalization at high exciton density.

Time traces at various distances away from the central spot are shown in Figure 7.4. In order to travel such long distances the indirect excitons must have very long life time. It is indeed on the order of 2 μs. The time traces are consistent with diffusion.

These preliminary results show the huge promise this type of samples has. The next step is to trap the excitons in a potential trap and manipulate the density in order to investigate the possibility for superfluidity.
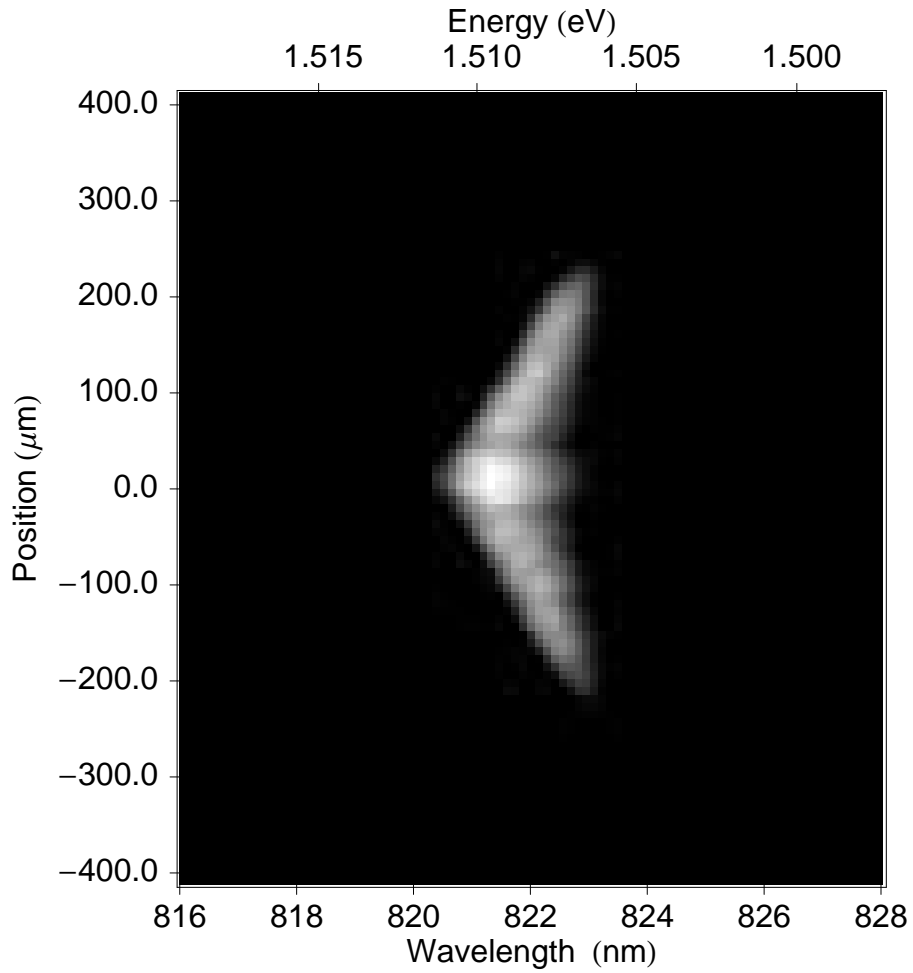
Figure 7.3: CCD image of the indirect exciton luminescence in the 100-40-100 GaAs QW sample. Modelocked laser with λ=797 nm and P=1.3 mW was used to excite the sample.
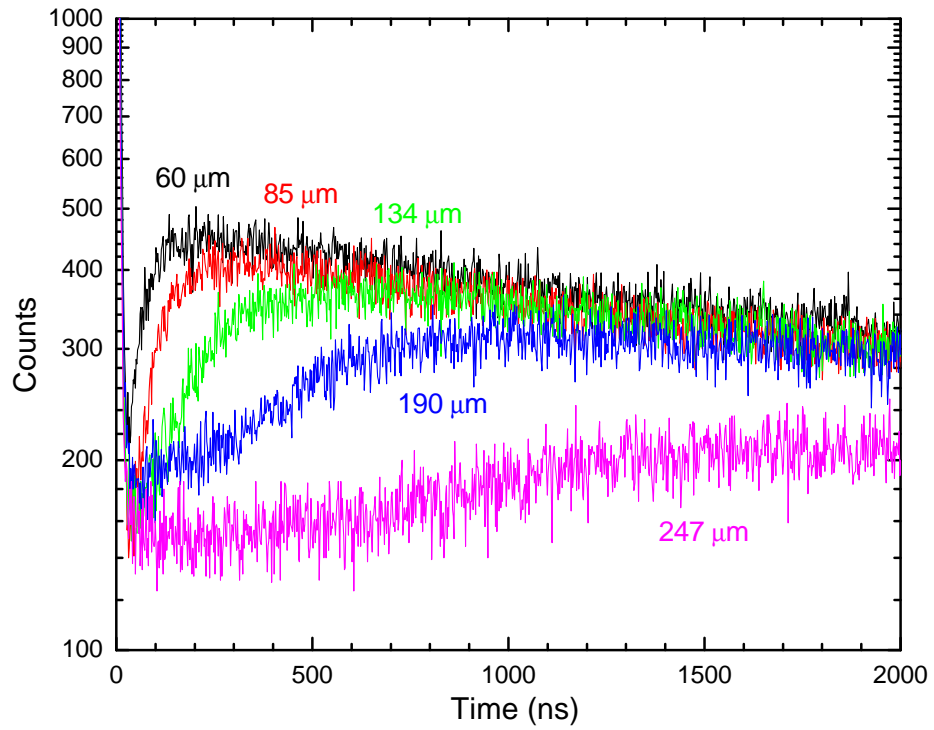
Figure 7.4: Time traces of the indirect exciton luminescence at increasing distances from the excitation spot. The sample was excited by a laser with repetition rate of 250 kHz and $\lambda=$ 786 nm.

BIBLIOGRAPHY

[1] M. H. Anderson, J. R. Enssher, M. R. Matthews, C. E. Wieman, and E. A. Cornell, *Science* **269**, 198 (1995)

[2] M. R. Andrews, M. -O. Mewes, N. J. van Druten, D. S. Durfee, D. M. Kurn, and W. Ketterle, *Science* **273**, 84 (1996)

[3] J. M. Blatt, K. W. Böer, and W. Brandt, Phys. Rev. **126**, 1691 (1962)

[4] S. A. Moskalenko, Fiz. Tverd. Tela Leningrad **4**, 276 (1962) [Sov. Phys. Solid State **4**, 199 (1964)]

[5] L. V. Keldysh and A. N. Kozlov, Zh. Eksp. Teor. Fiz. **54**, 978 (1968) [Sov. Phys. JETP **27**, 521 (1968)]

[6] E. Hanamura and H. Haug, Phys. Rep. C **33**, 209 (1977)

[7] B. Laikhtman, Europhys. Lett. **43** (1), 53 (1998)

[8] A. Olaya-Castro, L. Quiroga, and C. Tejedor, Solid State Comm. **127**, 141 (2003)

[9] T. C. Damen, J. Shah, D. Y. Oberli, D. S. Chemla, J. E. Cunningham, and J. M. Kuo, Phys. Rev. B **42** (12), 7434 (1990)

[10] W. F. Brinkman and T. M. Rice, Phys. Rev. B **7**, 1508 (1973)

[11] L. V. Keldysh, Contemp. Phys. **27**, 395 (1986)

[12] L. V. Keldysh in *Bose-Einstein Condensation*, ed. A. Griffin, D. W. Snoke, and S. Stringari (Cambridge University Press, 1995)

[13] R. C. Miller, D. A. Kleinman, W. T. Tsang, and A. C. Gossard, Phys. Rev. B **24**, 1134 (1981)

[14] G. Bastard, E. E. Mendez, L. L. Chang, and L. Esaki, Phys. Rev. B **26**, 1974 (1982)

[15] M. Grundmann and D. Bimberg, Phys. Rev. B **38**, 13486 (1988)

[16] Z. S. Piao, M. Nakayama, and H. Nishimura, Phys. Rev. B **54**, 10312 (1996); Z. S. Piao, M. Nakayama, and H. Nishimura, Phys. Rev. B **53**, 1485 (1996)

[17] R. L. Greene, Phys. Rev. B **29**, 1807 (1984)

[18] D. S. Chemla and D. A. B. Miller, J. Opt. Soc. Am. B **2**, 1155 (1985)

[19] R. Dingle, W. Wiegmann, and C. H. Henry, Phys. Rev. Lett. **33**, 827 (1974)

[20] L. Esaki and R. Tsu, *Superlattice and negative conductivity in semiconductors*, IBM Research Note RC-2418 (1969)

[21] L. Esaki and R. Tsu, IBM J. Res. Dev. **14**, 61 (1970)

[22] J. Feldmann, G. Peter, E. O. Göbel, P. Dawson, K. Moore, C. Foxon, and R. J. Elliott, Phys. Rev. Lett **59** (20), 2337 (1987)

[23] P. C. Hohenberg, Phys. Rev. **158** (2), 383 (1967)

[24] V. Bagnato and D. Kleppner, Phys. Rev. A **44** (11), 7439 (1991)

[25] P. Nozieres in *Bose-Einstein Condensation*, ed. A. Griffin, D. W. Snoke, and S. Stringari (Cambridge University Press, 1995)

[26] V. Negoita, D. W. Snoke, and K. Eberl, Phys. Rev. B **60**, 2661 (1999)

[27] V. Negoita, D. W. Snoke, and K. Eberl, Appl. Phys. Lett. **75** (14), 2059 (1999)

[28] J. M. Kosterlitz and D. J. Thouless, J. Phys. C: Solid State Phys., Vol. 6, 1181 (1973)

[29] D. R. Nelson and J. M. Kosterlitz, Phys. Rev. Lett. **39** (19), 1201 (1977)

[30] Daniel S. Fisher and P. C. Hohenberg, Phys. Rev. B **37**, 4936 (1988)

[31] Yu. E. Lozovik and V. I. Yudson, Pis'ma ZhETF **22**, 556 (1975) [JETP Lett. **22**, 274 (1975)]; Yu. E. Lozovik and V. I. Yudson, Sol. State Comm. **19**, 391 (1976)

[32] T. Fukuzawa, E. E. Mendez, and J. M. Hong, Phys. Rev. Lett. **64** 25, 3066 (1990)

[33] A. V. Larionov, V. B. Timofeev, J. Hvam, and K. Soerensen, JETP **90** 6, 1093 (2000)

[34] A. V. Larionov, V. B. Timofeev, P. A. Ni, S. V. Dubonos, I. Hvam, and K. Soerensen, JETP Lett. **75** 11, 570 (2002)

[35] A. A. Dremin, V. B. Timofeev, A. V. Larionov, J. Hvam, and K. Soerensen, JETP Lett. **76** 7, 450 (2002)

[36] L. V. Butov, A. Zrenner, G. Abstreiter, G. Böhm, and G. Weimann, Phys. Rev. Lett. **73** 2, 304 (1994)

[37] L. V. Butov, A. L. Ivanov, A. Immamoglu, P. B. Littlewood, A. A. Shashkin, V. T. Dolgopolov, K. L. Campman, and A. C. Gossard, Phys. Rev. Lett. **86** 24, 5608 (2001)

[38] L. V. Butov, Sol. State Comm. **127**, 89 (2003)

[39] L. V. Butov, A. C. Gossard, and D. S. Chelma, Nature **418**, 751 (2002)

[40] L. V. Butov, L. S. Levitov, A. V. Mintsev, B. D. Simons, A. C. Gossard, and D. S. Chemla, Phys. Rev. Lett. **92** 11, 117404 (2004)

[41] O. L. Berman, Y. E. Lozovik, D. W. Snoke, and R. D. Coalson, cond-mat/0406587 (2004); O. L. Berman, Y. E. Lozovik, D. W. Snoke, and R. D. Coalson, cond-mat/0408053 (2004)

[42] Viorel Negoita, PhD Thesis *Potential Traps for Excitons in Two and Three Dimensional Systems*, Department of Physics and Astronomy, University of Pittsburgh (2001)

[43] *Semiconductors: Group IV Elements and III-V Compounds*, ed. O.Madelung, (Springer-Verlag, 1991)

[44] Sadao Adachi, *GaAs and Related Materials: Bulk Semiconducting and Superlattice Properties*, (World Scientific, 1994); Sadao Adachi, J. Appl. Phys. **58** (3), R1 (1985); Sadao Adachi, J. Appl. Phys. **53** (12), 8775 (1982)

[45] C. Bosio, J. Staehli, M. Guzzi, G. Burri, and R. A. Logan, Phys. Rev. B **38**, 3263 (1988)

[46] D. J. Arent, Phys. Rev. B **41**, 9843 (1990)

[47] R. T. Deck and Xiangshan Li, Am. J. Phys. **63** (10), 920 (1995)

[48] M. H. Szymanska and P. B. Littlewood, Phys. Rev. B **67**, 193305 (2003)

[49] M. H. Szymanska, P. B. Littlewood, and R. J. Needs, Phys. Rev. B **63**, 205317 (2001)

[50] X. F. Wang, I. C. da Cunha Lima, and X. L. Lei, Phys. Rev. B **58** (19), 12609 (1998)

[51] H. Sakaki, T. Noda, K. Hirakawa, M. Tanaka, and T. Matsusue, Appl. Phys. Lett. **51** (23), 1934 (1987)

[52] Z. Y. Xu, S. R. Jin, C. P. Luo, and J. Z. Xu, Sol. State Comm. **87** (9), 797 (1993)

[53] K. K. Choi, B. F. Levine, N. Jarosik, J. Walker, and R. Malik, Phys. Rev. B **38**, 12362 (1988)

[54] M. Lee, N. Wingreen, S. Solin, and P. Wolff, Sol. State Comm. **89**, 687 (1994)

[55] S. Denev, V. Negoita, D. W. Snoke, B. Laikhtman, K. Eberl, and L. Pfeiffer, Phys. Rev. B **66**, 205304 (2002)

[56] V. Negoita, D. W. Snoke, K. Eeberl, Sol. State Comm. **113**, 437 (2000)

[57] V. V. Krivolapchuk, D. A. Mazurenko, N. K. Poletaev, and A. L. Zhmodikov, Phys. Solid State **40** (5), 737 (1998)

[58] I. Aksenov, J. Kusano, Y. Aoyagi, T. Sugano, T. Yasuda, and Y. Segawa, Phys. Rev. B **51** (7), 4278 (1995)

[59] D. L. Miller and B. Laikhtman, Phys. Rev. B **54**, 10669 (1996)

[60] D. Snoke, S. Denev, Y. Liu, L. Pfeiffer, and K. West, Nature **418**, 754 (2002)

[61] J. S. Blakemore, J. Appl. Phys. **53** (10), R123 (1982)

[62] A. Siarkos, E. Runge, and R. Zimmermann, Phys. Rev. B **61** (16), 10854 (2000)

[63] S. A. Moskalenko and D. W. Snoke, *Bose-Einstein Condenstation of Excitons and Biexcitons*, (Cambridge University Press, 2000)

[64] D. Snoke, Y. Liu, S. Denev, L. Pfeiffer, and K. West, Sol. State Comm. **127**, 127 (2003)

[65] R. Rapaport, Gang Chen, D. Snoke, S. H. Simon, L. Pfeiffer, K. West, Y. Liu, and S. Denev, Phys. Rev. Lett. **92** 11, 117405 (2004)

[66] L.V. Butov, L.S. Levitov, A.V. Mintsev, B.D. Simons, A.C. Gossard, and D.S. Chemla, cond-mat/0308117 (2003)

[67] L. S. Levitov, B. D. Simons, and L. V. Butov, cond-mat/0403377 (2004)

[68] D. Snoke, S. Denev, Y. Liu, S. Simon, R. Rapaport, G. Chen, L. Pfeiffer, and K. West, in press